UNIVERSITÀ DEGLI STUDI DI TRIESTE

XXIX CICLO DEL DOTTORATO DI RICERCA IN FISICA

TIME AND ANGLE-RESOLVED PHOTOELECTRON SPECTROSCOPY STUDIES OF NOVEL TOPOLOGICALLY ORDERED MATERIALS

Settore scientifico-disciplinare: **FIS/03 FISICA DELLA MATERIA**

DOTTORANDO / A
ANDREA STERZI

COORDINATORI
PROF. PAOLO CAMERINI
PROF. LIVIO LANCERI

SUPERVISORE DI TESI
PROF. FULVIO PARMIGIANI

CO-SUPERVISORI DI TESI
DR. ALBERTO CREPALDI
DR. FEDERICO CILENTO

ANNO ACCADEMICO 2015/2016

Contents

Chapter 1

Introduction

1.1 Prelude

The different phases of matter are conventionally described according to their pattern of symmetry breaking. In the last decades however we assisted to the prediction and discovery of materials eluding this classification. In this regard, the studies of J. Michael Kosterlitz and David J. Thouless have paved the way for the discovery and realization of what has been called a "new topological phases of matter".

During the 70s a new phase transition have been discovered; the Kosterlitz-Thouless (K-T) transition, in which topological defects play a fundamental role. Unexpectedly, in contrast to conventional phase transitions, the "K-T" transition shows no symmetry breaking [1]. In 1980 Klitzing realized the first material whose ground state is defined by its topology and not by symmetry breaking. This class has been named as "two-dimensional (2D) Quantum Hall (QH) materials". The QH state can be regarded as the first realization of the predicted novel topological phase [2]. Schematically QH insulators are 2D insulators presenting anomalous transport properties at the edges, in a low temperature and strong external magnetic field regime. The Hall conductivity is quantized and, while they are insulating in the bulk, electrons can travel freely at the surface.

Soon after, David J. Thouless and collaborators explained the quatized Hall conductivity in QH states by developing new models. In 2016, these studies have culminated with the assignment of the Nobel prize in physics to David J. Thouless, F. Duncan M. Haldane and J. Michael

Kosterlitz for the *"Topological phase transition and topological phase of matter"* [3]. In the years following the discovery of QH states, a large scientific interest arose for searching new topological materials. In 2006 Bernevig and Hughes proposed that it could have been possible to obtain a quantum spin Hall insulator (QSHI) system by growing a HgTe/CdTe quantum well [4]. QSHIs are insulators in the bulk and metallic at the surface, mimicking the behaviour of the QH states, but in absence of external magnetic fields. QSHIs show spin-polarized and topologically protected surface states at the edges, under the influence of strong atomic spin orbit coupling (SOC). These systems have also been defined as 2D Topological insulators (TIs), a concept which has been successively extended to the three-dimensional case, for the 3D topological insulators.

Since the synthesis of the $Bi_{1-x}Sb_x$ alloy in 2007 as the first TI, a huge numbers of experimental and theoretical works have been published [5]. One of the reasons why TIs have captured the attention of the relevant scientific community, is because they seemed the natural ideal candidates for future spintronics applications. Among the numerous results in this field, we mention the integration of magnetic materials with topological insulators, which has led to the genesis of topological spintronics [6]. The investigation of the spin dynamics in ferromagnet - TI- heterostructures, has revealed the great potential of the $\mathrm{Bi_2Se_3}$ TI for spintronics devices [6]. As a matter of fact, efficient spin-transfer torque devices has been already realized, by using a thin film of $\mathrm{Bi_2Se_3}$ in combination with a ferromagnetic permalloy [7].

Another important study research area for these materials aims at exploiting phenomena associated to the coupling of light to Tis, these includes: the colossal Kerr rotation [8], photo-induced spin currents [9] and long-lived surface state population [10]. A number of studies have also investigated the electrons and the phonons dynamics induced by an ultrafast optical excitation by using time- and angle- resolved photoemission spectroscopy [11, 12, 13, 14, 10]. Angle-resolved photoelectron spectroscopy (ARPES) is the ideal tool to explore such processes, since it allows to probe directly the band structure of materials. Time-resolved ARPES (TR-ARPES) can provide a stroboscopic picture on the femtosecond time-scale of the evolving excited states via a pump-and- probe approach.

TR-ARPES studies performed on different doped TIs, revealed differences in their transient electron dynamics [11, 15, 16]. However, no study so far has systematically addressed the role of doping in these materials, in particular, concerning the contributions of different relaxation

mechanisms such as the diffusion and the electron-phonon scattering.

During my PhD thesis I performed a systematic study on six different doped TIs by means of TR-ARPES. The motivation of my work aims at understanding the role of different relaxation channels that, in cooperation with the electron-phonon scattering, determine the thermalization of the system. The formation of the topological phase is possible under the influence of a strong SOC which induces a hybridization between valence and conduction bands. This process, leading to the formation of the topological surface state, is followed by a band parity inversion.

This important mechanism has been verified by analyzing linear dichroic effects in the photoemission spectra of the prototypical $GeBi_2Te_4$ TI. To study in detail the dichroic character of the bulk valence bands I have used the technique of linear-dichroic ARPES (LD-ARPES). The SmB_6 compound has been also investigated by means of TR-ARPES, with the intent of evaluating its electron-phonon coupling constant. Contrary to "conventional" TIs, this material is a strongly correlated Kondo Insulator (KI), which in the last years has been proposed to be Topological Kondo Insulator (TKI) [17]. Its classification however, despite several studies focused on understanding topological nature, is still under debate.

In the last year of my PhD, I had the opportunity to investigate a novel topological phase of matter known as Weyl semimetals (WSMs). The band structure of the WSMs presents unique features, such as point-like Fermi surfaces and open Fermi arcs [18, 19]. In particular, I have focused my attention on $MoTe_2$, that is a transition metal dichalcogenide showing the WSM behaviour. This material, differently from other WSMs, presents a temperature-induce structural phase transition. [20]-[21]. The high temperature phase is centrosymmetric ($1T''$), while the low temperature phase is non-centrosymmetric ($1T'$). Only the latter case should support the Weyl semimetal phase $1T'$. However such a prediction still waiting for a clear experimental confirmation.

To shed light on this controversial question, an ARPES and spin-resolved ARPES (SARPES) study of both the the two $MoTe_2$ phases has been performed. Spin-polarized 2D states forming Fermi arcs have been observed. However, the type-II WSM nature of $MoTe_2$ has not established, since a Fermi arc was found to persist in the high temperature centrosymmetric $1T''$ phase.

1.2 Outline of the Thesis

In the following is the outline of the thesis.

- **Chapter 2**: This chapter briefly introduces the conventional and the time-resolved ARPES technique. The main models used to analyze the time-resolved spectra are reviewed: the concept of a "hot" - Fermi Dirac distribution is introduced and a modified version of the two-temperature (2T) model is derived. In the last part of the chapter the experimental TR-ARPES setup is described. In particular, the development of a novel pump-probe optical setup for fourth harmonics generation is detailed.

- **Chapter 3**: The third chapter deals with a short introduction to the quantum Hall (QH) effect and quantum spin Hall (QSH) insulators, since these systems can be regarded as the precursors of TIs. I provide the theoretical picture and the basic concepts that define the nontrivial topological phase, the Z_2 topological invariant, the fundamental quantity at the base of the topological materials classification.

  The second part reviews the "state-of-the-art" of TR-ARPES studies on TIs, by focusing on the most important investigations, ranging from the first works on $\mathrm{Bi_{1-x}Sb_x}$ to more recent time-resolved experiments on the archetypal $\mathrm{Bi_2Te_3}$ and $\mathrm{Bi_2Se_3}$ topological insulators.

- **Chapter 4**: Chapter 4 presents the results of the investigation of different doped TIs showing that the relaxation dynamics of the excited state population is strongly influenced by the doping level of the material under scrutiny. By extracting the evolution of the electronic temperature for the different compounds I discuss and elucidate the role played by charge diffusion processes.

- **Chapter 5**: This chapter introduces $\mathrm{SmB_6}$ within the frame of Kondo Insulators (KI) and Topological Kondo Insulators (TKI). This material has attracted a great interest because of its anomalous transport properties and since it has been proposed as the first realization of a strongly-correlated TI. The basic literature about $\mathrm{SmB_6}$, including the discussion on its topological nature and previous ARPES studies, is reviewed.

- **Chapter 6**: The sixth chapter focuses on the study of the $\mathrm{SmB_6}$ compound. I have investigated its out-of-equilibrium electron dynamics by means of time- and angle-resolved

photoelectron spectroscopy. The transient electronic population above the Fermi level can be described by a time-dependent Fermi-Dirac distribution. By solving a two-temperature model (2T) that well reproduces the relaxation dynamics of the effective electronic temperature, I estimate the electron-phonon coupling constant of the material.

- **Chapter 7**: Chapter 7 reports on the results I have obtained performing a synchrotron based ARPES investigation of $GeBi_2Te_4$ TI. By performing Linear-Dichroic (LD) ARPES I report a large dichroism in the bulk valence band which has been interpreted as an experimental evidence of the band parity inversion, which is a key mechanism for the realization of the topological phase.

- **Chapter 8**: The last chapter of this work is devoted to the study of $MoTe_2$, a material which has been proposed as the type II Weyl Semimetal (WSM). In the first part the literature concerning previous works on $MoTe_2$ is reviewed. In the second part I discuss the ARPES measurements performed on $MoTe_2$, aimed at revealing whether the surface state survives only in the low temperature non-centrosymmetric phase.

- **9**: The last chapter draws the conclusion and summarize the main results obtained.

Chapter 2

Time and Angle Resolved Photoelectron Spectroscopy

In the last decades we assisted to a strong development of spectroscopic techniques based on the photoelectric effect, these techniques belong to the class of Photoelectron Spectroscopies (PESs), and are nowadays widespread. Among PESs, the Angle Resolved Photoelectron Spectroscopy (ARPES) is one of the most advanced spectroscopic method to directly probe the electronic bands dispersion in solids. ARPES allows to measure the electronic band structure of crystalline solids usually over the entire Brillouin Zone (BZ) with high angular and energetic resolution.

Chapter 2 covers the following arguments. In the first part I provide a brief theoretical overview of ARPES at equilibrium: its kinematics and the conservations laws will be described and a formula for the photoemission intensity will be derived. In the second part I introduce the Time-Resolved ARPES (TR-ARPES), a recent implementation of conventional ARPES technique that allows to study the out-of-equilibrium electronic properties of solids. The last part of the chapter is devoted to the description of the experimental setup developed, focusing, in particular, on the the latest technical achievements.

2.1 ARPES at Equilibrium

2.1.1 Introduction

Photoelectron spectroscopic techniques are based on the photoelectric effect, originally discovered by Hertz in 1887 and then explained by Albert Einstein in 1905; its understanding granted him the Nobel Prize in 1922. This effect can be described as follows: let us consider a monochromatic radiation of frequency ν and energy $E = \hbar\nu$ impinging on a material having work function ϕ. When a photon carrying an energy E greater than the material work function ($\hbar\nu > \phi$) hits the sample, then the electron is excited in a free electron-like state and it can escape from the material. The maximum kinetic energy of the photoemitted electrons is $E_{kin} = \hbar\nu - \phi$. This happens for electrons lying exactly at the Fermi level, i.e. having null binding energy.

Photoemission is a complex quantum process which is considered to happen, in the more rigorous and realistic description, in a single step. Under suitable approximations the entire process can be modelled by using the so called three-step approach. In the case of the three-step model, two approximations are made: the so-called *independent-particle* picture and the *sudden* approximation. These assumptions are equivalent to disregarding both many-body interactions and the relaxation of the system during the photoemission process. In the *three-step* model, we can identify these steps [22]:

1. the impinging photon induces an optical excitation from an occupied initial state of energy E_{in} to an unoccupied state with energy E_{fin}.

2. the photoemitted electron travels through the bulk to the surface, undergoing several scattering events.

3. the sample surface acts as a potential barrier. For the electron to escape into the vacuum a matching between the electron wave function inside the solid and the free-electron like wave function outside the solid is required.

The three steps listed above provide only a qualitative description: from a quanto-mechanical point of view we should not ascribe the photoemission process to three independent events. For this reason, the *one-step* model is considered as the more rigorous description. Formally the correct modelling should describe an optical transition respecting the boundary conditions at

the edge of the solid and where the initial and final states are composed of many body wave functions. The initial state is one of the possible *N*-electron eigenstates of the semi-infinite crystal, while the final state must be one of the eigenstates of the ionized *(N-1)*-electrons.

In ARPES an electron energy analyzer collects photoelectrons emitted from the solid and measures their kinetic energy E_{kin} for a given emission angle. The knowledge of E_{kin} along with the emission direction allows to completely determine the momentum $\mathbf{K} = \mathbf{p}/\hbar$ of photoelectrons in vacuum. This direction is defined, with respect to the sample surface, in terms of the polar (θ) and azimuthal (ϕ) angles [23], as illustrated in figure 2.1. The modulus $|\mathbf{K}|$ is obtained by the E_{kin} value and the momentum components, parallel and perpendicular to the sample surface ($\mathbf{K}_\perp$ and $\mathbf{K}_\parallel$).

The *energy* conservation law, in a photoemission process, is defined within a non-interacting electron picture by:

$$E_{kin} = \hbar\nu - |E_B| - \phi \tag{2.1}$$

where E_B is the binding energy of electrons characterized by a specific electron density of states (DOS) and related to core electrons or bands states of the solid. The momentum conservation law relates the momentum $\mathbf{k}$ of electrons to the momentum $\mathbf{K}$ of photoelectrons. Within the three-step model, during the propagation across the surface the in-plane component of the wave vector $\mathbf{k}_\parallel$ is conserved because of the translational crystal symmetry is conserved at the surface. Hence, the wave vector component ($\overrightarrow{k}_{\parallel,in}$) of the wave function propagating in the solid corresponds to the wave vector component of the free-electron like wave function outside the solid ($\overrightarrow{k}_{\parallel,out}$). In particular the in-plane component $\mathbf{k}_\parallel$ of the momentum descends directly from the $\mathbf{K}_\parallel$:

$$\mathbf{k}_\parallel = \mathbf{K}_\parallel = \frac{1}{\hbar}\sqrt{2mE_{kin}} \cdot \sin\theta \tag{2.2}$$

Conversely, the normal component is not conserved, $\overrightarrow{k}_{\perp,in} \neq \overrightarrow{k}_{\perp,out}$ owing to the breaking of the translational symmetry at the surface. It is demonstrated that, by introducing the inner potential V_0, the normal component can be expressed as [23]:

$$\mathbf{k}_\perp = \frac{1}{\hbar}\sqrt{2m(E_{kin}\cos^2\theta + V_0)} \tag{2.3}$$

The term V_0 corresponds to the energy of the bottom of the valence band referenced to the vacuum level E_v. The value of V_0 can be determined experimentally. The procedure consists in detecting photoelectrons emitted at normal emission, (i.e. $\mathbf{k}_\parallel = 0$) while varying the incident

photon energy and thus the kinetic energy and $\mathbf{K}_z$. In the case of low-dimensional systems, like 2D-systems, the dispersion along the z axis is negligible. However, in the case of materials which present both 2D and 3D states, as Topological Insulators, the measure of the $\mathbf{k}_z$ can be relevant[1]. We will refer, in this thesis, to the *band mapping* as the measure of the band dispersion in the x-y plane, via the in-plane component ($\mathbf{k}_{\|}$).

In general the aim of an ARPES experiment is to measure the electronic dispersion $E(\mathbf{k})$ of electrons, thus the band structure of the material, by measuring the kinetic energy and momentum of electrons photoemitted in vacuum. It is worth noticing that only a portion of the photoelectrons can be exploited to extract information about the DOS of the sample. The conservations laws we introduce, applies only to the photoelectrons that do not undergo scattering events, maintaining unaltered their energy and momentum. Such electrons are called "primary photoelectrons"[2]. The mean free path, λ of the primary photoelectrons, presents a minimum in correspondence the energy range between 20 eV and 100 eV. At these energies, primary photoelectrons come from the topmost layers of the sample, hence come from the surface. The dependence of λ on the photon energy explains why the ARPES technique is said to be "surface sensitive" [24].

2.1.2 Photoemission Intensity

We can evaluate the ARPES intensity via both a semi-classical approach or through the quantum Green's function formalism. In both cases we treat the solid quantum-mechanically, however in the first case the electromagnetic field is represented classically by the vector potential $\mathbf{A}$. In this description the interaction between the electromagnetic radiation and the sample is accounted for by an hamiltonian perturbative term H_i. Within the dipole approximation, this operator can be written as:

$$H_i = -\frac{e}{mc}\boldsymbol{A}\cdot\boldsymbol{p} \tag{2.4}$$

[1]The dimensionality of surface and bulk derived states is experimentally determined by evaluating their $\mathbf{k}_z$ dispersion.

[2]The electrons mean free path λ depend on the photon energy, and do not depend in first approximation on the material.

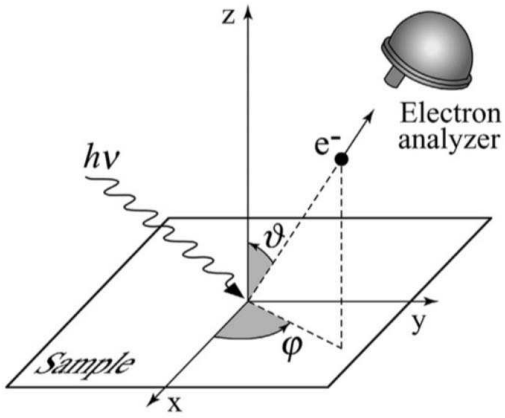

Figure 2.1: Geometry of an ARPES experiment. The polar (θ) and azimuthal (ϕ) angle specify the emission direction. [23]

with $\boldsymbol{A}$ being the potential vector and $\boldsymbol{p}$ the total momentum. The transition probability W_{fi} for an electron dipole optical transition between the N-electrons ground state (Ψ_i^N) and one of the possible final states (Ψ_f^N) can be expressed, by the Fermi Golden Rule as:

$$W_{fi} = \frac{2\pi}{\hbar}\left|\left\langle \Psi_i^N \right| H_I \left|\Psi_f^N\right\rangle\right|^2 \delta(E_f^N - E_i^N - h\nu) \tag{2.5}$$

We invoke here again the sudden-approximation and simplify the term W_{fi} by factorizing the wavefunctions in equation 2.5 into the photoelectron and the $(N-1)$- electron terms. We write the initial and final states as a product among ($\Phi_f^{\boldsymbol{k}}$) for photoelectrons and (Ψ_f^{N-1}) for the electrons:

$$\Psi_f^N = \mathcal{A}\Phi_f^k \Psi_f^{N-1} \tag{2.6}$$

$$\Psi_i^N = \mathcal{A}\Phi_i^k \Psi_i^{N-1} \tag{2.7}$$

where $\mathcal{A}$ is the antisymmetric operator that antisymmertrizes the wavefunction satisfying the Pauli principle. We can now write the matrix element in equation 2.5 in the following form:

$$\left\langle \Psi_f^N \right| H_i \left|\Psi_i^N\right\rangle = \left\langle \Phi_f^k \right| H_i \left|\Phi_i^k\right\rangle \left\langle \sum_m \Psi_m^{N-1} \middle| \Psi_i^{N-1} \right\rangle = M_{if}^k \left\langle \sum_m \Psi_m^{N-1} \middle| \Psi_i^{N-1} \right\rangle \tag{2.8}$$

Let assume the generic excited state of the solid left behind to have eigenfunction Ψ_m^{N-1} and eigen energy E_m^{N-1}. The total transition probability is given by the sum over all possible excited

states m. We introduce the annihilation operator $c_{\boldsymbol{k}}$ and write the the initial state as $\Psi_i^{N-i} = c_k \Psi_i^N$. This substitution formally leads to the "second quantization" formalism, fundamental to introduce the *one-particle spectral function*:

$$A^-(\boldsymbol{k},\omega) = \sum_m \left|\left\langle \Psi_m^{N-1} \right| c_{\boldsymbol{k}} \left| \Psi_i^N \right\rangle\right|^2 \delta(\hbar\omega + E_m^{N-1} - E_i^N) \tag{2.9}$$

The photoemission intensity measured as a function of the kinetic energy and momentum, given by $I(E_{kin}, \boldsymbol{k}) = \sum_{f,i} W_{f,i}$ is proportional to:

$$\sum_{f,i} \left| M_{f,i}^{\boldsymbol{k}} \right|^2 \sum |c_{m,i}|^2 \delta(E_{kin} + E_f^N - E_i^N - h\nu) \tag{2.10}$$

Where $c_{m,i} = \left\langle \Psi_m^{N-1} \right| c_{\boldsymbol{k}} \left| \Psi_i^N \right\rangle$. We can finally express the intensity of photoemission, as measured in a typical ARPES experiment, by the product of three independent terms, as:

$$I(E_k, \hbar\omega) = I_0(\mathbf{k}, \nu, \mathbf{A}) A(\mathbf{k}, \omega) f(\hbar\omega). \tag{2.11}$$

The firs term, $I_0(\mathbf{k}, \nu, \mathbf{A})$ is proportional to the squared matrix element $\left| M_{f,i}^{\boldsymbol{k}} \right|^2$. The second term, $A(\mathbf{k}, \omega)$, is the *one-particle spectral function*, which is usually represents the most important information that the ARPES technique allows to retrieve. This function, also known as *one-particle spectral density*, defines the probability of adding (if $E > E_F$) or removing (if $E < E_F$) an electron with energy E and wave vector **k** from or to the interacting N-electron system.
The third term, $f(\hbar\omega) = (\exp^{\frac{\hbar\omega}{k_B T}} + 1)^{-1}$, is the Fermi-Dirac function, which accounts for the statistical occupancy of the electronic states.

In some cases, the matrix element effects, accounted for by I_0, can lead to a complete suppression of the photoemission intensity. Hence, they become particularly important when performing polarisation-dependent ARPES investigations, usually indicated as Linear- and Circular-Dichroic ARPES (LD and CD-ARPES respectively). Here, we illustrate the case of the linearly polarized photons for the LD-ARPES investigation reported in this thesis work.

We can express the matrix element as a function of the unit vector along the polarization direction of the vector potential **A** of the incident photon, ε as:

$$\left| M_{f,i}^k \right|^2 \propto \left| \left\langle \phi_f^k \right| \varepsilon \cdot \hat{x} \left| \phi_i^k \right\rangle \right| \tag{2.12}$$

Selection rules depends mathematically on the parity of the operator and of the wavefunctions as well as on the experimental geometry. Let us consider as an example the photoemission from a

$d_{x^2-y^2}$ orbital, as sketched in fig. 2.2. The incoming beam direction defines the scattering plane (SP), while the high symmetry directions of the sample define the mirror plane(MP).

The detector, hence the analyzer entrance slit, lies in the mirror plane. The *p* and *s* polarizations are indicated by E_s and E_p respectively. The matrix element 2.12 must be even under reflection with respect to the mirror plane in order to have a non-vanishing photoemission signal [25]. The ideal situation is when the (SP) and (MP) are in the angular dispersion plane[3]. The final state wavefunction ϕ_f^k is mirror-symmetric and has even-parity under reflection. Hence the initial state ϕ_i^k has to obey precise selection rules, which can be summerized as:

$$\begin{cases} \phi_i^k - even \mapsto \epsilon \cdot \boldsymbol{A}(even) \\ \phi_i^k - odd \mapsto \epsilon \cdot \boldsymbol{A}(odd) \end{cases} \tag{2.13}$$

The photoemission intensity, as a result, can be suppressed or enhanced, due to these selection rules. From the above discussion we deduce that photoemission performed with different light polarizations allows, under proper geometrical conditions, to probe the parity of ground state wavefunction. This makes LD-ARPES the ideal tool to study the dichroism of different materials and systems or to exploit it in order to enhance the signal coming from a particular band.

[3]The energy dispersion plane of the analyzer sketched in fig.2.2 is orthogonal to the SP and MP planes, hence the angular dispersion plane is parallel to SP and MP.

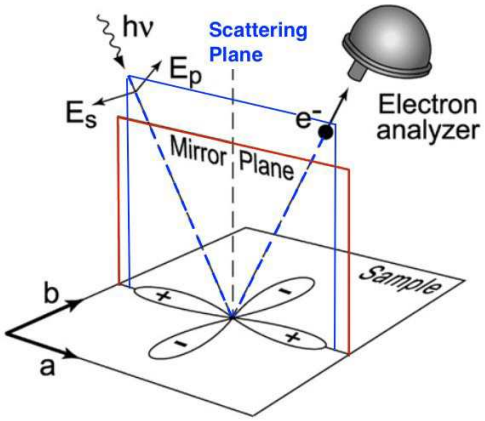

Figure 2.2: Photo emission from $d_{x^2-y^2}$ orbitals. The mirror plane (MP) in red is defined by the crystal symmetry and and the scattering plane (SP) in blue is defined by the beam geometry. Adapted from [25].

2.2 Out-of-Equilibrium ARPES

ARPES provides us the opportunity to directly probe the band structure of the materials, as those studied in the present thesis, at equilibrium. However, in order to study the evolution in time of the electronic properties, triggered by a photo-excitation, a time resolved approach is needed. In this section we introduce the time-resolved ARPES (TR-ARPES) along with some basic a formalism to interpret the experiments. After a brief introduction we will focus on the time-dependent description of the photoemission intensity and on the two-temperature (2T) model which has been adopted.

The advent of pico- and later femto-second laser sources, has triggered the development of time resolved optical spectroscopies. Gradually the time resolved approach has been extended to other spectroscopies, such as ARPES. The time-resolved ARPES (TR-ARPES) is based on a stroboscopic pump-probe approach, realized as follow. First, an intense laser pulse, called *pump*, excites the sample. After the arrival of the pump pulse, a weaker laser pulse, with photon energy sufficient to produce primary photoelectrons, called *probe*, is sent on the sample at a variable delay time, δt, with respect to the arrival of the pump pulse. By varying the delay time, the spectra corresponding to snapshots of the evolution of excitation and relaxation dynamics induced by the pump are detected using a suitable ARPES apparatus. The out-of-equilibrium properties can then be investigated by relating the electron dynamics to the specific band structure of the material.

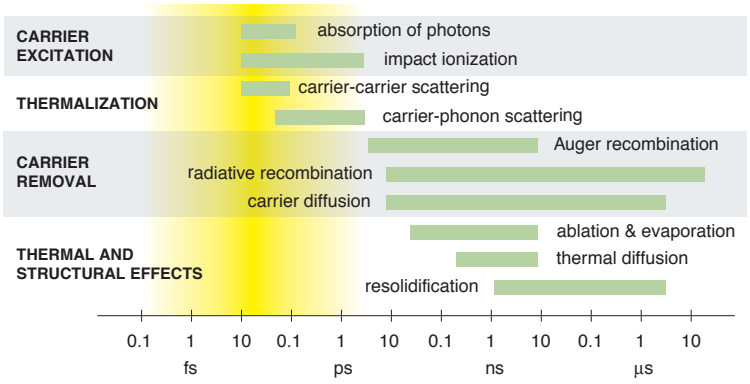

Figure 2.3: Representative time and energy scales of electronic and phononic processes in correlated materials. [33]

The past few years have seen a rapid diffusion of this technique, since it offers a direct insight into many-body interactions and in electron correlation properties out of equilibrium. The first set of systems investigated were mostly the charge density waves (CDW) materials [26, 27] and high temperature superconductors (HTSCs) like the cuprates [28, 29], and the picnitedes [30, 31].

Recently the scientific interest moved to the out-of-equilibrium properties of topologically non trivial systems like the Topological Insulators Bi_2Se_3 and Bi_2Te_3 [14, 12, 32]. Several pump-probe investigations have shown that during the non-equilibrium regime after the pump excitation, the energy transferred from the excited electrons to the rest of the system can be due to several independent or intertwined processes. Even though they can coexist on the same energy scale, they are often characterized by different time scales, hence distinguishable in the time domain. Figure 2.3 reports an overview of the main relaxation processes in solids on the femto- and pico-second time scale. In particular, in our work we are interested in the fast dynamics (below 10 ps), which involves electron-electron and electron-phonon interactions.

In developing phenomenological models for the TR-ARPES we use, as a starting point, the framework used to describe the equilibrium ARPES. In particular, we assume that after the

arrival of the pump pulse, the first and fastest process taking place is the carriers excitation. Due to the fast electronic response, the duration of this process is essentially imposed by the temporal length of the pulse (usually few tens of fs). Electrons, excited by the absorption of the IR photons pump, reach higher energy states in the conduction band, leaving holes in the valence band. Inter or intra-band excitations can occur, depending on the energy gap.
Excited carriers, which are in a non-equilibrium state after pump excitation, scatter among each others. It should be noted that carriers-carriers scattering process does not dissipate the extra energy but only causes a dephasing of the coherence between the excited particles (electrons and holes) leading to the theramalization of the electronic population.

The excited electrons get thermalized via ultrafast relaxation processes typically describable by a *hot*-thermal distribution function. In a very first approximation and in the absence of a more detailed knowledge of the relaxation processes, it is possible to consider the electron gas and the lattice like two independent but interacting systems evolving toward the equilibrium and to whom it is possible to assign two temperatures T_e and T_L. The electron system, after the light excitation, transfers the energy to the lattice via electron-phonon scattering processes with an effectiveness related to the electro-phonon coupling constant λ. We will see in section 2.2.2 that the time-constant of the cooling process of the electrons via interactions with the lattice depends, within a simple model, only on the electron-phonon coupling constant with no free parameters.

2.2.1 The Hot-Fermi Dirac Distribution

The photoemission intensity, as expressed by equation 2.11, is proportional to the product $A(\mathbf{k}, \omega) \cdot f(\hbar\omega)$. In order to extend this formalism to the non-equilibrium case and try to disentangle the time and energy domains, we introduce the following approximations.

In the general case, a photo-excited state is described by a many-body density matrix, in which off-diagonal terms refer to the optical coherence. Due to ultrafast scattering processes (faster than the temporal resolution of a typical pump-probe set-up) the density matrix can be actually considered diagonal [34]. Indeed, the electron-electron interaction, responsible for e-e scattering processes, can be assumed to be faster than the duration of both the pump and probe pulses ($\approx 100fs$).

We consider that primary electrons do not suffer any scattering events while escaping from the surface, as indicated by the *sudden approximation*. If these conditions are satisfied, we

can describe the electronic states and their time evolution separately in the energy and time domains respectively [35]. Hence, the time-dependent photoelectron spectrum is proportional to $A(\mathbf{k}, \omega, t) \cdot f(\hbar\omega, t)$ where A is the *one particle spectral function*, *t* is the delay time and f is an effective *hot*-Fermi Dirac distribution.
The temporal evolution of the spectral function contains informations about the modification of the photo-hole life-time along with the time evolution of the many-body correlations on the ultrafast timescale.

A detailed study of the spectral weight modification has been recently realized, thanks to the recent significant improvements in the detecting capabilities [36]. Concerning the statistical occupation of the electronic levels, the investigation of the time-evolution of the Fermi-Dirac (FD) distribution has been applied in both trivial and correlated materials. W.S. Fann et al. reported one of the first time-resolved photoemission spectroscopy studies in which the electron thermalization has been investigated and the concept of a hot Fermi-Dirac Distribution has been introduced [37]. Figure 2.4 shows their original results. They described the effect of the optical excitation on the electrons by a nascent electron distribution which deviates from a thermal FD function for at least one picosecond after optical excitation. However, by fitting a FD to the electronic distribution acquired at different delay times, and neglecting the "hot-electron tail" region, they have been able to extract an effective temperature T_e of hot electrons.

The comparison of the photoemission intensity acquired at delay t with the shape of a FD function that best approximates the measured electronic distribution shows that often, even in simple metallic systems, the electronic thermalization can happen on very long timescales, especially for what concerns a logarithmically small density of electrons at high kinetic energy. A qualitatively similar behaviour was found, for example, in the investigation of a cuprate superconductor, as reported in [28]. This kind of analysis have been improved with the availability of 2D detectors in combination with high resolution hemispherical electron analyzers. These allowed to extract energy- and momentum-dependent electronic distribution curves, indeed the occupied electronic bands of the crystal, with high energy and momentum resolution. A conventional and effective way to analyze the ARPES spectra in the momentum-energy domain is to extract the data at constant energy or at constant momentum.The Energy Distribution Curves (EDCs) provide the energy dispersion at fixed $\mathbf{k}$ values. Conversely the Momentum Distribution Curves (MDCs) give the momentum dependence at fixed energy values.

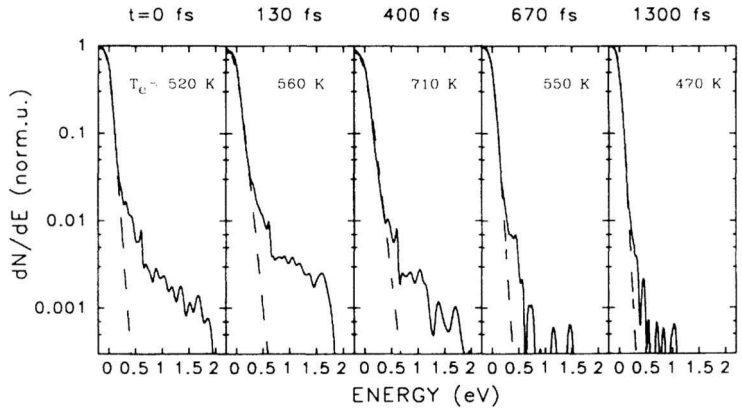

Figure 2.4: Electron Energy Distribution Curves vs energy at five delay times. The Fermi-Dirac fits (dashed lines) and the corresponding electronic temperature are shown. [37]

The EDCs are fitted by an expression containing a FD distribution, which provides the value of the chemical potential μ and of the the electronic temperature T_e. This represent a common procedure to analyze the transient dynamics in TR-ARPES experiments. As an example, we report, in figure 2.5, the measurements performed on Bi_2Se_3 TI and reported in Ref. [12]. The electronic temperature and chemical potential have been extracted from time dependent EDCs and fitted with a FD distribution.

In the panel (a) of fig. 2.5 the effect of the increasing temperature (thermal broadening) on the FD functions, that depends on the delay of the laser excitation, is shown. Their time evolution is reported in panels (b) and (c) respectively. Panel (d) reports the modification of the band structure of the material, that makes the Dirac cone clearly visible. The differential color scale (red-blue) is used to reveal the electron-holes transient population after the pump excitation. Negative values (blue) corresponds to a loss of photoemission intensity (excess of holes) while positive in red indicates an increase of the electrons number.

2.2.2 Two- and Three-Temperature Models

This paragraph is devoted to the description of the so-called Two-Temperature (2T) model, which as been developed by Anisimov [38] and Allen [39]. In the end of this section we introduce an extension of this model, known as Three-Temperature (3T) model, initially proposed

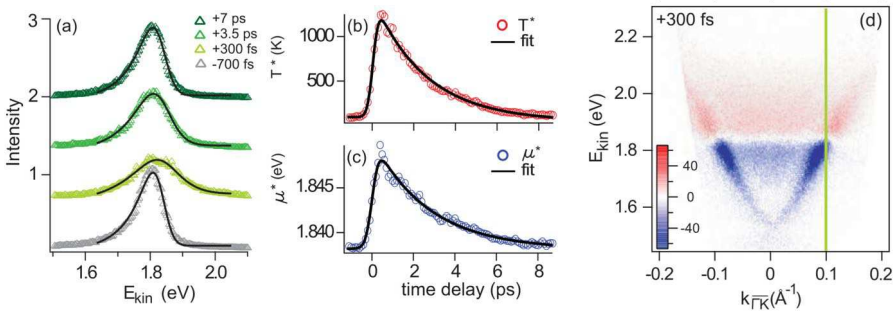

Figure 2.5: Time-resolved ARPES on Bi_2Se_3 TI [12]. EDCs at different delay time in panel (a) extracted along the direction shown in panel (d). Electronic and chemical potential in panel (b-d), derived by the fit of the hot FD distributions. Panel (d) is a the differential image of the band structure acquired 300 fs after the pump excitation.

by L. Perfetti [28].

The 2T model describes, within some basic assumptions, the physics of a pump and probe experiment allowing to extract, in some cases and under specific assumptions, the electron-phonon coupling constant of the material from the measured relaxation mechanisms. The first important requirement is that the electron and phonons distribution functions can be approximated to the local equilibrium distribution given in the first case by the Fermi-Dirac distribution function (FD) and in the second case by the Bose-Einstein distribution function (BE).

Under these assumptions the energy balance for a metal absorbing a laser pulse can be approximately described by a minimal and phenomenological system of coupled differential equations. The relevant excitation and relaxation processes shown in figure 2.3 constitute the physical picture withstanding the following system of equations:

$$\begin{aligned} \frac{\partial T_e}{\partial t} &= \frac{S}{C_e} - \frac{G}{C_e(T_e - T_l)} \\ \frac{\partial T_l}{\partial t} &= -\frac{G}{C_l(T_e - T_l)} \end{aligned} \tag{2.14}$$

where T_e, T_l are the electronic and lattice (phonon) temperatures previously defined. The coupling constant between the electron and the phonon systems is $G = \gamma_{e-ph} C_e$, sometimes also expressed directly by γ_{e-ph}. The electronic specific heat is $C_e = \gamma_e T_e$, being γ_e its linear coefficient. C_l is the lattice specific heat and *S* is the absorbed power, with the Gaussian temporal

profile of the laser pulse.

The solution of the system is a single exponential function with time-constant $\tau = \frac{1}{\gamma_{e-ph}}$. The term τ and the electron-phonon coupling constant λ are related [39]. λ indeed can be directly obtained by τ once the mean phonon energy $\langle \hbar^2\omega^2 \rangle$ and the electronic temperature T_e are known.

$$\gamma_{e-ph} = \frac{3\lambda \langle \hbar^2\omega^2 \rangle}{\hbar\pi k_B^2 T_e} \tag{2.15}$$

thus:

$$G = \gamma_{e-ph}\gamma_e T_e = \frac{3\gamma_e}{\hbar\pi k_B^2}\lambda \langle \hbar^2\omega^2 \rangle \tag{2.16}$$

k_B is the Boltzmann constant and ω is the frequency of the phonon mode. To comprehend the limits of the Allen formula 2.15 and to further improve the accuracy of the 2T model, it is convenient to start from a general description of the electron thermal energy decay rate, which can be expressed as:

$$\frac{\partial E_e}{\partial t} = 2\pi N_c N(E_F) \int_0^\infty d\Omega \alpha^2 F(\Omega)(\hbar\Omega)^2[n(\Omega, T_l) - n(\Omega, T_e)] \tag{2.17}$$

where N_c represents the number of unit cells of the material, $N(E_F)$ is the density of states (both spins per unit cell) and $n(\Omega, T_j)$ stands for the BE distribution functions ($j = e, l$). $\hbar\Omega$ is the phonon frequency and $\alpha^2F(\Omega)$ is the Eliashberg function, where the electron-phonon coupling $\lambda = 2\int_0^\infty d\Omega 1/\Omega \alpha^2 F$ [39]. The energy of the electrons can be generically rewritten as $E_e \approx E_0 + \frac{1}{2\gamma_e T_e^2}$. E_0 indicates the system point zero energy at $T = 0$. The right-end side of equation 2.17 can be evaluated via different approximations.

The first, also known as "*high temperature limit*", consists in a Taylor expansion of the Bose-Einstein distributions $n(\Omega, T_j)$ in terms of $\hbar\Omega/k_B T_j$. This assumption is valid when T_e and T_l are much higher than the maximal phonon energy $\hbar\Omega$, that matches the Debye energy $\hbar\Omega_d$. Hence, when $k_B T_j \gg \hbar\Omega_d$, we can simplify expression 2.17 and obtain obtain the system of equation 2.14 previously described.

Several complex systems cannot be treated as simple metals from the point of view of the electron-lattice interaction. This is the case of compounds which present a strongly anisotropic

coupling or which relax via different scattering processes. In the general case, the electronic temperature may relax through more than one single exponential decay. Perfetti et al. proposed the so called Three-Temperature model (3TM) to solve this problem and to qualitative interpret their time-resolved ARPES result on a HTCS [28]. Indeed, they revealed for these compounds a peculiar double-exponential decay of the electronic temperature. The basic idea that allowed to interpret this finding is that the lattice can be divided in two subsystems: a subset of *hot*-phonons which strongly interact with the electrons and the "cold" lattice, which is weakly coupled.

We associate to the hot phonons the strongly coupled modes (a fraction f of the total modes) and to the cold lattice the nearly non interacting $(1-f)$ phonon modes. During first femtoseconds after the excitation the electronic distribution converges to a thermalized hot Fermi Dirac distribution, and then the electron relaxation with the hot-phonons takes place. Both phononic and electronic populations relax on the ps time scale. The relaxation process follows with the mutual interaction of the two independent phonon subsets, governed by phonon-phonon anharmonic scattering processes.

The main hypothesis and simplification in this model concerns the phonon spectrum for the strongly-coupling phonons, which is described by the Einstein model. The energy decay rate (2.17) can be then rewritten by considering a non-dispersing distribution for the phononic modes given by $F(\Omega-\Omega_0) \propto \Omega-\Omega_0$, so the rate for the energy transfer becomes $\int_0^\infty d\Omega\Omega^2\alpha^2F(n_e - n_p)$ with $n_j = (e^{\Omega/k_bT_j-1})^{-1}$. Since the dimensionless electron-phonon coupling constant is defined as $\lambda = 2\int_0^\infty d\Omega 1/\Omega\alpha^2F$, the system of the rate equations can be written as:

$$\begin{aligned}
\frac{\partial T_e}{\partial t} &= -\frac{3\lambda\Omega_0^3}{\hbar\pi k_b^2}\frac{(n_e-n_p)}{Te} + \frac{S}{C_e} \\
\frac{\partial T_p}{\partial t} &= \frac{C_e}{C_p}\frac{3\lambda\Omega_0^3}{\hbar\pi k_b^2}\frac{(n_e-n_p)}{Te} - \frac{(T_p-T_l)}{\tau_\beta} \\
\frac{\partial T_l}{\partial t} &= -\frac{C_p}{C_l}\frac{T_p-T_l}{\tau_\beta}
\end{aligned} \tag{2.18}$$

The n_j are the Bose-Einstein distributions at the temperature T_j, while $C_j(T)$ represents the electrons ($j = e$), hot phonons ($j = p$) and cold phonons ($j = l$) specific heat. For the electronic specific heat, it holds $C_e = \gamma_e T_e$. In this model the phonon-phonon anharmonic decay is accounted for phenomenologically by the time constant τ_β, describing the second relaxation timescale observed in the experimental data for $T_e(t)$. We stress that in this model the electrons

are considered coupled only to one single phonon mode at frequency $\Omega = \Omega_0$. Conversely, in this formulation no approximations are made on the Bose-Einstein statistics, hence the model is valid for any temperature $T_j(t)$.

It is worth anticipating here that our experiment on $\mathrm{SmB_6}$ motivated us to develop a novel formulation of the 2TM, since the common assumptions made in the conventional 2TM were not satisfied. In particular, the experimentally determined electronic temperature $T_e(t)$ was found to be considerably lower than the Debye temperature of the material (T_D= 373 K ref.[40]), hence the *high-temperature limit* cannot be considered as a correct approximation in our situation. Conversely, as it will be discussed in chapter 6, in $\mathrm{SmB_6}$ it is a reasonable assumption to consider the electrons coupled only to a peculiar phonon mode, with the lattice specific heat calculated through the approximated Einstein model. We then derived a modified version of the 2TM, that writes:

$$\begin{aligned} \frac{\partial T_e}{\partial t} &= -\frac{3\lambda\Omega_0^3}{\hbar\pi k_b^2}\frac{(n_e - n_l)}{Te} + \frac{S}{C_e} \\ \frac{\partial T_l}{\partial t} &= \frac{C_e}{C_l}\frac{3\lambda\Omega_0^3}{\hbar\pi k_b^2}\frac{(n_e - n_l)}{Te} \end{aligned} \tag{2.19}$$

2.3 Experimental Setup

Time-resolved ARPES is a technique which requires a specifically designed UHV and optical setup to be correctly operated. The next section introduces the Time-resolved ARPES end-station we used for the experiments reported in this thesis. In particular on the new optical setup that has been recently implemented.

2.3.1 The T-Rex ARPES End-Station

A typical ARPES end-station is composed by four main elements: (a) the vacuum system; (b) a sample manipulator/ cooling system; (c) a light source; (d) a photoelectron analyzer. Additional apparatuses can be also integrated with these essential components in order to prepare, treat and manipulate under UHV conditions the samples.

The vacuum system of the TR-ARPES end station at the T-ReX Laboratory includes three interconnected vacuum chambers, for introducing the samples under controlled conditions, for

preparing and manipulating the samples and the main chamber hosting the main samples manipulators, a low energy electron diffraction (LEED) diffractometer and a hemispherical electron analyzer. The samples are loaded in the the *load lock fast entry* chamber which can be quickly pumped down to a base pressure in the 10^{-8} mbar range.

The preparation chamber, next to the load-lock, allows to cleave the sample in ultra high vacuum environment, for providing an atomically clean and fresh surface. The average pressure is of the order of 10^{-11} mbar. After suitable preparation, the samples can be transferred to the main experimental vacuum chamber, also having a base pressure in the 10^{-11} mbar range. The preparation chamber contains other important apparatuses, like a Low Energy Electron Diffraction (LEED) spectrometer, an Argon sputtering gun and evaporation sources.

The main experimental chamber is equipped with an automated manipulator with 6 degrees of freedom. The manipulator hosts a cryostat, which allows the sample temperature to be controlled and stabilized in the range $35 - 350$ K, when liquid helium cooling is used. An electron gun and a Helium discharge lamp are also available. The main chamber is completed by a Specs Phoibos 225 equipped with a 2D-CCD detector hemispherical electron energy analyzer, that allows high energy and momentum resolution when operated in the ARPES mode.

Time-resolved ARPES experiments require the use of ultrashort laser pulses with specific features, like a short temporal duration and a proper photon energy. Typical ultrafast laser sources produce trains of light pulses in the near-infrared spectral range, with a temporal duration of ≈ 100 fs. In particular, the fundamental emission of a Ti:Sa laser is at 800 nm, i.e.1.55 eV. This photon energy is often used for the pump pulse, whereas the probe pulse must then be obtained via non-linear optical crystals in order to obtain a photon energy suitable for the linear photoemission. Typically, the fourth harmonics of the Ti:Sa, at a wavelength of 200 nm (6.2 eV), is the lowest harmonics that satisfies this energy condition (2.1).

To perform the experiments which are presented in this thesis work, we have adopted, in combination with the vacuum apparatus, a pump-probe optical setup which scheme is reported in figure 2.6. We call *setup-1* the standard optical setup, and *setup-2* a novel optical setup presenting improved characteristics and performances. In setup-1 the fundamental beam is split into two beams by BS1: the reflected beam is used as the pump, while the transmitted beam is used to generate the fourth harmonics probe. After two mirrors (M1 and M2) the transmitted beam goes through a second beam splitter BS2 before being focused on the second harmonic

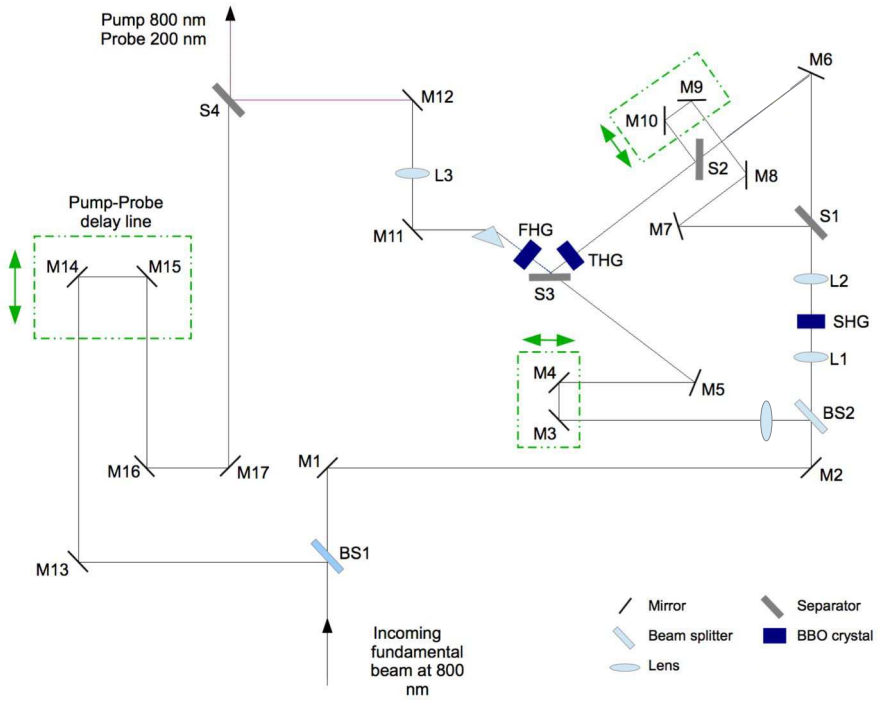

Figure 2.6: Scheme of the first pump-probe setup (setup-1). [41]

generation (SHG) crystal, a type I-BBO crystal. An optical separator (S1) divides the second harmonics (SH) from the fundamental (F) into two different optical paths.

The fundamental and the second harmonics beam are then recombined on a second BBO crystal, with the proper polarization and temporal coincidence, in order to generate the third harmonics by a sum frequency generation process. The third harmonics beam interacts with the 800 nm beam on a third BBO crystal to generate the fourth harmonics at 200 nm. The fourth harmonics is finally separated from the other harmonics by means of a prism. In the last part of the optical path, a mirror focuses pump and probe beams on the sample.

2.3.2 New Pump and Probe Optical Setup for 4^{th} Harmonics Generation with a Prism Compressor

In order to improve the efficiency and the stability of the harmonics generation process we have designed and realized a new optical setup (setup-2) represented in figure 2.7. The image shows

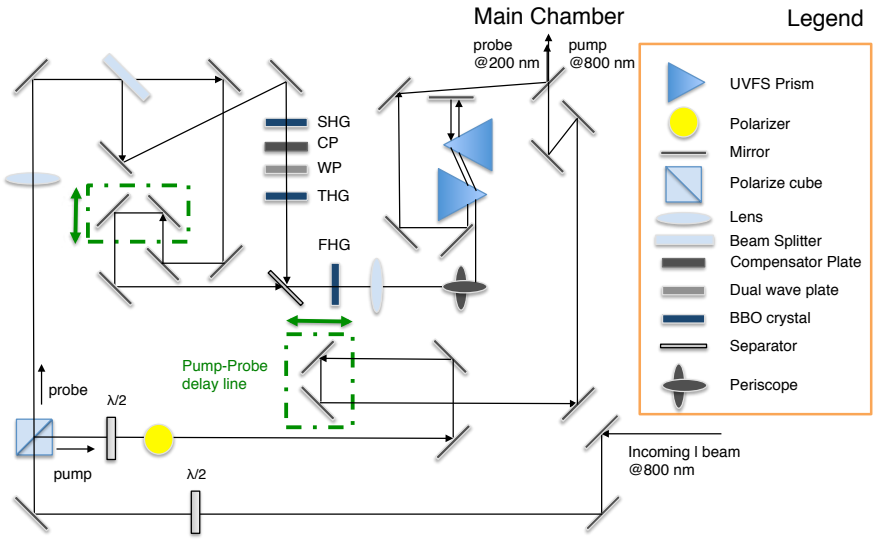

Figure 2.7: Scheme of the new pump-probe setup-2 equipped with the optical compressor. The optical components are indicated in the legend.

a sketch of the optical path with the optical components.

The main difference with respect to setup-1 consists in a new optical scheme for the third harmonics generation and in the presence of a prisms compressor. The effective overall size has also been reduced. The fundamental of the laser, the second and the third harmonics are collinear and are generated along the same optical path. This arrangement, which is sketched in figure 2.8, requires no beam splitters and mechanical delay slits. The setup for THG is much simpler and employs less optical components that those needed in setup-1.

The fact that the temporal and spatial overlap on the THG crystal is obtained by default makes this optical design almost unaffected by possible small accidental misalignments and the THG results stable with respect to slow drifts of the beam position. In particular, the beam at 400 nm, after being generated by the first BBO, passes trough a calcite velocity delay compensator with a negative chirp. A dual wavelength wave-plate rotates the polarization of the fundamental beam only before the second (THG) BBO crystal. The beams collinearity leads to an improved spatial overlap thus providing a better efficiency of the sum frequency generation. The improved conversion efficiency achieved in the collinear generation scheme allows to use thinner BBO crystals (by a factor 2 to 3).

Thanks to a considerably higher "mixing acceptance bandwidth", the bandwidth of the THG pulse is increased, sustaining shorter pulses. This is also the case of the FHG beam. A larger bandwidth (by about a factor 2 with respect to setup-1) can lead to a much better time-resolution in TR-ARPES experiments (at the expense of a reduction in the energy resolution), provided that the FHG pulse is correctly controlled. Indeed, a large bandwidth pulse is more subject to temporal broadening when passing through optics such as lenses and windows, especially in the UV range, where the refractive index of optical material is strongly wavelength dependent.

Despite all the optics are carefully chosen for UV light, a prism compressor is fundamental to compensate for the chirps that would be acquired by the FHG pulse while propagating through optical components. The compressor also works as a wavelength separator, allowing to extract the FHG from the collinear lower harmonics. Finally, a pulse compressor allows to approach the "transform-limit" for the time-bandwidth product, hence leading to the maximal time resolution for the given energy bandwidth. The next section is devoted to the description of the pulse compressor. The temporal duration of the laser pulses is of paramount importance in time-resolved techniques since it determines the final temporal resolution. In a time-resolved ARPES experiment, both time and energy must be accounted.

Cross-correlation measurements, which have been previously performed on the setup 2.6, reveal that the probe pulse is subjected to a considerable temporal broadening. By calculating the transform limited duration Δt_{TL} of the pulse from the FWHM of the spectrum, we obtain $\Delta t_{TL} \simeq 100 fs$. The "effective" duration is instead equal to $\Delta t_{out} \simeq 330 fs$. Hence, we have decided to recompress the pulse by equipping the setup-2 with a prism compressor displaced nearby the fourth harmonic generation. The aim is to optically compress the pulse in time while optically compensating the broadening of the probe pulse.

We notice that the pulse duration can not be arbitrary short, without increasing the pulse bandwidth. The uncertainty principle for a transform-limited Gaussian pulse, expressed by the product $\Delta\nu\Delta t \simeq 0.44$, must be considered. However, reducing the gap between Δt_{TL} and Δt_{out}, with a prism compressor, has obviously no effect on the bandwidth of the pulses, hence the energy resolution of the setup is unaffected. This, indeed, accounts for several contributions in addition to the pulse bandwidth, as the temperature of the system, the electric noise and the analyzer resolution. Hence, we expect that the temporal resolution can be significantly improved while keeping unchanged the energy resolution.

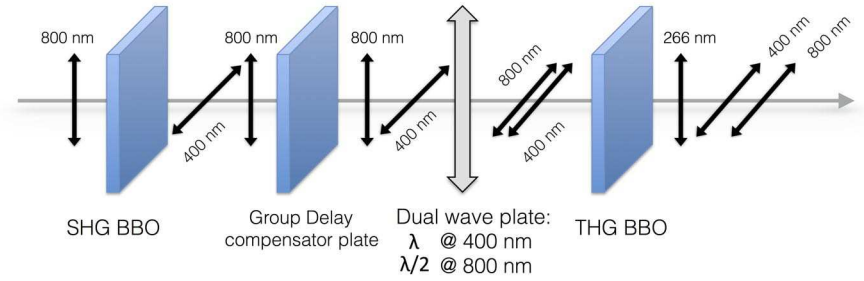

Figure 2.8: Collinear optical third harmonics generation scheme.

In order to design an effective prism compressor let us consider a gaussian pulse characterized by a frequency bandwidth $\Delta\nu$ and an effective temporal length Δt_{out}. When a laser pulse travels through a dispersive media the spectral components will propagate with different group velocities giving rise to an effect known as chirping[4] effect. This dependence is described by the group delay dispersion (GDD), which is related to the second derivative of the refractive index with respect to the wavelength and to the length L of the media by:

$$GDD = \frac{\lambda^3}{2\pi c^2}\left(\frac{d^2 n}{d\lambda^2}\right) L \tag{2.20}$$

This quantity can be completely expressed in terms of experimental observables (i.e. pulse width and spectrum) as [42]:

$$GDD_{pulse} = \frac{1}{4\ln 2}\sqrt{\left(\frac{c_b \Delta t_{out}}{\Delta\nu}\right)^2 - \left(\frac{c_b}{\Delta\nu}\right)^4} \tag{2.21}$$

where $\Delta\nu = c\Delta\lambda/\lambda^2$ and $c_b \simeq 0.44$ is the time-bandwidth product for a gaussian profile. The group delay dispersion affects the temporal duration of the pulse.

By considering this, we start by evaluating expression 2.21, substituting the parameters measured for the probe pulse. The result is $GDD_{pulse} \simeq 10984\ fs^2$, by adopting the following parameter: $\lambda = 197$ nm, $\Delta\lambda = 0.59$ nm, $\Delta t_{out} = 330$ fs and $c_b = 0.441$. If we compare three pulses with the same central wavelength and bandwidth but with a positive, a negative and without any chirp, the minimum temporal duration corresponds to the one which shows zero

[4]When a light pulse propagates through a dispersive media high and low frequency of the spectrum are selectively delayed, thus the resulting pulse can assume a positive or negative chirp (becoming positively ore negatively chirped).

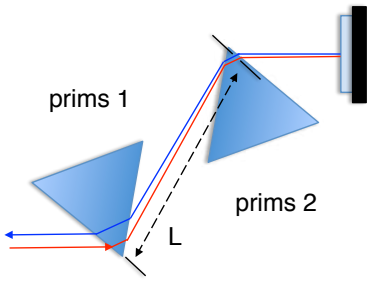

Figure 2.9: Sketch of the folded geometry of the two-prism compressor. Red and blue are the incoming and out coming beams respectively.

GDD (chirp). To realize this condition it is necessary to introduce a negative chirp, in order to balance the positive chirp acquired by the pulse when traveling through optical elements.

A negative chirp can be introduced only by the angular dispersion of the beam through the prisms. In this way, with a prism compressor, it is possible to compensate for the pulse chirp, by setting:

$$GDD_{pulse} = -GDD_{prism} \tag{2.22}$$

The negative GDD_{prism} can be expressed via the equation:

$$GDD_{prism} = \frac{\lambda^3}{\pi c^2}\left(-4L\left(\frac{dn}{d\lambda}\right)^2 + 4D_{1/e^2}\left(\frac{d^2n}{d\lambda^2}\right)\right) \tag{2.23}$$

We have adopted this expression to estimate the distance L between the apexes of the two prisms. The first and second derivative of the refractive index[5] with respect to the wavelength are $\frac{dn}{d\lambda}^2 \simeq 0.151 \cdot 10^{-2} nm^{-1}$ and $\frac{d^2n}{d\lambda^2} \simeq 4.47 \cdot 10^{-5} nm^{-2}$ for UVFS, the materials of which the prisms considered are made. The estimated beam diameter is $D_{1/e^2} \approx 2$ mm.

Through relation 2.22 we have estimated that $L \simeq 83.6$ mm. To arrange the compressor, we have adopted a "folded" geometry, which consists in using two prisms with a folding mirror placed after the second, as indicated in figure (2.9). The reflection losses can be minimized if the beam enters and exits each prism close to the Brewster angle. The polarization of the incoming beam should then be *p*, hence we introduced a periscope in order to rotate the *s* polarization obtained after FHG.

[5]The prisms designed for 200 nm are in UV fused silica

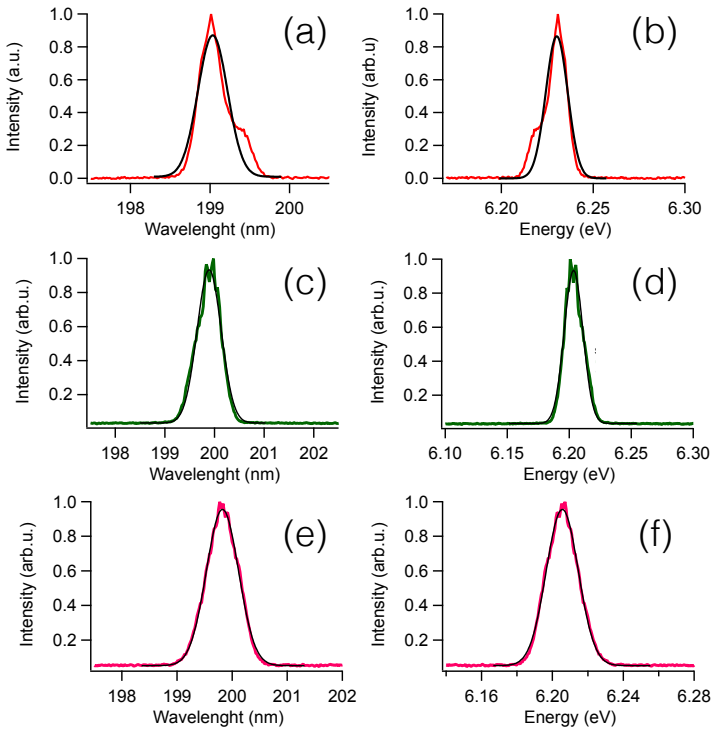

Figure 2.10: (a-b) Spectrum of the fourth harmonics probe pulse generated in setup(1). (c-d) Spectrum generated with a 500 μm thickness BBO crystal in setup-2(a) and (e-f) generated in setup-2(b) by using a 100 μm BBO crystal. Coloured curves represents spectra in unit of nm and eV and black curves are the fit functions.

2.3.3 Pulse Characterization: Bandwidth and Temporal Duration

The characterization of the setup-2 performances starts with the measurements of the bandwidth of the fourth-harmonics pulses, that determines both the ultimate energy and time resolutions that can be achieved in a time-resolved ARPES experiment. The spectra have been acquired through a high resolution monochromator.[6] The normalized curves, together with the fit functions, are reported in figure 2.10. The data have been fitted with a Gaussian function in order to extract their FWHM. Results obtained from the fits are summarized in table 2.1, and are expressed in unit of both nm and eV.

[6]The model is a M266 monochromator and spectrograph by Solar Laser System. We used a 2400 grooves/mm grating. Target resolution is 0.08 nm.

	$\lambda_0(nm)$	$\Delta\lambda(nm)$	$E_0(eV)$	$\Delta E(eV)$	$\Delta(t)_{TL}$ (fs)
setup-1	199 ± 0.1	0.4 ± 0.1	6.23 ± 0.003	0.013 ± 0.003	145 ± 35
setup-2 (a)	199.8 ± 0.1	0.6 ± 0.1	6.21 ± 0.003	0.017 ± 0.003	97 ± 15
setup-2 (b)	199.8 ± 0.1	0.7 ± 0.1	6.20 ± 0.003	0.021 ± 0.003	84 ± 11

Table 2.1: FWHM values extracted from the gaussian fits shown in figure 2.10. Setup-2(a) refers to the use of a 0.5 mm thickness BBO crystal while setup-2(b) refers to a 0.1 mm thickness. The error has been evaluated by considering the instrument accuracy and then propagated on the calculated quantities.

We have tested two BBO crystals for the fourth harmonics generation of different thickness. The first is a 0.1 mm of thickness BBO, while the second is a 0.5 mm thickness crystal. The two cases are indicated in table 2.1 with *setup-2(a)* and *setup-2(b)* respectively.
The transform limited duration of the pulses $\Delta(t)_{TL}$, has been calculated by recalling the time-energy uncertainty principle[7]:

$$\Delta\lambda = \left(\lambda^2 \frac{C_B}{c}\right) \frac{1}{\Delta t} \tag{2.24}$$

By comparing values reported in table 2.1, we notice that the bandwidths of pulses generated with the new setup-2 are wider with respect to the older setup-1. The minimal (transform-limited) pulses durations $\Delta(t)_{TL}$, according to the increased bandwidth, are shorter.

As expected, the thickness of the BBO crystal plays a crucial role in determining the bandwidth of the harmonic pulse. This fact descends from the the mixing acceptance bandwidth of a non-linear crystal, which is inversely proportional to its thickness. Hence, a thinner non-linear crystal is expected to produce pulses with a wider bandwidth (provided the mixed beams can sustain it). As reported in the last raw of table 2.1, the bandwidth of the pulse produced with the 0.1 mm BBO crystal is the widest, and equals to 21 meV. The estimated transform limited pulse duration equals 84 fs.

To measure the ultimate temporal duration of the probe pulse after compression, we have performed a TR-ARPES experiment (pump at 1.55 eV, probe at 6.2 eV) and we have extracted the time-dependent photoemission intensity from integrated in an energy-momentum window (E,k) above the Fermi level where no electronic band structure features are present (the target sample

[7] c is the the speed of light constant.

was Bi_2Se_3). In this condition, the transient electron signal closely resembles a cross-correlation signal, since no true final states are involved. We then extract the FWHM of the cross-correlation of the first harmonics (pump pulse) and fourth harmonics (probe pulse), by performing a fitting of the time-resolved photoemission signal with a function composed of an exponential decay convoluted with a Gaussian function accounting for the temporal resolution (cross-correlation). In this way, we can obtain an excess estimate of the temporal cross-correlation. In order to extract the duration of the probe pulse only, we need to deconvolve the duration of the infrared pump-pulse from the cross-correlation, with the following expression:

$$\Delta t_{conv} = \sqrt{{\Delta t_{probe}}^2 + {\Delta t_{pump}}^2} \tag{2.25}$$

The photoemission intensity, and its fit are shown in fig. 2.11. The duration of the convoluted pulse obtained from the rise-time is $\Delta t_{conv} = 125 \pm 30$ fs. The bandwidth of the pump pulse is $\Delta\lambda = 31$ nm at 790 nm, giving a transform-limited duration $\Delta t_{pump} = 30$ fs. However, the actual value of the duration of the infrared 1.55 eV beam equals 60 fs. Hence, from relation 2.25, we estimate a maximal duration (transform-limited) for the probe pulse of $\Delta t_{probe} = 109$ fs. Finally, if we compare the actual probe pulse durations measured via the photoemission experiment with the transform-limited values reported in table 2.1, we can conclude that the prisms compressor is operating properly and the resulting probe compression can be considered more than satisfactory.

2.3.4 Pulse Characterization: Beam Profile

In addition to the pulse temporal duration, the optical fluence[8] of laser beam which impinges on the sample, represents a fundamental parameter we must control during the time-resolved photoemission experiments. To correctly determine it, a careful estimation of the beam diameter is needed. We have measured the pump and probe beams profile in a position corresponding to the focal spot on the sample, by means of the knife-edge technique. Table 2.2 reports the results for both beams and the two setups. In both setups, the pump spot diameter is larger than the probe one, as required in pump-probe experiments. The ratio between the spot sizes of pump and probe is of the order 1.5.

[8] Optical fluence, defined as the optical energy delivered per unit area ($joule/cm^2$).

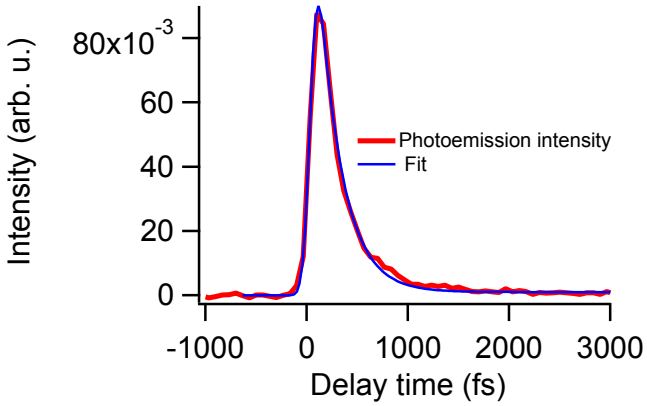

Figure 2.11: (red) Time-dependent photoemission intensity extracted from empty states above the Fermi level. (blue) Fit function.

Setup version	**Beam**	**FWHM** (μm)
1	probe	177.1 ± 15
1	pump	158.4 ± 1.3
2	pump	219 ± 3.5

Table 2.2: The beams spot dimension obtain by the knife-edge technique. The errors are equal to one standard deviation of the fit coefficients.

Chapter 3

Non-Trivial Topological States in Complex Layered Materials

This chapter deals with the discovery of materials with novel topological phases through the definition of the basic principles necessary to distinguish trivial and topological states. In the second part I briefly review the "state-of-the-art" of the time-resolved ARPES on the prototypical topological compounds Bi_2Te_3 and Bi_2Se_3. The main results of the experimental investigations which have been performed so far are reported. This review will focus, in particular, on the works that have inspired and stimulated our research, whose results will be presented in the following chapter.

3.1 Topological Insulators

The prediction and the discovery of 3D Topological Insulators (TIs) is based on the definition of quantum Hall (QH) states and quantum spin Hall (QSH) insulators. Those systems can be considered as the precursors of these new topological phases. In this chapter the historical development that has lead to the study of TIs is presented. In addition, we provide the theoretical background and the basic concepts necessary to define the nontrivial topological phase, including the definition of topological invariants, which are fundamental quantities necessary for the classification of topological materials.

3.1.1 Quantum Hall States

The different states of matter have been classified, up to 1980, according to their ground state symmetry properties. For instance, crystalline solids and ferromagnetic systems, are characterized by the breaking of spatial translational symmetry and time-reversal (TR) symmetry, respectively. The discovery in 1980 of the Quantum Hall (QH) effect by Klaus von Klitzing has changed this perspective [2]. The two dimensional QH state is commonly regarded as the first realization of a novel topological phase of matter. This is due to the fact that its behaviour depends only on its topology and not on its symmetry and geometrical properties [43].

A QH state is a two-dimensional insulator which under the effect of intense magnetic field and low temperature presents anomalous metallic charge transport at the boundary. The Hall conductivity is quantized, as it assumes only integer values which are multiple of the quantity $\sigma = \nu e^2/h$ [1]. The origin of such quantization has been described by Laughlin, who has demonstrated that this phenomenon can be regarded as a subtle manifestation of the principle of gauge invariance [44]. In a QH state while the bulk is insulating electrons can travel at the edges. Electron currents are also spatially separated, as represented in figure 3.1 panel (a). These circulating edge states, unlike ordinary metallic states, are robust against the presence of impurities. This mechanism can be explained trough a phenomenological picture as follows. When an electron encounters an impurity, it simply takes a detour and keeps going in the same direction. This electron, due to the defined direction of propagation of the metallic edge states, can not be scattered or reflected back. In fact, any scattering event, would revert the direction of propagation, "transferring" the electron from one edge to the opposite one. However, electrons have no available states with opposite chirality to scatter in.

The typical definition of insulator, which is based on the presence of a band energy gap, can not be adopted to classify QH systems. In fact these materials present, at the same time, a bulk gap and conductive edge states, hence a new generalized definition is needed. Fu and Kane proposed that a topological non-trivial state can be consider as a system in which the electronic properties, and so the response to an external magnetic field for the QH case, are local. For instance, if we apply the magnetic field to a materials of different shapes we can see the concept of locality at play.

Let us consider a rectangular shape as a plate and an annular shape as a donut. A magnetic

[1] ν is the integer factor, also known as "filling factor".

field is applied perpendicular to the flat face in the first case, and trough the hole in the second, i.e. out of the sample surface. For both geometries in the QH state the metallic conductance is supported by the edge states. The response is not local in the sense that depends not only on the sample region, where the field is directly applied as for the rectangular shape, but also on the region surrounding the sample, as in the case of the magnetic field trough the hole of the donut in the second shape. The background needed to introduce important quantities as the topological invariants, requires to abandon the concept of "locality" in favour of the concept of "adiabaticity".

Insulators are described by an Hamiltonian which can be adiabatically transformed into the one of an isolated atom (atomic insulator), without undergoing any phase transition or ground state modifications. The concept of adiabatic transformation of an Hamiltonian $\hat{H}(t)$ is of paramount importance, since it allows to introduce the concept of Berry's phase [45]. The Berry's phase is a geometrical phase that the wavefunction describing the system acquires over the course of an adiabatic cycle. This parameter discriminates the QH state from a trivial atomic insulator. The Berry's phase can assume, for a QH system, π or $(2n+1)\pi$ values, while in the case of an atomic insulator, this parameter can only be equal 0 or 2π.

From the adiabatic evolution of the hamiltonian, and the resulting Berry's phase, several quantities can be introduced to describe the TKNN number [46]. This quantity, as we will see in details, constitutes the first topological invariant. When the system dimension is increased to 3, more than one integer number is needed to describe the topology. For instance, in the three-dimensional case, the topology is described by a set of 4 integer numbers instead of one. [47].

3.1.2 Quantum Spin Hall Insulators

The intriguing dissipationless transport mechanism exhibited by conductive edge states in QH systems motivated several studies, aimed to realize novel devices in view of novel advanced technologies. The first practical limit to engineer this class of materials, was represented by the low temperature and the high external field requirement. In the perspective of overcoming these limitations, a new class of materials known as Quantum Spin Hall Insulators (QSHI) has been realized [48].

QSHI are bulk insulators which present a strong atomic spin orbit coupling (SOC) that sim-

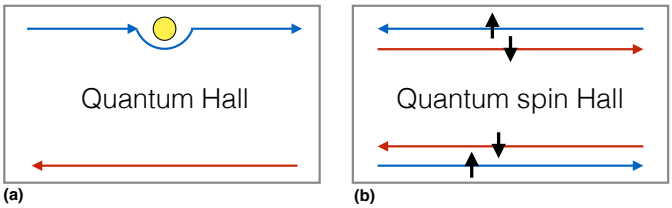

Figure 3.1: (a) A QH bar with both forward and backward carriers divided in the upper and lower edge, since the states are robust, carriers go around an impurity without scattering. (b) A QSH system shows 4 spatially separated and spin polarized channels.

ulates the effect of an external magnetic field. These materials supports, as QH systems, metallic states at the perimeter. Conversely from QH states, the TR symmetry in conserved, due to the absence of an eternal magnetic field. Figure 3.1 panel (b) shows a schematization of the QSH state.

Along the upper and lower edges spin-polarized electron currents flow, showing a well defined spin helicity. A net transport of spin is realized, since two states with opposite spin counterpropagate at a given edge of the material [4, 49]. Being the edge states spin polarize, they are robust and the backscattering by non magnetic impurities is forbidden. The number of forward/backward carriers it is not arbitrary, but must be odd (as represented in fig.3.1). The even-odd parity of carriers number is related the so-called Z_2 topological quantum number [50], an important quantity which belongs to the class of the topological invariants and will be treated in details in the next part.

The experimental realization of the QSH effect was achieved by Bernevig and Hughes [51]. In their work, in 2006, they have successfully proved that a HgTe/CdTe quantum wells system is a QSH insulator by observing a quantized resistance due to perfectly conducting edge states. They have recorded, in particular, that the behaviour of a HgTe/CdTe quantum well system depends on the thickness d of the HgTe layer. Quantum wells thinner than a critical thickness (d_c) are characterized by the fact the electron and hole bands are inverted. The strong spin-orbit interaction drives an energy ordering inversion of HgTe orbitals. As a consequence of the inversion of the parity ordering, at the boundary between the inverted HgTe and trivial CdTe well, metallic edge states appear dispersing within the band gap. This experiment is of pivotal importance because it represents the first experimental realization of the band-parity inversion. This mechanism, is at the base of the topological phase formation.

3.1.3 Three Dimensional Topological Insulators: The Topological Invariants

Topological Insulators can be thought as the 3D extension of the QSH insulators which, for this reason, has been recently renamed as 2D TI. The necessity for strong atomic SOC both QSH insulators and TIs requires the compounds to be formed by heavy elements, with a large Z number. Soon after the QSH states discovery, Fu and Kane have formulated a set of general criteria to distinguish topologically ordered material from topologically-trivial ones [52].

The theoretical approach formulated is based on the bulk band parity inversion which can be expressed in the form of topological invariants. Their model provides a straight and simple (in the case of centrosymmetric materials) way to predict new TIs. Hence, it has a tremendous impact on the experimental development of the field.

In this section we examine the effect of SOC on the energy levels of the prototype TI $\mathrm{Bi_2Se_3}$ of a TI, before the concept of topological protection is analized. Finally, we detail the topological invariants, necessary to formally classify and distinguish different topological phases of matter. For the sake of simplicity we analize the case of $\mathrm{Bi_2Se_3}$, but the conclusions we draw are general for all the TIs.

We consider at the beginning the case of a common topologically trivial semiconductor with a small energy gap. The conduction and valence bands show well defined parities,[2] specifically p-character (negative parity) into the valence band (VB) and a s-character (positive parity) into the conduction band (CB). In the presence of strong SOC, the level degeneracy can be broken and the original ordering can be inverted, breaking the levels degeneracy. P-levels split into two states ($j = 1/2$ and $j = 3/2$) and the latter above the s-level. Figure 3.2 shows the energy ordering inversion for the case of $\mathrm{Bi_2Se_3}$ TI.

In analogy to the QSHI case, topological surface states appears within the energy gap, when the material with inverted band ordering (the TI) is interfaced with a normal (topologically trivial) insulator materials, or for example, the vacuum. The surface state, which presents a typical linear dispersion, is known as Dirac cone. It is worth noticing that the existence of the metallic surface states is a consequence of the electronic properties of the bulk and the states are topologically protected against small perturbations of the hamiltonians. Only modifications capable to induce the closure of the gap can affect the surface state dispersion. In order to discuss the stability of surface states we provide in the following a more rigorous formulation.

[2] The parity is due to the symmetry properties of Block wavefunctions.

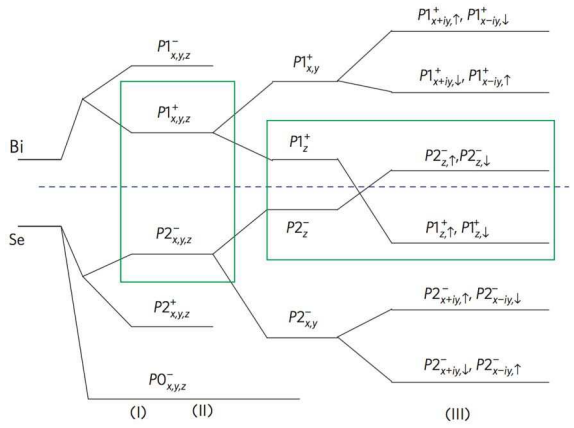

Figure 3.2: Diagram of levels of p_x, p_y, p_z atomic orbitals of CB and VB of Bi_2Se_3 TI at the Γ point. The three different stages represent the effect of turning on: chemical bonding (I), crystal-field splitting (II) and SOC (III). The blue dashed line represents the Fermi energy. [53]

The Kramers theorem predicts the spin degeneracy in solids when TR and spatial inversion symmetries are satisfied. At the surface of the sample the inversion symmetry in broken because of the asymmetry of the potential in a direction orthogonal to the plane, i.e. interruption of the translational symmetry. As described by the Rahsba-Bychkov model [54], the breaking of the symmetry in combination with the SOC lifts the spin degeneracy in almost the entire Brillouin Zone. Nevertheless, at a finite number of points of the reciprocal space, the TR symmetry alone is sufficient to guarantee the spin degeneracy. These points are called Time-Reversal Invariant Momenta Γ_i (TRIM), defined by:

$$-\Gamma_i = \Gamma_i + \mathbf{G} \tag{3.1}$$

where $\mathbf{G}$ is a bulk reciprocal lattice vector. In analogy, also surface TRIMs are defined can be defined according to the relation:

$$-\Lambda_a = \Lambda_a + \mathbf{g} \tag{3.2}$$

with $\mathbf{g}$ a surface reciprocal lattice vector.

Let us consider, for example, an insulator with a hexagonal Brillouin zone and the projection of the bulk bands along the high symmetry direction connecting the two surface TRIMs, $\Gamma - M$. This projection is represented by the grey areas in fig. 3.3. In panels (b-c) Rashba- Bychkov split

free electron-like surface states are represented, while in panels (d-e) topologically protected surface states are shown. If we modify the chemical potential, by small modification of the hamiltonian, states can be lifted above the E_F, as illustrated in fig. 3.3 panel (c). Thus, starting from a metallic system we get a semiconductor.

If we try to modify the dispersion of the topological protected states, as shown in panels (d-e), the scenario is radically different. By varying the position of the chemical potential, we can in principle push or pull the crossing-point of the two spin branches above or below the E_F. However, no energy gap is open, and the metallicity is conserved. As a matter of fact, the gap opening would violate TR symmetry that guarantees spin-degeneracy at $\bar{\Gamma}$.

We notice that the band dispersion of the electronic states represented in both panels (b) and (d) of fig. 3.3 shows some similarities. The most striking difference between the two is the number of E_F crossing between the two opposite surface TRIM points, $\bar{\Gamma}$ and $\bar{M}$. If the E_F is intersected an even number of time the material is topologically trivial, and the hamiltonian can be modified in order to reduce the number of crossing to zero. Otherwise, the number is odd the material is a 3D TI and the metallicity is protected.

To formally classify QH, QSH and TIs according to their topology, we introduce a set of topological invariants. As previously explained, a 2D QH is fully identified by the integer TKNN number [46], while a 2D QSH by the Z_2. The Z_2 is a relative base-2 number which can assume only two values, namely 0,1 or 1,-1. Three dimensional TIs requires instead 4 distinct Z_2 numbers. Three of them, (ν_1, ν_2, ν_3), are related to the translational symmetry of the lattice and characterize the so-called *weak* topological insulator phase. The fourth invariant, ν_0, is the most important since it accounts for the robustness in the presence of disorder, and characterizes the *strong* topological insulator phase. This integer number is evaluated by introducing the so-called parity invariants $\delta(\Gamma_i)$, which can be calculated for each of the eight bulk TRIM trough the expression [55]:

$$\delta(\Gamma_i) = \prod_n \xi_{2n}(\Gamma_i) \tag{3.3}$$

where the $\xi_{2n}(\Gamma_i)$ are the parity eigenvalues of the occupied band at Γ_i, obtained from band structure calculations. The integer ν_0 can be finally calculated by the product of the single parity

invariants $\delta(\Gamma_i)$ by:

$$(-1)^{\nu_0} = \prod_n \delta(\Gamma_i) \tag{3.4}$$

A material is a topological insulator when the product gives -1, while is a trivial insulators when the result is 1. Indeed, is a topological insulator for $\nu_0 = 1, (0)$ [3] and a trivial insulator when $\nu_0 = -1$. It is worth mentioning the case of weak topological insulators, since they can be consider as an exception for this classification.

Weak TIs present a strong topological invariant ν_0 which is equal to 0, while the three numbers (ν_1, ν_2, ν_3) distinguish them from trivial insulators. They have attracted the interest of the scientific community because, from an experimental point of view, the determination of the weak topological phase with respect to the strong one requires a significant effort. We cite the study performed by [57], who have predicted the first weak TIs candidates in the family of even-layered semiconductors compounds, which can host quantum spin Hall layers.

By projecting the parity invariants onto the surface TRIMs, a second important topological number derives, the surface fermion parity $\pi(\Lambda_a)$:

$$\pi(\Lambda_a) = (-1)^n \delta(\Gamma_i)\delta(\Gamma_j) \tag{3.5}$$

Where Γ_i and Γ_j are the bulk TRIMs projected on the surface high symmetry points Λ_a. The product between two surface fermion parity numbers $\pi(\Lambda_a)$ and $\pi(\Lambda_b)$ defines the parity number of E_F crossing when moving along the $\Lambda_a\Lambda_b$ direction. The product is equal to $+1$ in the case of a trivial insulators, indicating a even number of crossing. Whereas, in TIs this product assumes -1 value, thus an odd number of gapless surface states is guaranteed.

Figure 3.4 illustrates such a difference between trivial an topological insulators. We consider two surface TRIMS (Λ_a, Λ_b), where spin split states respect the Kramer spin degeneracy. In the case of a TI (a), when moving between two TRIMs the couple of states is modified. In the latter case (b), the couple of states is conserved. This effect is called the band parter switching, and originates from the change in surface fermion parity.

[3] In the case of Bi_2Se_3 TI, bulk parity invariants calculated for Z, L and F TRIMs are 1 while for the bulk Γ point is -1. The product of is thus found to be -1, hence $\nu_0 = 1$ [56].

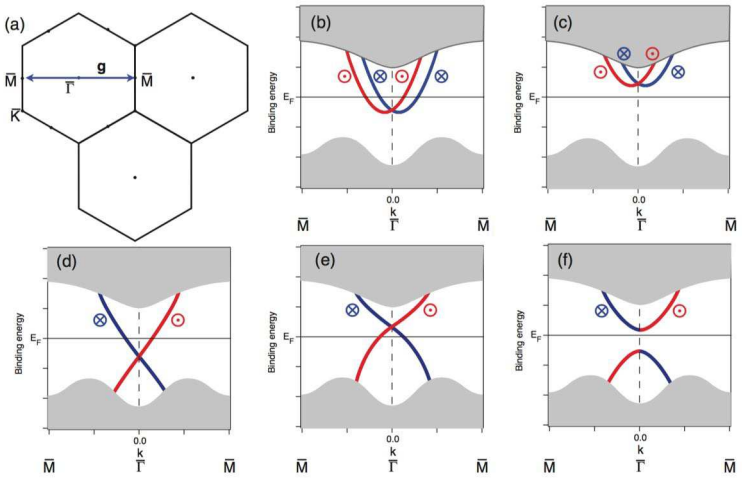

Figure 3.3: (a) Hexagonal surface Brillouin zone with high-symmetry points. The $\bar{M}$ is as a time-reversal invariant momentum. (b,c) Rashba-split free electron-like surface state in a projected bulk band gap. The dispersion of metallics state in (b) is lifted above the E_F in (c). In Panels (d,e) show a topologically protected spin-split surface state. Time reversal symmetry avoid a band gap opening, so the situation in (f) cannot be realized. [58]

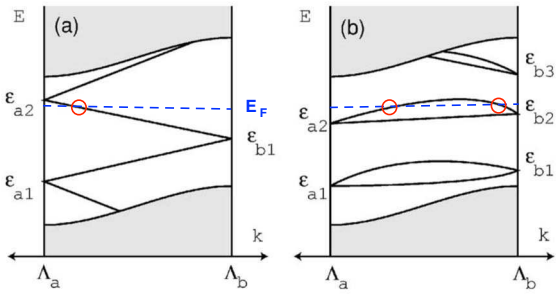

Figure 3.4: Sketch showing two possible way to connect different TRIMs with Kramer-degenerate spin split surface states. The E_F is indicated by the blu dotted line and the crossing point with red circles. In the case (a) the couple changes by moving between two TRIMs, odd number of Fermi crossing, TI. In the case (b) the couple is conserved, even number of crossing points, trivial insulator. Adapted from [50].

3.1.4 The New Generation of 3D TIs

The capital work of Fu and Kane has triggered the search for new topological compounds. Three-dimensional TIs constituted the ideal system for angle resolved photoelectron spectroscopy (ARPES), becouse this technique is capable to reveal the materials electronic and spin structure. Because of the ARPES surface sensitivity and its capability to access the band dispersion, also with spin polarization, ARPES has probed to be the ideal tool to investigate TI systems.

In 2007, the first 3D TI candidate was proposed, the bismuth antimony alloy $Bi_{1-x}Sb_x$ [5]. Pure bismuth is a semimetal, and it has large atomic number Z and it displays strong SOC. Band structure calculations along the T-L-H high symmetry directions have revealed that, at the $\bar{\Gamma}$ point, the top of the VB lies at energy higher than the bottom of the CB.

An hole- and electron-pocket are present at the T and L point respectively [59]. The progressive substitution of the bismuth with the antimony has leaded to drastically changing the band structure. At a certain concentration of Sb ($x \simeq 0.04$), the energy gap at the L point closes and reopens with an inverted ordering. Thus, starting from a trivial semimetallic state a topological phase is reached. The evaluation of the fourth Z_2 invariants ν_n confirmed the TI character of this compound. The product of the parity invariants $\delta(\Gamma_i)$ at Γ, T, L and X TRIMs points is 1.

Finally we note that also the pure Sb presents a ν_0 value equal to 1, but this compound has no bulk band gap, hence it represents one of the first example of topological semimetals. Soon after, an ARPES experiment have been carried out on the $Bi_{0.9}Sb_{0.1}$ by [60], in order to verify if this compound has inherited the topological character from $Sb(111)$ [61]. ARPES measurements have experimentally confirm the TI nature of this alloy. In addition, a spin-ARPES investigation has revealed the predicted spin-polarization of surface states. However, this material has showed to strongly depend on Sb concentration and has revealed a quite complex band structure in proximity of the E_F.

In order to exceed these limitations, the research of new TIs has started, with the requirements which follows. Stoichiometric compounds are required, in order to be grown, highly homogeneous over relatively large size. The number of surface states should be lower, in order to ease theoretical calculation and the experimental observation, while a large energy bulk gap is favoured, in order to host highly dispersing surface state. Ab-initio theoretical calculations have proposed the layered stoichiometric crystal $\mathrm{Bi_2Se_3}$, $\mathrm{Bi_2Te_3}$ and $\mathrm{Sb_2Te_3}$ as TIs compounds.

These materials, which fulfil all these requirements, share the same rhombohedral crystal

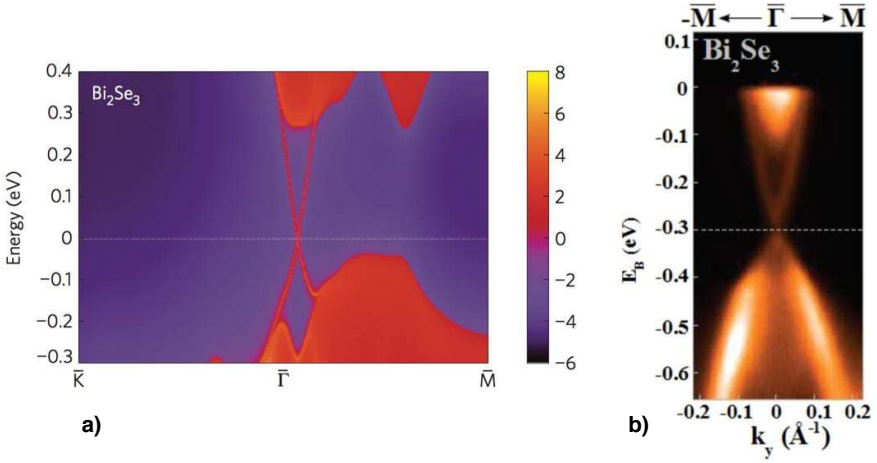

Figure 3.5: a) Bi_2Se_3 LDOS on the [111] surface, adapted from [53]. (b) The measured band structure along $\Gamma - M$ [63].

structure with the space group D^5_{3d} $(R\bar{3}m)$ and five atoms per unit cell [53]. Among the three, the bismuth based compounds, Bi_2X_3- X = Te,Se are certainly the most studied. Their crystal structure consist of quintuple-layers (QLs) blocks, arranged orthogonally to the z-axis. Each QL results from two planes of Bi sandwiched between three layers of X = T e, Se. While different QLs are bounded together by weak van der Waals interaction, the atomic layers within QL are strongly coupled by covalent bonding.

The archetypal strong TI is identified in Bi_2Se_3, since it exhibits the largest band gap (0,3 eV). Figure 3.5 (a) and (b) show the calculated Local Density of States (LDOS) projected on the (111) surface in panel (a), and the corresponding measured band dispersion (b) [53]. A single Dirac cone at the Γ point is present, connecting the top VB with the bottom CB. For case of Bi_2Se_3 the bottom of the CB is populated, as shown in panel (b) of fig. 3.5.

In general, naturally grown Bi_2X_3 compounds present a large electron-doping, for instance n-type resulting from Bi vacancies and Te(Se)/Bi antisites. Chen et al. have investigated hole doping effects on the band structure of TIs, by measuring $(Bi_{1-\delta}Sn_\delta)_2\,Te_3$ with different Sn concentrations (δ) [62]. Figure 3.6 shows the evolution of the of Fermi surface (FS) and the Fermi level (E_F) position for increasing values of δ.

In the native sample, panel (a), the E_F crosses both CB and SS, which are indicated in the FS in fig. 3.6 with SSB and CBC respectively. When the E_F crosses only the surface state,

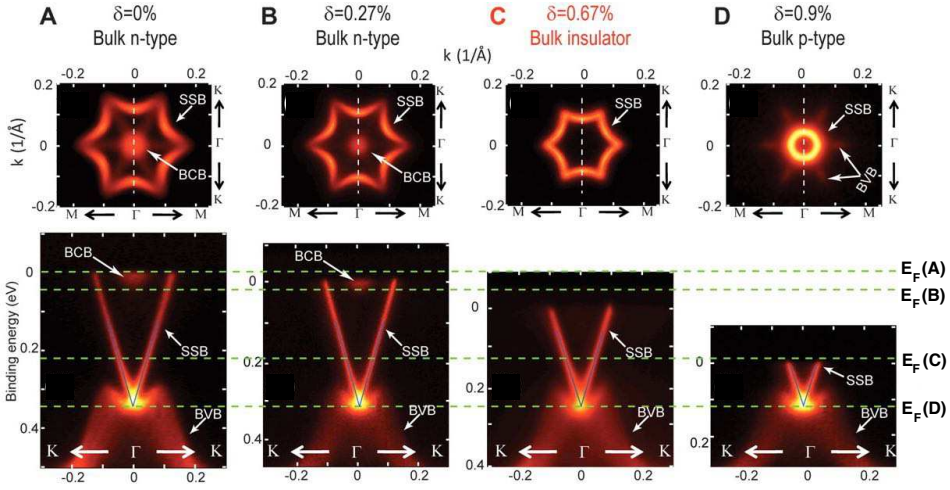

Figure 3.6: (A-D) Top raw: measured FSs for 0, 0.27, 0.9 % nominally doped compounds. Adapted from [62] Bottom raw: Measured band structure along $\Gamma - K$. BCB, SS, BVB are indicated. Greed dotted lines indicate the E_F for the four cases.

as shown in panel c, the TI is said to be intrinsic. The third and the last possible doping is represented by the hole p-type. This is shown in fig. 3.6 panel (d) with the top of the bulk VB visible at the E_F.

3.2 State-of-the-Art: Previous Tr-ARPES Investigations on TIs

The peculiar spin polarization exhibited by topological surface states has inspired several studies aimed at realizing spin-current based devices. Interestingly, the possibility of optically inducing spin-polarized currents by using ultrafast circular polarized photons has been shown [9]. An essential parameter for photoconductivity in TIs is the balance between excess electrons and holes in the Dirac cone. This balance can be optically controlled by varying the interplay of surface and bulk transient carrier dynamics. As a result, charge carriers can be directly photo-inject into TSSs. [32].

In the perspective of investigating the response of Dirac particles to ultrafast photoexcitations, a pump-probe approach is needed. Tr-ARPES has revealed to be the most powerful tool to study the non- equilibrium dynamics of TI materials. As matter of fact, several Tr-ARPES studies have been performed in this direction, and most relevant are collected in the next sections.

3.2.1 Pioneer Results on Bi_2Se_3 and Bi_2Te_3 TIs

First time-resolved experiments performed on $\mathrm{Bi_2Se_3}$ and $\mathrm{Bi_2Te_3}$ by Sobota and Hojlaui have pioneered the investigation of ultrafast optically excited carriers dynamics in TIs [10, 32].

The first work has developed a simple model to describe the excitation and relaxation of the transient electronic population in surface and bulk states. The second study, in order to describe the relaxation of the system, has proposed a more quantitative system of rate equations. The authors have performed tr ARPES measurement of slightly p-doped (Mg doped) $\mathrm{Bi_2Se_3}$ single crystal [10]. They have exploited the first harmonics (1.5 eV) of a high-repetition rate amplifier to excite the system (pump) and the fourth harmonics of the laser (6 eV) as probe.

Figure 3.7 shows snapshots of the measured band structure at the different delay time between the pump and the probe. The E_F, is crossed by the valence band, according to the material p-doping. The first panel (a) of fig. 3.7, shows a delay time before the arrival of the pump. The peak of photoemission intensity in located at the top of the VB, whereas the CB lies in the unoccupied density of states (DOS). After optical excitation (panel c and d) the Dirac cone and the bottom of CB are populated, reaching the maximum occupation within about 0.7 ps after the arrival of the pump pulse. In the second panel, (b), a schematic of the band structure is reported.

By comparing the different delay it is evident that TSS are not directly populated. The

entire process can be decomposed in different steps, which are schematized in fig. 3.8 (a-d). A direct inter-band optical transition first excites electrons from the VB to the high energy branch of the CB, panel (a). Successively, electrons scatter towards the E_F, on a fast time scale ($<$ 1ps), while a long-live electron population is observed at the bottom of the CB, panel (b). The bottom of the lower branch and the Dirac cone are simultaneously filled in a finite time, via intra-band scattering (c). Electrons at the edge of the bulk CB form a metastable population and also SS carriers persist [10]. Because the energy gap (200 meV) is larger than the higher phonon energy (23 meV), electrons and holes can not recombine through electron-phonon scattering. The authors propose that the mechanism of cascade relaxation and bottleneck at the gap result in a surprising slow relaxation of the carriers along surface states. The persistent non equilibrium population of the Dirac SS is associated, by the authors, to a cascade mechanism. This effect is possible due to the presence of the CB, which acts as a carriers reservoir. This cascade process is visible in the data of figure 3.8 panel (f). This reports the measured photoemission intensity curves. These data have been extracted by small energy-momentum integration regions along the Dirac cone.

Finally the electronic temperature (Te) has been extracted, by selectively fitting the EDCs related to VB and CB. The temporal evolution of the electronic population in the VB and CB, because of the bottleneck effect, are described by two different Fermi Dirac distributions. By analyzing the temporal evolution of the FD distributions, authors claim that they can infer about the electronic temperature T_e. Finally, from the fitting to the temporal evolution of Te, the authors estimate the decay time constants τ_{e-ph} for the intra-band cooling, which is $\simeq 1.74$ ps.
Hojlaui et al, have performed a tr-ARPES study of the transient electronic population in surface and bulk states of a slightly n-doped Bi_2Te_3 TI by means of a pump-probe approach [32]. They have confirmed, for this different doping and different compound, that a long lasting signal is observed in the TSS after optical excitation. Moreover, they have reported a peculiar dependence between the relaxation time of the electronic population and the position in the electronic band structure where the population is evaluated. This is shown in figure 3.9 (c), where the dynamics of the photoemission intensity is reported for four different regions of the band structure, both above and below E_F as schematized in fig. 3.9 (a) and (b).

Figure 3.9 (a) shows the band structure before the optical excitation. Panel (b) is a sketch of the surface and bulk bands. Two regions, labelled B_1^* and B_2^* correspond to the upper and

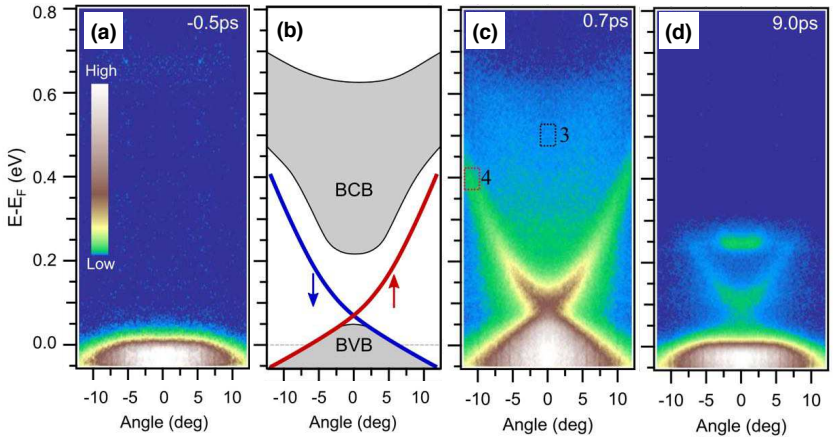

Figure 3.7: The transient photoemission intensity before the photo-excitation in panel (a), after 0,7 ps and 9 ps in panel (c-d) respectively. A sketch of band structure of measured Bi_2Se_3 showing spin-polarized SSs in panel (b). Adapted from [10].

lower branches of the CB. The Dirac cone is divided in two regions, S^* and S, one above and one below the E_F, respectively. The corresponding temporal evolution of the four populations (B_1^*, B_2^*, S^* and S) after the pump excitation are reported in figure 3.9 panel (d).

While the transient population of the CB, at larger energies, relaxes in few ps, the SS shows a longer dynamics with a persistent intensity in proximity of E_F. The bottom of the CB, (B_2), was found to exhibit a slow dynamics too. Hence, the CB was proposed to play a role of reservoir which fills the Dirac cone below. In order to mimic properly the temporal evolution of intensity, they have developed a complex rate equation system describing the microscopic scattering between the parts of the band structure. The fit functions which are represented as continuos line in figure 3.9 panel (c), has been derived from the model. Each scattering process contributes to the total dynamics. The electrons, which have been directly transferred by the pump pulse in the unoccupied B1*, decay in B_2^* and S^* in 0.34 ps. Successively, these two states show similar decay times, 1.8 ps for B_2^* and 2.1 ps for S^*. Finally, according to the system or rate equation, the S empty states are filled showing two different characteristic times, 0.14 ps and 5.7 ps.

There is a remarkably good agreement between the experimental results and the model. Nonetheless, we note also the limits of the proposed model. B_2 and S^* present a parallel evolution, but in the rate equation no scattering term has been taken in account. Besides, there

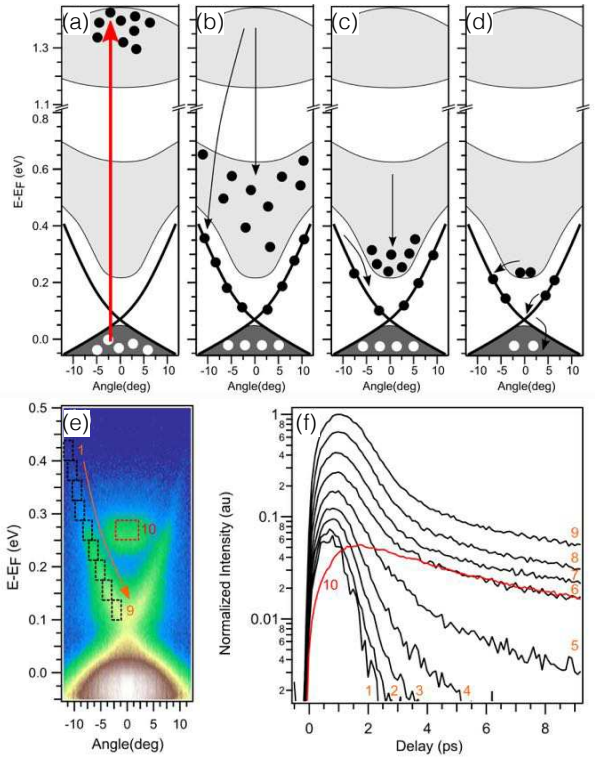

Figure 3.8: Different excitation and relaxation processes illustrated by a sketch, panels (a-d). Energy-momentum integration regions along the Dirac cone (e) and corresponding time-dependent photoemission intensity curves (f). Adapted from [10].

is no term accounting for the different energy position of the electrons in each band. In both these Tr-ARPES investigations, the long lasting population observed after optical excitation in the surface state has been ascribed to the cascade mechanism from the CB, acting as a charge reservoir. In conclusions, in these two studies, the authors have proposed that the slow relaxation of surface hot electrons might manifest a general property of TIs.

The rapidly growing research on optically excited TIs was further boosted by the work of Y. H. Wang et al., reporting a further Tr-ARPES study of the prototypical Bi_2Se_3 TI [11]. The authors have compared the electron dynamics at two different lattice temperatures, 15 K and 300 K. Being the first below the Debye temperature of the material, found to be approximately 182 K, the latter temperature is above. These authors have been able to extract the relaxation dynamics of the electronic temperature and the chemical potential relaxation dynamics related to the TSS surface states and bulk bands separately.

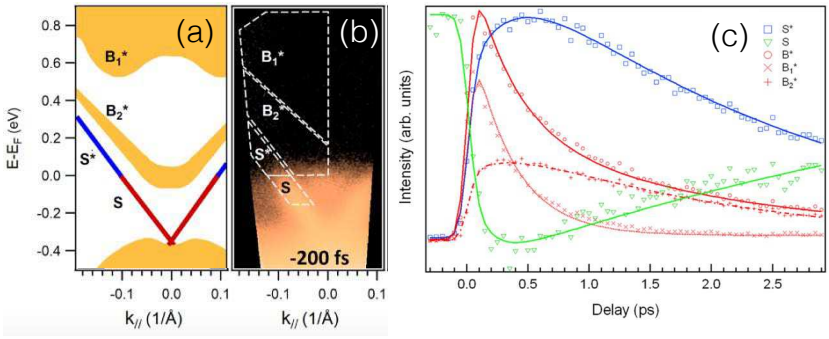

Figure 3.9: (a) Schematic illustration of the Bi_2Te_3 band structure measured along the $\Gamma - K$ high symmetry direction, reported in (b). The time-dependent photoemission intensity extracted from the four integration regions B_1^*,B_2^*,S^* and S are shown in (c) with different marks. The fits (continuos lines) functions derived from a system of rate equation [32].

The results have revealed that, depending on the lattice temperature, that different scattering channels are at play. Figure 3.10 shows the surface and bulk electronic temperature, labelled by T_e^{SS} and T_e^{CB} respectively. In the high temperature case, T_e^{SS} and T_e^{CB} equilibrate within the investigated temporal window. Electron can scatter between the bulk and surface states via electron-phonon scattering leading to the thermalization of the two electronic systems.

In the low temperature case instead this phonon mediated scattering is suppressed, being the phononic mode frozen below the Debye temperature. As a consequence, electrons in CB and TSS do not thermalize within the temporal window investigated in the experiment. Wang et al. ascribe this different behaviour to the presence of two different scattering processes. They suggest that the lack of thermalization at 15 K is due to an inelastic e-e scattering between SS and CB with a time scale which exceeding the measured time window. Hence, the authors suggest the suppression of interband inelastic e-e scattering is due to kinematics constraints.

Other Dirac materials, as graphene, have show that different mechanisms, based on carrier density dependence, can be distinguished [64]. In order to selectively study the intraband cooling dynamics, Y.H.Wang et al. have measured the Bi_2Se_3 TI over a wide range of doping, and consequently with different energy position of the Dirac point. Figure 3.11 shows the dependence of the electronic temperature dynamics of surface (a) and bulk (b) states for different charge carriers concentration. The surface temperature relaxes in general with two decay components, τ_1^{SS} and τ_2^{SS}. They suggest that below 600 K the optical phonon cooling became less effective,

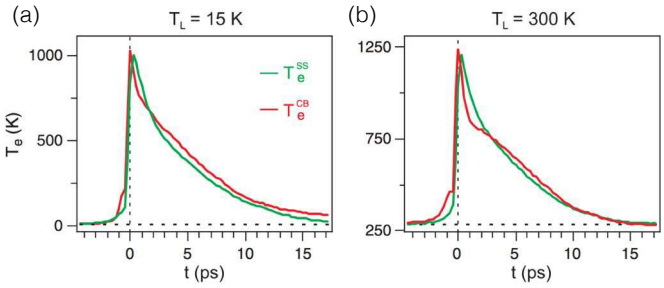

Figure 3.10: Inter band surface and bulk electron dynamics measured at two different lattice temperatures. (a) Electronic temperature T_e for SS (green) and CB (red) at lattice temperature $T_L = 15K$ and (b) $T_L = 300K$ respectively. Taken from [11].

and the decay is dominated by the second component τ_2.

This second decay time shows a clear dependence on the position of the Dirac point (E_D) and thus on doping. The bulk dynamics, on the contrary, shows a fast component which matches with previous investigations and a second slow component which exhibits no discernible dependence on E_D. The different dependence in bulk and surface states on the doping is also evident in the inset of fig. 3.11 panel (b). This inset reports the rate $1/\tau_2$ as a function of $\mathrm{E_D}$. In the surface case, a power low dependence is shown, whereas in the bulk case no evident dependences are detectable . These interesting results suggest that varying the electron-hole concentration in TI systems, we can observe remarkable consequences on the surface and bulk relaxation dynamics.

The interpretation of the long relaxation dynamics observed in the TSS in terms of a cascade process from the charge reservoir in CB was partially questioned by a Crepaldi et al.[12]. Similarly to the previous study, these authors have found that after the optical excitation, surface state electrons are thermalized at all delay times. In agreement with Wang et al, a variation in the effective chemical potential ($\Delta\mu \simeq 10meV$) has been observed and interpreted as the result of the ultrafast photo doping of the conduction band. The dynamics of effective electronic temperature and of the chemical potential have been analized. In particular ref. [12] show characteristic relaxation times τ_T and τ_μ of 2.5 ps and 2.7 ps, respectively. The τ_T value is smaller than the one reported for p-type $\mathrm{Bi_2Se_3}$ (1.67 ps [10]). The authors ascribe this discrepancy to different pump fluences in the different experiments.

In agreement with the work of Hajolouji et al., the dynamics of the electron population

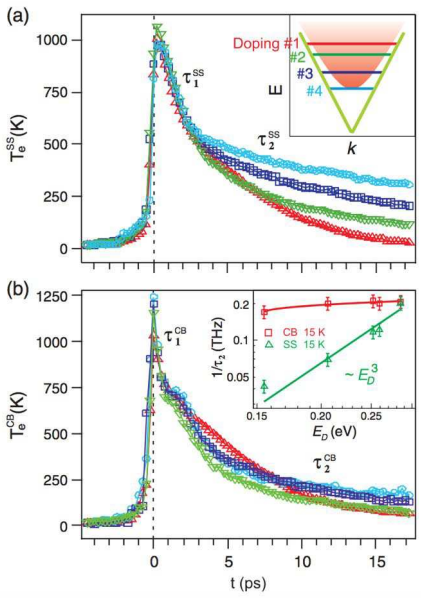

Figure 3.11: Temporal dependent electronic temperature of surface (a),and bulk states (b) at $T_L = 15K$. Different colors corresponds to different Dirac point position shown in the inset of panel (b). Inverse cooling time of the slow component$1/\tau_2$ of T_e as a function of E_D at 15 K for SS (green triangles) and CB (red squares). Taken from [11].

shows a peculiar dependence with the energy position along the dispersion of the TSS. However, in contrast to the previous investigations have proposed the creation of a long-lived population in the CB to be responsible for the slow relaxation time, here a different interpretation is suggested. The population dynamics in different positions of the band structure have been analyzed quantitatively and a minimal model is proposed to describe the dependence of $I(E, k, t)$.

This model is based on the idea that the characteristic relaxation times of $\mathrm{T_{el}}$ (τ_T) and if $\mu(\mathrm{t})$ (τ_T) are insensitive on the k and energy position and they alone dictate the relaxation times of the electronic population in different region of the band structure. In fact, the different temporal evolutions of I(k,E,t) is mediated by the Fermi Dirac distribution and shows a non liner dependence with $\mathrm{T_{el}}$ and $\mathrm{mu(t)}$. This phenomenology has been analytically treated in Reference [65] where it has been shown that the relaxation time of I(k,E,t), in different region of the band structure can be express as:

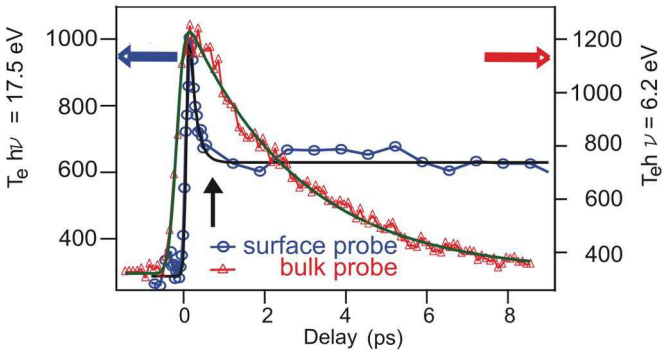

Figure 3.12: Electronic temperature: blue (red) markers refer to 17.5-eV (6.2-eV) probe energy. The black solid line shows the best fit obtained with a single decay exponential plus a constant. [66].

$$\tau(E) \simeq \frac{1 + e^{-\frac{E-\mu_0}{k_\beta T(0)}}}{\frac{\Delta T}{\tau_T}\frac{E-\mu_0}{k_\beta T(0)^2} + \frac{\Delta\mu}{\tau_\mu}\frac{1}{k_\beta T(0)}} \tag{3.6}$$

3.2.2 Surface and Bulk electron-phonon scattering processes

All of the aforementioned time-resolved ARPES experiments have been carried out exploiting high repetition rate laser-based sources at 6.2 eV photon energy. Due to the very low kinetic energy of the photoelectrons, those experiments can be considered relatively more bulk sensitive than conventional ARPES experiment in the VUV energy range. For Bi_2Se_3 the estimated photoelectron escape depth at this photon energy is $\sim 2-3$ nm, i.e. between 3 and 4 quintuple layers. For instance, at 17.5 eV the escape depth is less than 1 QL ($\sim$ 1) nm. Whereas, at a higher photon energies, the mean free path is reduces.

Crepaldi ed al., have investigated the possibility of different relaxation mechanisms at the surface or in the bulk of n-doped Bi_2Se_3 [66]. The authors have compare tr-ARPES results for different probe photon energies, namely 6.2 eV and 17.5 eV (extreme UV, EUV). By exploiting these probe energies, they have proposed to be able to record the out-of-equilibrium dynamics of the CB for the surface and the bulk. In particular, by following similar analysis to these discussed in the previous sections, these authors have extracted the evolution of the electronic temperature and the chemical potential.

Figure 3.12 shows the $T_{el}(t)$ obtained by measuring with 17.5 eV and 6.2 eV probe energy,

corresponding to shorter and longer mean free path. Blue and red markers indicate, respectively, the results obtained by the surface- and bulk- sensitive probes. Interestingly, two different relaxation dynamics for the electronic temperature in the CB have been revealed. In the bulk, the relaxation of T_e is fitted with a single exponential decay with τ_T =2.7 ps, in agreement with the characteristic values discussed in the literature. For this reason, the characteristic relaxation time τ_T, has been considered as a measure of the strength of the electron-phonon scattering in the material.

The second dynamics observed in T_e and reported in fig. 3.12, is quite different. An ultrafast decrease with $\tau_T \sim 160$ fs is followed by the formation of a steady state with $T_0 \sim 640$ K, as extracted by the best fit to the curve. This "hot" state lasts several ps. Hence, the temperature does not relax back to its equilibrium value, but exhibits a clear plateau for we exclude artefacts due to pump-induced space-charge effects since not depends on the pump fluence. The authors have interpreted this long-lasting out-of-equilibrium state in the CB as a manifestation of a reduced efficiency of the phonon scattering at the surface. In addition, they have noticed that the temperature characterizing the plateau, (640 K) is comparable to the temperature (600 K) where the cooling by optical phonons is expected to be less effective for a Dirac particle [11].
They ascribe the possibility of a reduced electron-phonon scattering at the surface to the observation of a weak electron-phonon coupling ($\lambda = 0.08$).

3.2.3 First Evidences of Correlation Between the Electron Dynamics and Doping

The pioneering work of Wang et al. has proved the dependence between the electron dynamics and the material doping, i.e. the position of the Fermi level with the band structure. The first systematic investigation of several different doped bismuth chalcogenide with different doping TIs is due to M.Hajlaoui et at.[15]. In particular, they have measured p-doped and n-doped compounds, revealing different temporal dynamics. Figure 3.13 reports ARPES images of a p-type $Bi_{2.2}Te_3$ (a) and of a n-type Bi_2TeSe (b) before and after the optical excitation.

The time-dependent photoemission spectra are reported in panel (c), as extracted from the indicated regions, CB and S. By comparing spectra acquired at the same temperature (40 K) it emerges that the time-evolution of the population in the n-doped case is almost completely relaxed after 8 ps. On the contrary the p-type shows a long lasting decay, which relaxes on a

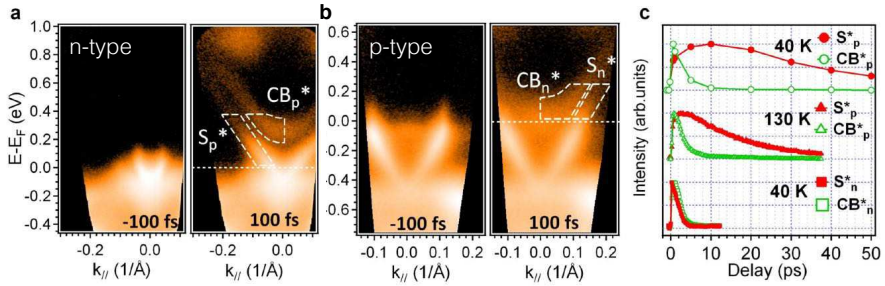

Figure 3.13: Time-resolved ARPES measurement of p-doped $Bi_{2.2}Te_3$ (a) and n-doped Bi_2TeSe selected before and after the arrival of the pump excitation. (c) Time evolution of the photoemission intensity corresponding to the integration regions indicated on surface and bulk states, acquired at 40 K and 130 K. Adapted from [15].

time scale of $\sim$ 50 ps.

Authors claim that it has already been observed that surface states have a longer relaxation time when they are within the gap, because they do not have access to the faster bulk recombination channels. Furthermore, the reservoir effect, previously attributed to the CB, it is not at play in the relaxation process they have shown. They completely ascribe the different temporal dynamics to a surface band bending and to a transient charge asymmetry.

The p- and n-type samples shown in figure 3.13 present a downward ($\sim$ 60 meV) and upward ($\sim$ 30 meV) surface band bending respectively. This can strongly affect the bulk-surface interplay and consequently the Dirac cone relaxation, by spatially separating the excess of electrons and holes [15]. The n-doped compound presents an excess of holes, because the bands are slightly bent upward, while the p-doped presents a more pronounced charge asymmetry. This charge disequilibrium at the surface is indicated as the cause of the long relaxation time for $Bi_{2.2}Te_3$, since excess electrons can not find holes to recombine with.

The absence of holes excess in the subsurface VB, that can not recombine with Dirac particles, is indeed attributed to a carriers drift into the bulk. Interestingly, they define the thickness of this region by considering the Debye length L_D of the material. Within this spatial region, called space charge layer $(0 \leq z \leq L_D)$, a situation is created where there is a strong excess of electronic population concentrated in the conducting surface states while no excess carrier are present in the bulk bands [15]. The electron-holes distribution is balanced in the case of a flat-bands TI, therefore they consider the electron-phonon scattering to be the intrinsic limiting.

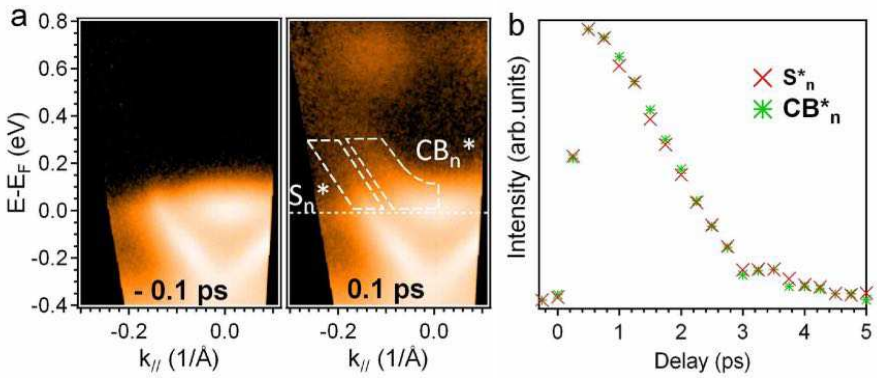

Figure 3.14: Dynamics of n-type Bi_2Te_3 flat-band sample. (a) Snapshots of the Tr-ARPES measurement, before and after the optical excitation (b). Temporal evolution of the electronic population in the Dirac cone and in the CB. Adapted from ref. [15].

In figure 3.14 is reported their measure of the ultrafast dynamics of a n-type Bi_2Te_3, presenting flat bands. The photoemission intensity, reported in panel (b) relaxes in ~ 3 ps, quite faster than the p-type sample. They explain such difference claiming that the electrons are strongly coupled with the CB and hence exploiting fast bulk recombination channels.
We notice that this fast relaxation time is comparable with the one they show for the n-doped Bi_2TeSe. By comparing fig. 3.13 and 3.14 we evince that the E_F crosses both surface states and the bottom of the CB for both cases. Hence, the role of the bulk relaxation channels they refers to, should be commensurate to the band bending effect.

Chapter 4

Bulk Diffusive Relaxation Mechanisms in Optically Excited Topological Insulators

4.1 Prelude: Observation of Long Surface Lifetime of a Intrinsic Topological Insulator

Bulk metallic topological insulators, which are the object of the studies discussed in chapter 4, present both the topological surface state (TSS) and the conduction band (CB) at the Fermi Level. The lifetime for the Dirac surface states after the optical excitation which has been reported for these materials, is in the order of picoseconds [10, 11, 12, 32, 66].

Very recently, a TR-ARPES investigation of a Bi_2Te_2Se (BTS221) TI performed by by M. Neupane et al., has reported a remarkably long lifetime in the order of 4 μs [16]. This material, conversely from the cases previously mentioned, is a true bulk insulator which presents only the TSS at the Fermi level. The authors have noticed that the observed long lasting temporal dynamics was accompanied by a shift a of the chemical potential of the Dirac TSS, as large as $\sim$100 meV. This shift of the chemical potential has been ascribed to a surface photovoltage, induced by the pump pulse [16].

Neupane and coworkers have measured a n-doped $GeBi_2Te_4$ and a p-doped $(Bi_{0.2}Sb_{0.8})_2Te_3$ TIs, in order to evaluate the temporal dynamics in the case of a metallic compound. The life-

time for both surface and bulk bands, is found to be faster then 5 ps, in agreements with values reported by previous studies. This work has revealed remarkable differences between the transient electron dynamics in intrinsic and metallic TI, suggesting that a detailed understanding of microscopic relaxation mechanism is still missing.

4.2 Introduction

Motivated by the pioneering work of Neupane et al., we have investigated by means of TR-ARPES the temporal evolution of the electronic properties of six TIs, characterized by different positions of the Fermi energy, (E_F) in the bulk band structure. We have investigated such a wide set of materials in order to provide a comprehensive picture of the electronic relaxation processes. Depending on the different position of the Fermi level with respect to the Dirac cone and to the conduction and valence band, compounds have been grouped in *n-type*, *intrinsic* and *p-type*[1]. The investigated materials are the following: n-type $GeBi_2Te_4$ and $GeBi_4Te_7$, p-type Sb_2Te_3 and Sb_6Te_3, and the intrinsic Bi_2Te_3 and $GeBi_2Te_4$.

It is worth noticing that in the present chapter, when we consider the sample doping level, we always refer to the surface doping. As a matter of fact, a common phenomenon with semiconductors is that the doping level at the surface can be different from that in the bulk. This discrepancy has motivated several static ARPES works on TIs, which have focused on surface effects as the band bending [67]. The band bending effect could be particular relevant, in particular when the assignment of the doping type is determined by the position of the chemical potential with respect to the energy gap. However, the band bending reported for the TIs we have measured, ranges from 30-60 meV [15] up to 80-100 meV [67]. Hence, since the effect is small with respect to the energy gap, we do not expect that the assignment of the six samples to the three different groups could be compromised.

The ARPES technique, due to its surface sensitivity, can not directly provide informations about the bulk carriers concentrations. In order to quantify the bulk carriers density and to determine quantitatively the bulk doping, transport measurements are needed. However, since no transport measurements are available for the samples object of our investigations, we do not

[1] When the Fermi level crosses both the bottom of the CB and the SS the compound is n-type. When the Fermi level crosses just the SS is considered intrinsic and when the Fermi level intersects the bottom of the VB is p-type.

provide an estimation of the bulk carriers concentration. Nonetheless, our study is aimed at directly relating the surface scattering processes to the actual surface doping. A direct comparison between the electron dynamics and the doping would require to probe the same samples volume. For that reason, we have adopted the same surface sensitive technique, which represents the best choice for such kind investigation.

The results of the present study, reported and discussed in the next sections, can be summarized as follows. When three-dimensional bulk states lie at $\mathrm{E_F}$, a fast relaxation dynamics with characteristic time of few picosecond (ps) is observed. On the contrary, a long lasting excited state is detected only when the two-dimensional surface state crosses $\mathrm{E_F}$. These findings suggest the important role played by electron diffusion in the direction orthogonal to the surface. We show that this electron diffusive mechanism is propelled by the optically induced temperature gradient and can only be accounted for by electrons residing in bulk states. To understand the origin of this different relaxation timescale, we have quantitatively evaluated the temporal evolution of the electronic temperature, $\mathrm{T_e}$, which offers a direct way for monitoring the energy flow, after the optical perturbation, from the electrons towards other degrees of freedom, such as lattice vibrations.

4.3 Experiment

The experiments was carried out at the T- ReX laboratory [68], exploiting the TR-ARPES end station described in the second chapter. The output of the Ti:sapphire regenerative amplifier, a Coherent RegA 9050 centred at 800 nm (1.55 eV) and operating at 250 KHz, was adopted as pump. The pulse was p-polarized and responsible for the sample optical excitation, with a fluence of $\simeq 230\mu J/cm^2$. The probe pulse, obtained from the fourth harmonics of the laser (6.2 eV), was s-polarized. The overall temporal resolution was $\simeq 250$ fs. The final energy and angular resolution was set to $\sim$ 20 meV and $\sim$ 0.2 Å, respectively. The samples have been cleaved in situ at room temperature in UHV $(10^{-10}mbar)$, and the experiments were carried out in a temperatures range of 110 - 120 K. The samples were oriented along the $\overline{\Gamma K}$ high symmetry direction by means of an in situ low energy electron diffraction (LEED).

The investigated compounds were grown by a vertical variant of the Bridgman technique, as discussed in details in [69]. The n-doped $\mathrm{GeBi_4Te_7}$ and the intrinsic $\mathrm{Bi_2Te_3}$ were grown

by Bridgman technique. Finally, in order to further inquire the relation between the electron dynamics and the E_F position, we have synthetized $GeBi_2Te_4$ with two different bulk charge carrier concentrations: n-type and intrinsic as grown by Bridgman and vapour transport method, respectively. We label the two samples $b - GeBi_2Te_4$ and $v - GeBi_2Te_4$ in order to distinguish them according to the growth techniques.

4.4 Results

The most important TR-ARPES results are summarized in Figure 4.1 (a - h), which shows the ARPES images of the band structure measured along the $\overline{\Gamma K}$ high symmetry direction. For $b - GeBi_2Te_4$ (a), $GeBi_4Te_7$ (b), Bi_2Te_3 (c) and $v - GeBi_2Te_4$ (d), the images refer to the data at equilibrium, before the arrival of the optical excitation. In the p-doped Sb_2Te_3 (g), Sb_6Te_3 (h), the SS lies in the unoccupied density of states (DOS). We chose to display the transient electronic population above the E_F, immediately after the arrival of the pump excitation.

In fig. 4.1 (a) and (b) we clearly resolve the spin polarized SS, with the Dirac point located $\simeq 0.37$ eV and $\simeq 0.3$ eV below E_F, and the Fermi wavevector k_F equal to $\pm$ 0.22 Å^{-1} and $\pm$ 0.122 Å^{-1}, respectively. Along with the SS, we observe additional intensity crossing E_F for smaller wavevector. This intensity corresponds to the 3D bulk CB, dispersing with its minimum at $\simeq 0.1$ eV. The Fermi level is crossed by the bulk CB in both $b - GeBi_2Te_4$ and $GeBi_4Te_7$, which are considered n-type. In the case of Bi_2Te_3 and $v - GeBi_2Te_4$, only the SS disperses at E_F. The CB is unoccupied, and the two compounds are intrinsic TIs. The Dirac point is located at $\simeq 0.2$ eV and $\simeq 0.13$ eV with $k_F \simeq \pm$ 0.07 Å^{-1} and $k_F \simeq \pm$0.1 Å^{-1}, respectively.

Figure 1 (e) and (f) show the corresponding differential images obtained for Bi_2Te_3 and $v - GeBi_2Te_4$, as difference between the ARPES images after (+500 fs) and before (-500 fs) optical excitation. Red and blue indicate the increase and decrease of intensity, respectively. The bottom of the conduction band is clearly resolved at the $\overline{\Gamma K}$ high symmetry point, 0.2 eV above E_F for $v - GeBi_2Te_4$ and 0.3 eV above E_F for Bi_2Te_3. These values are larger than the kz dispersion of the CB, which is of the order 100 meV, as shown experimentally for Bi_2Te_3 [70] and theoretically for $v - GeBi_2Te_4$ [71]. For these reasons we can conclude that these two compounds are intrinsic TIs. Finally, for Sb_2Te_3 (g) and Sb_6Te_3 (h) the SS lies in the unoccupied DOS and the Dirac point is located respectively $\simeq 0.2$ eV and $\simeq 0.25$ eV above E_F.

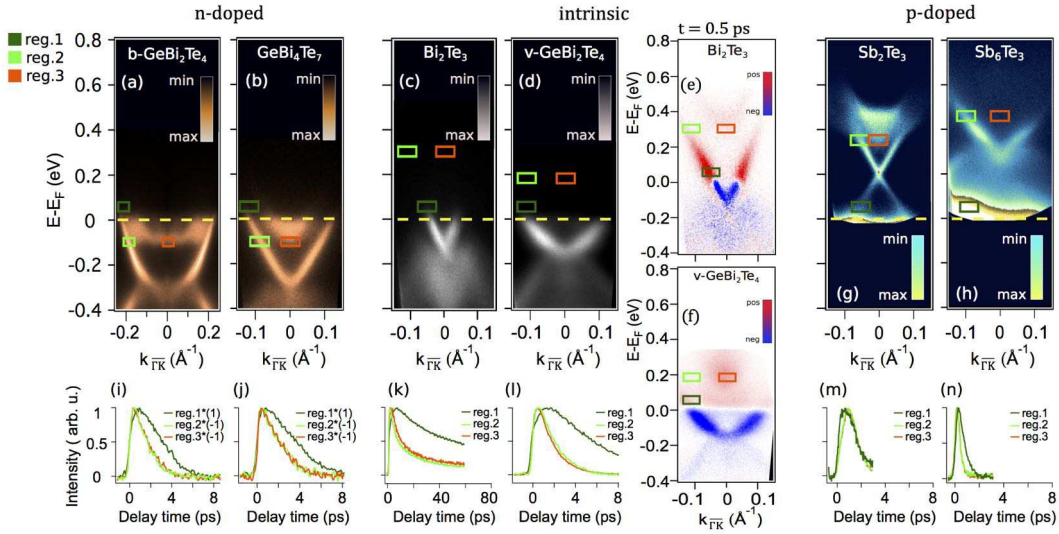

Figure 4.1: (Color online) (a - h) ARPES images of the bands measured along the $\overline{\Gamma K}$ high symmetry direction. (a) $\mathrm{b-GeBi_2Te_4}$ and (b) $\mathrm{GeBi_4Te_7}$ are n-type TIs, with the 3D bulk CB lying at $\mathrm{E_F}$. The data of panel (a) have been measured for negative wavevectors and successively they have been symmetrized. In the case of (c) $\mathrm{Bi_2Te_3}$ and (d) $\mathrm{v-GeBi_2Te_4}$, $\mathrm{E_F}$ lies within the bulk band gap. $\mathrm{E_F}$ is only crossed by the 2D SS and the materials are intrinsic TIs. (e) and (f), differential images obtained from the difference between the measured band dispersion after (+500 fs) and before (-500 fs) optical excitation for $\mathrm{Bi_2Te_3}$ (e) and $\mathrm{v-GeBi_2Te_4}$ (f). For (g) $\mathrm{Sb_2Te_3}$ and (h) $\mathrm{Sb_6Te_3}$, $\mathrm{E_F}$ is crossed by the 3D bulk VB and the samples are p-type TIs. The SS lies completely in the unoccupied density of states, and the data refer to the transient electronic population built by the optical excitation. (i - n) Temporal evolution of the corresponding electronic population after optical excitation, as integrated in the three regions indicated by colored rectangles in (a-d, g, h). The dynamics for the n- and p- type TIs are comparable and characterized by relaxation times of few ps, regardless of the specific position of $\mathrm{E_F}$ either within CB (i, j) or VB (m, n). On the contrary, for intrinsic TIs (k, l) the dynamics is much slower, and the intensity does not recover the equilibrium value in the investigated temporal window, exceeding 60 ps for $\mathrm{Bi_2Te_3}$ (k).

Furthermore, the Fermi level is found to intersects the VB, hence the two compounds fall in the p-type TIs group, as discussed extensively in ref.[69].

Before proceeding in comparing the out-of-equilibrium dynamics for the six distinct TIs, we point out that in each pair of compounds several specific details of the band structure are different. Besides the previously discussed energy position of the Dirac point, the minimum of CB and k_F, displays linearly dispersing SS ($\mathrm{GeBi_4Te_7}$, $\mathrm{Bi_2Te_3}$ and $\mathrm{Sb_2Te_3}$), whereas for

$GeBi_2Te_4$ and Sb_6Te_3 the SS dispersion looks more parabolic-like. For Sb_6Te_3 the parabolic (Rashba-like) dispersion, has been recently discussed as a consequence of the indirect gap closing, thus suggesting that this compound is probably a semimetal rather than a semiconductor [69]. Figure 4.1 (i - n) displays the temporal evolution of the electronic population averaged in energy-momentum windows of ($\simeq 20$) meV time 0.033 $Å^{-1}$. Three regions are selected for each compounds, those are indicated by colored rectangles in panels (a-d, g, h). In order to ease the comparison between the dynamics above and below E_F, we take them positive disregarding the sign.

For a thermalized electron system, where the out-of-equilibrium properties are fully accounted by the temporal evolution of the Fermi- Dirac (FD) distribution, the dynamics of the TR-ARPES intensity depends on the energy with respect to the E_F, as discussed in details for for Bi_2Te_3 [12, 65]. Hence, in order to correctly establish a comparison between different materials, we have decided to select one region at a fixed energy with respect to E_F. Region 1 (dark green) is located $\simeq 0.055eV$ above E_F along the dispersion of the SS.

The other two regions are selected according to the materials specific band structure. Region 2 (orange) corresponds to the minimum of the CB and region 3 (light green) refers to the same energy position of region 2, but along the SS dispersion. The correct assignment of the minimum of CB is trivial for n-type TIs, whereas for intrinsic and p-doped TIs is possible only immediately after the optical excitation.

Interestingly, we notice that the dynamics in fig. 4.1 (g,h) are similar, for n- and p-type respectively. In both cases the temporal evolution is slower in proximity of E_F than at the bottom of CB, as expected for a thermalized electron population [12, 65]. The dynamics are comparable, weakly dependent on the specific details of the band structures. For the two n-type TIs, after 7 ps the intensity has recovered the equilibrium. For the two p-type TIs, a slightly shorter time, 4 ps, is sufficient for the relaxation to be fully completed. The slightly faster dynamics for p-type and for n-type TIs cannot be easily interpreted in terms of cascade processes from the high energy CB toward E_F [10], as it will be discussed later in details later.

The most important result of our study consists in the observation that, for intrinsic TIs, the population dynamics requires a much longer time to recover the equilibrium value, as shown in fig.4.1 (k, l). In particular, for Bi_2Te_3 the intensity in region 1 reaches 60% of its maximum value within a temporal window of 60 ps, thus displaying a characteristic time more than one

order of magnitude larger than for n- and p-type TIs. In the case of $\mathrm{v-GeBi_2Te_4}$, the intensity after 8 ps is still 40% of the maximum excitation. Although longer than for n- and p-type TIs, the dynamics of the two intrinsic TIs show some differences. The sensitivity of the intrinsic TIs dynamics to the specific material properties might reflect a stronger influence of the surface band bending on the electron dynamics, a phenomenon that has been subject of a recent TR-ARPES study [15].

Furthermore, it is interesting to compare the dynamics of the intensity in region 1 and 3 for the intrinsic TIs. In fact, we observe that, after the fast increase due to the optical excitation, the electronic population at the bottom of CB (reg.3) rapidly decreases, whereas the dynamics at $\mathrm{E_F}$ (reg.1) is much slower. Such a different dynamics cannot be ascribed only to the temporal evolution of the FD distribution, as discussed for n-doped $\mathrm{Bi_2Se_3}$ [12, 65]. We propose that this different dynamics might reflect a cutoff of the electron population at the bottom of CB, thus suggesting that different relaxation mechanisms are at play in the bulk and surface states.

Having revealed this remarkably longer dynamics in intrinsic TIs, we have spent some efforts to clarify the observed difference between the n- and p-type TIs. In this perspective, we have evaluated the temporal evolution of the FD distribution for the six distinct materials. Following the analysis already proposed for $\mathrm{Bi_2Se_3}$ [11, 12, 15] we extract for each delay time the intensity distribution curves curves (EDCs) integrated along the SS dispersion, except for $\mathrm{Sb_2Te_3}$ and $\mathrm{Sb_6Te_3}$ where only VB crosses the $\mathrm{E_F}$. Figure 4.2 (a -f) show three selected EDCs extracted at a delay time immediately before (-0.5 ps, blue) after (0.5 ps. red) and 5 ps after (orange) the arrival of the pump.

We immediately notice that, in contrast to n- and p- type TIs for intrinsic at 5 ps the EDCs are still broader than at equilibrium, thus indicating a larger $\mathrm{T_e}$. In particular, for the case of $\mathrm{Sb_2Te_3}$, the electronic system seems not be fully thermalized within the experimental temporal resolution, in contrast to the case of n- and p-doped TIs. Thermalization is in general mediated by electron-electron scattering, as for example impact ionization between high-energy electrons and the electronic states below E_F. We speculate that the absence of 3D bulk states at EF, characterized by a large density of states, might affect the impact ionization process and the electron thermalization. In order to be more quantitative, each EDCs has been fitted with a function resulting from the product between a time-dependent FD distribution and a time independent polynomial function. The polynomial function describes the material DOS and it is optimized

for the data acquired at negative delay time. The product between the FD distribution and the DOS function is convolved with a gaussian distribution, accounting for the finite energy resolution. The best fit curves are shown in fig. 4.2 as black dash lines. The analysis provides us with the temporal evolution of $\mathrm{T_e}$, from which we can further address the microscopic scattering mechanisms responsible for the energy transfer within the band structure and between the electrons and the other degrees of freedom of the materials, as it will be discussed in the following section.

4.5 Discussion

Figure 4.3 reports the temporal evolution of the electronic temperature for the six distinct TIs, along with a schematization of our proposed diffusion relaxation mechanism. For n- and p- type TIs, the temporal evolution of $\mathrm{T_e}$ well mimics the electron population dynamics of fig. 4.1. In particular, a single exponential decay describes the full recovery of the equilibrium temperature within few ps.

For the n-type TIs, the characteristic relaxation times are $\tau \simeq 2.55 \pm 0.1$ ps for $\mathrm{b-GeBi_2Te_4}$ and $\tau \simeq 2.65 \pm 0.1$ ps for $\mathrm{GeBi_4Te_7}$. P-type TIs display slightly faster relaxation, with $\tau \simeq 2.5 \pm 0.1$ ps for $\mathrm{Sb_2Te_3}$ and $\tau \simeq 1.3 \pm 0.1$ ps for $\mathrm{Sb_6Te_3}$. Within the investigated temporal window, the electronic system is expected to be thermalized with the lattice [11, 12, 15]. The temperature dynamics is suggesting that after few ps no extra energy is retained neither in the electronic system nor in the lattice, and the equilibrium conditions are fully restored.

We propose the diffusion in the direction orthogonal to the surface to be responsible for this efficient energy dissipation. This process is mediated by the bulk states, either CB or VB, which enable to transfer hot electrons far from the surface, thus removing energy from the first few nm investigated by the surface sensitive TR-ARPES [15]. Figure 4.3 (g) and 4.3 (i) schematize our proposed bulk diffusion relaxation mechanism.

If $\mathrm{E_F}$ lies within CB (g) or VB (i), channels are available for electrons to delocalize deep in the crystal bulk. Bulk diffusion can be considered as the result of the temperature gradient in the direction orthogonal to the sample surface caused by the optical excitation. This process has already been proposed to fully account for the temporal evolution of $\mathrm{T_e}$ in bulk metals, such as Ru(111) [72] and Gd(0001)[73].

In intrinsic TIs we observe a different scenario. The diffusion process is still at play, and it is responsible for the emptying of the CB states above $\mathrm{E_F}$. However, a fraction of the excited electrons relaxes from CB into the SS, for which only in-plane diffusion is possible. Figure 4.3 (c) and (d) show that for $\mathrm{Bi_2Te_3}$ and $\mathrm{v-GeBi_2Te_4}$, $\mathrm{T_e}$ does not relax back to the equilibrium value in the investigated temporal window. In particular in $\mathrm{Bi_2Te_3}$, $\mathrm{T_e}$ after an exponential decay with $\tau \simeq 1.5 \pm 0.2$ forms a plateau that lasts longer than 60 ps. Similarly $\mathrm{v-GeBi_2Te_4}$ relaxes with fast decay ($\tau \simeq 3 \pm 0.2$) and ends with a plateau. We ascribe this hot state to the limited capability of the 2D surface electrons to diffuse, thus removing energy from the investigated region.

For intrinsic TIs, the electron-phonon scattering, and successively anharmonic phonon scattering is responsible for the lattice cooling. These processes take place at longer time scale. This is particularly true, if we consider that the reduce area of the SS Fermi surface imposes severe constrains on the phonons phase space available for scattering, similarly to the case of graphene [74, 75]. The sketch in Figure 4.3 (h) illustrate the intrinsic case, with $\mathrm{E_F}$ crossing only the SS, thus limiting the diffusion process at the surface.

We discuss now our results in view of the relevant models reported in literature. Previous TR-ARPES studies reported a long relaxation dynamics of the SS when the bulk CB is unoccupied [76, 15, 16]. These results were interpreted or in terms of cascade scattering from the high energy branches of CB towards $\mathrm{E_F}$ [10] or as the results of surface bend bending, trapping photoexcited charges at the surface [15]. In the former, the slow relaxation results from the impossibility to directly recombine electrons and holes from CB to VB, thus the electrons are proposed to relax back to the E_F through electron-phonon scattering along the SS. However, according to this model, the electron dynamics in the p-type TIS $\mathrm{Sb_2Te_3}$ and $\mathrm{Sb_6Te_3}$ should be longer, or at least comparable, to the one of the intrinsic TIs.

On the contrary, we have recorded the fastest relaxation dynamics in the p-type TIs, with timescale of few ps, in agreement with the experimental finding of other independent works [77, 78]. Hence, our results help in providing a more complete view of the scattering mechanisms, in particular when the effect of spatial diffusion is reduced by precisely selecting the doping level, as also proposed in Ref [10]. Concerning the surface band bending model, it accounts for the change in the charge dynamics as a function of the surface Coulomb potential. This potential tends to form charge accumulation layers at the surface by trapping hole or electrons,

according to the potential sign [15]. We expect the surface bend bending to affect the strength of the bulk diffusion mechanisms. As a result, different band bending at the surface of Bi_2Te_3 and $v - GeBi_2Te_4$ might explain their slightly different electron dynamics.

Finally, we compare our results with the recent TR-ARPES experiment reviewed in the prelude section, which has reported an extremely long relaxation dynamics at the surface of the bulk insulating TI Bi_2Te_2Se, exceeding 10^{-6}s [16]. This was experimentally compared to the faster timescale in n- or p-type TIs. Due to the limit temporal window accessible in our experimental results, we cannot resolve completely the full relaxation dynamics of Bi_2Te_3. However, the plateau observed for T_e in Fig. 3(c) suggests that the dynamics might take place on the scale of several hundred ps, and it might be comparable to the case of Bi_2Te_2Se [16]. Our results generalize these observations, by proving that the longer relaxation dynamics is a characteristic of intrinsic TIs, here shown for Bi_2Te_3 and $v - GeBi_2Te_4$. Moreover, we succeeded in proposing a model, based on our experimental data and the derived T_e dynamics, for describing the different relaxation dynamics in term of the different role played by the bulk and surface states, in the diffusion of the excited charges.

4.6 Conclusion

In summary, we have investigated by TR-ARPES the different contributions of the bulk and surface state to the out-of-equilibrium electronic properties of TIs, by studying six distinct compounds with different E_F within the band gap. The position of E_F as estimated by ARPES reflects the surface doping in the few topmost layers. We have observed that, if E_F is crossed by the bulk CB (n-type) or VB (p-type) states, the electron populations dynamics relax with similar characteristic time of few ps, regardless of the material specific details of the band structure, For intrinsic TIs, where E_F lies within the band gap, the relaxation dynamics is more than one order of magnitude slower.

The different dynamics has been discussed in term of the temporal evolution of T_e, which in intrinsic TIs does not relax back to the equilibrium value, in contrast to the n- and p-type TIs. We propose that the efficient removal of energy in the n- and p-type TIs results from diffusion processes in the direction orthogonal to the surface, mediated by the presence of 3D states at E_F providing charge channel deeply delocalized in the bulk. In contrast, in intrinsic TIs a fraction of

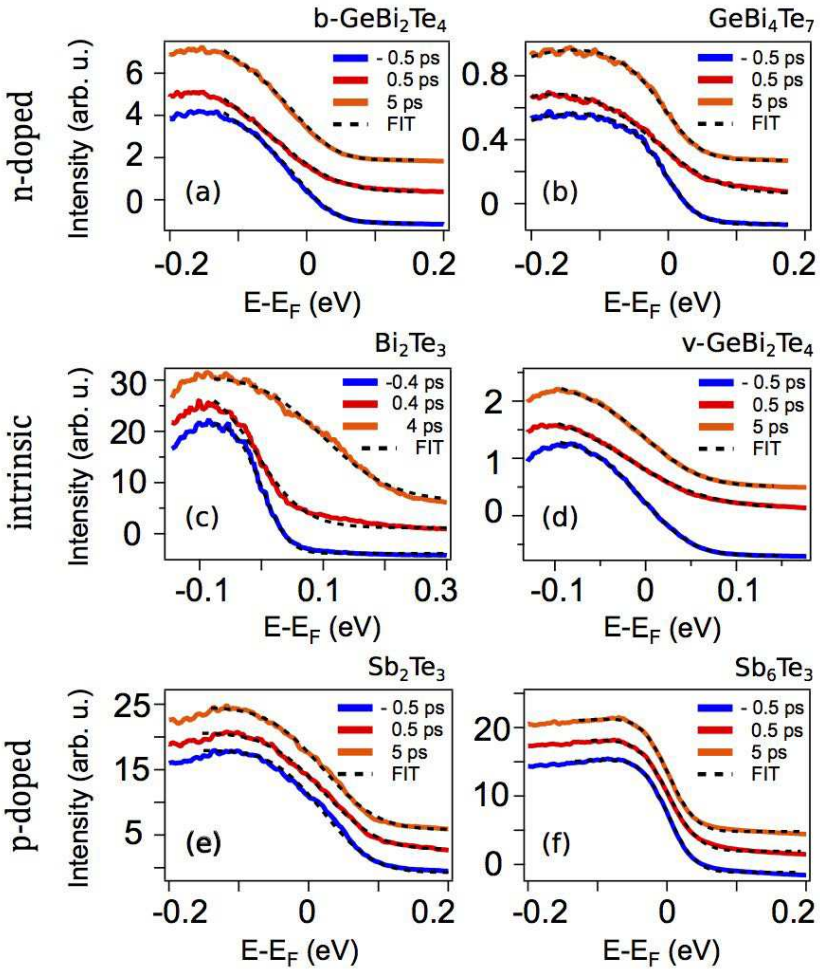

Figure 4.2: (Color online) (a - f) Intensity distribution curves as a function of energy (EDCs) extracted along the SS dispersion for (a) b $-$ $GeBi_2Te_4$, (b) $GeBi_4Te_7$, (c) Bi_2Te_3 and (d) $GeBi_2Te_4$. For the p-type TIs (e) Sb_2Te_3 and (f) Sb_6Te_3, the EDCs are taken along the dispersion of the bulk VB crossing E_F. For each compounds, the three EDCs are taken immediately before (blue) after (red) and 5 ps after (orange) the arrival of the optical excitation. Black dashed lines show the best fit, resulting from the product between the time dependent FD distribution and a time independent function describing the material DOS. This is further convolved with a gaussian accounting for the finite energy resolution.

the energy is retained by the 2D SS, for which in-plane diffusion is not an efficient mechanism to remove energy from the shallow region investigated by the surface sensitive TR-ARPES. The fast relaxation, observed once the chemical potential crosses 3D bulk states, can be also related to the presence of a larger phase space available for the electron-holes annihilation. The bulk

energy gap can also play an important role in the relaxation processes, indeed it presence no longer protects from the phonon emission. However, we have no direct experimental evidences to support this hypothesis.

The long dynamics observed in intrinsic Bi_2Te_3, and similarly in Bi_2Te_2Se [16] suggest these compounds as test samples to investigate the effects of phase space restriction in the electronic relaxation processes. In particular, due to the linear dispersion and the spin helicity of the SS, supercollision [74, 69] and the protection from elastic backscattering [79] might affect the electron scattering. Our results highlight the different contributions of 3D bulk states and 2D SS to diffusive mechanisms. A realistic diffusion model can be considered, as a future perspective, to further investigate the differences between in-plane and out-of-plane diffusion processes. Moreover, such model can be used to quantify the electron motion out of the region probed by the ARPES.

Diffusive relaxation processes have been reported also in the recent TR-ARPES studies on TIs [16]. Nonetheless, with the present study we prove that the bulk diffusive relaxation mechanism is more general and it might play a major role also in the out-of-equilibrium physics of other materials.

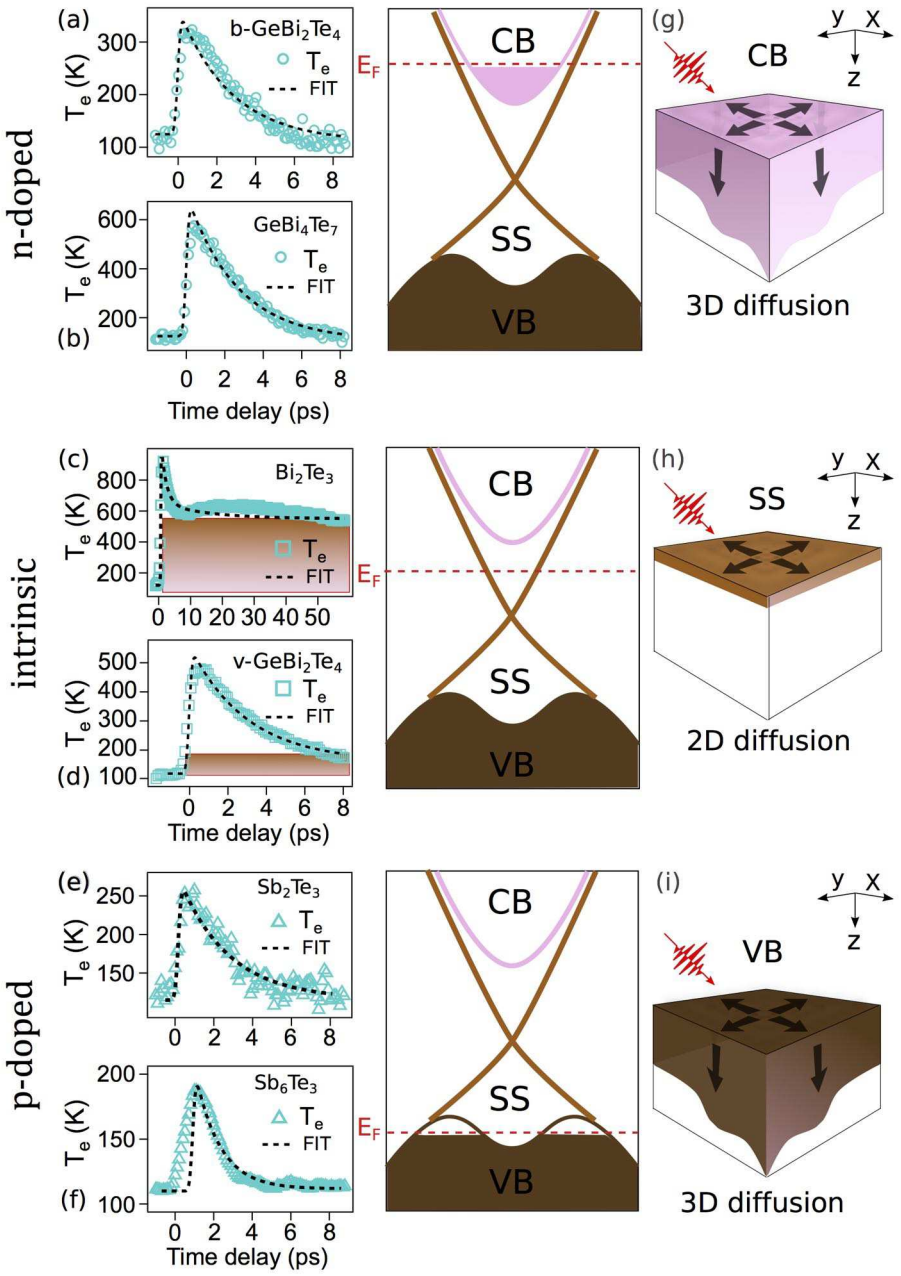

Figure 4.3: (Color online) (a - f) Temporal evolutions of T_e as extracted from the fit to the EDCs of fig. 4.2. For the (a, b) n- and (e, f) p- type TIs, T_e recovers the equilibrium value with characteristic time of few ps. On the contrary, in intrinsic TIs (c, d) T_e does not relax back to the equilibrium value, but it forma a plateau, indicated by the grey area. (g - i) Schematizations of our proposed diffusion model. If bulk states, either CB (g) or VB (i), cross E_F 3D states are available for the excited charges to diffuse in the bulk, out of the few nm region investigated by surface sensitive TR-ARPES. Whereas, if E_F lies within the band gap, part of the energy is trapped in the 2D SS, for which in-plane diffusion is not an efficient way to remove energy from the electronic system.

Chapter 5

SmB_6: A Strongly-Correlated Kondo Topological Insulator

SmB_6 is a strongly correlated electron-system which is attracting a large interest year after its discovery. It is considered, indeed, one of the first Kondo Insulator (KI)[80] and it has been proposed, recently, as the first Topological Kondo Insulator (TKI) [17]. Several experiments have been performed in order to clarify the origin of its anomalous low-temperature transport properties as well as to understand its topological nature [17, 81, 82]. Nevertheless, this question is controversial and still under debate because of the complex band structure characterized by a narrow Kondo energy gap. In this chapter, as a prelude to the experimental results, we briefly report on the main properties of this material within the classes of KI and TKI. The recent transport and ARPES investigations that constitute nowadays the state of the art on this topic will be summarized.

5.1 The Discovery of the First Kondo Insulator

SmB_6, discovered in 1969 by A. Menth [80], is a heavy electron material considered as the forefather of Kondo Insulators (KIs). Menth et al. have observed that when this material is cooled below a certain temperature, defined as Kondo temperature (T_K) the resistivity departs from the conventional metallic behaviour (reduction of resistivity when lowering the temperature, because of a reduction of the scattering rate) and showing an upturn with a monotonic increasing

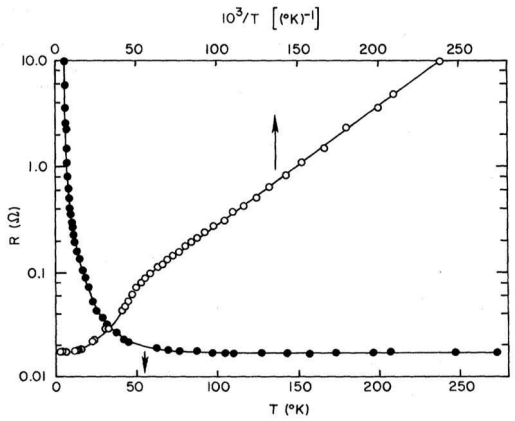

Figure 5.1: Resistance versus Temperature (closed circles) and resistance versus $10^3/T$ (closed circles). Adapted from [80].

for $T < \mathrm{T_K}$. This observation is considered as the fingerprint of a modification of the electronic structure of the material, the opening of a energy gap that turns the metal into a semiconductor at $\mathrm{T_K}$.

Figure 5.1 reports such effect for $\mathrm{SmB_6}$ through the characteristic behaviour of the resistance versus temperature curve. The resistance starts to increase below 50 K and saturates at 3 K. This phenomenon has been initially interpreted as a change of the electronic configuration of Sm ions. Interestingly, it was noticed that in the low temperature regime (below the 3 K) this material does not show evidences of magnetic ordering, in contrast to other magnetic rare earth exaboride [80]. Hence, an intimate connection between the semiconducting and the magnetic properties was expected.

Successively several detailed studies have focused on the $\mathrm{SmB_6}$ anomalous conductivity. Allen et al. have shown that the $\mathrm{SmB_6}$ resistivity ρ, rapidly increases below 30 K reaching a saturation value [83]. They have reported a size of the resistivity increase in the order of $\sim 10^4$ and that saturates at ~ 3 K. Their study has focused on the dependence of both the Hall coefficient R_H on temperature and on the estimated carriers concentration. By considering that the charge concentration ranges from $\simeq 9 \cdot 10^{21}/cm^3$ at room temperature to $\simeq 5 \cdot 10^{17}/cm^3$ at 4 K, they have classified the $\mathrm{SmB_6}$ as a "bad" metal [83]. In the temperature range below 4K, they have noticed that the amount of the resistivity increase is too large to be ascribed to a conventional scattering mechanisms.

Finally, they attributed this resistivity change to a decrease in the carriers concentration.

These finding indicates the presence of a small energy gap. These initial experimental findings have prompted several further studies about the origin of the observed residual low-temperature conductivity, as we will see in the upcoming section.

5.2 Kondo and Topological Kondo systems

The KIs class has been formally proposed many years after the SmB_6 discovery [84]. At present includes a significant number of compounds, like the YB_6 [85], the SmS[1] (under high pressure condition) [86], YbB_{12}, $CeFe_4P_{12}$ and also the d-electron material $FeSi$ [87].

KIs are often classified like "simple" local magnetic-moment metals, since they show at high temperature, a classic Curie-Weiss magnetic susceptibility [87]. At low temperature, due to the Kondo effect, the strength of the antiferromagnetic interaction between local magnetic moments and the conduction electrons grows, leading to Kondo screening of the local moments. This screening effect leads to the formation of a paramagnetic Kondo ground state, which is accompanied by the creation of a narrow gap [84, 87].

The Kondo effect, originally observed by J. Kondo in 1964 in magnetic alloys, describes the energy gap opening and the characteristic change in the electrical resistivity with temperature as a result of the scattering of conduction electrons due to magnetic impurities [88]. In a Kondo insulating state, Kondo singlets scatter electrons without conserving the momentum, giving rise to a huge build-up of resistivity al low temperature [89]. Whereas in a lattice with translational symmetry, the elastic scattering between electron and purities conserves momentum, hence leading to a coherent scattering of Kondo singlets [89].

New models have been proposed, afterwards, to describe the physics of Kondo systems, such as the *Kondo lattice model* introduced by S. Doniach [90]. This model can be described by a lattice of localized magnetic moments *immersed in a sea* of mobile electrons. Its metal or insulating behaviour is determined, within this picture, by the competition of two effects: the Kondo effect and the RKKY (Ruderman-Kittel-Kasuya-Yoshida) magnetic interaction. The first effect screens the local moments hence leading to the formation of the insulating-paramagnetic ground state. The latter, in contrast to the first, leads to a magnetic ordered metallic state.

[1] SmS is the first system which exhibits, under high pressure, a paramagnetic behaviour similarly to SmB_6.

Singlets formation takes place below the Kondo Temperature T_K, expressed by [87]:

$$T_K = D\sqrt{J\rho}\exp\left\{-\frac{1}{sJ\rho}\right\} \tag{5.1}$$

where J is the Kondo coupling, D represents the value of the maximum electron energy state below the E_F and ρ is the density of states. The RKKY interaction shows a characteristic temperature $T_{RKKY} \simeq J^2\rho$. In the temperature regime where T_K exceeds T_{RKKY}, the Kondo effect dominates and the singlet ground state is formed.

The Kondo lattice is described by an hamiltonian which consists of the sum of two terms, proportional to the hopping *t* and to the antiferromagnetic Kongo coupling *J* [90].

A Kondo insulator can be explained, in a simple picture, the Kondo lattice model in the limit of strong coupling. This is realized when the coupling constant J is much larger with respect to the hopping term *t*. The hopping term is considered, in that case, as a perturbation to the onsite Kondo interaction. An alternative way to interpret Kondo systems is based on the Anderson Lattice Model (ALM), which has been proposed by R. Martin and J. Allen [91]. They have proposed a Kondo lattice hamiltonian consisting of three main terms [87]:

$$\hat{H}_{ALM} = \hat{H}_f + \hat{H}_c + \hat{H}_{hyb} \tag{5.2}$$

$\hat{H}_f$ describes localized f-states at each atomic site. It accounts for the corresponding Coulomb repulsive interaction U and the hopping amplitude between neighbouring lattice sites. The second term,$\hat{H}_c$, accounts for a band of non interacting conduction electrons. Finally the third term $\hat{H}_{hyb}$ describes the hybridization between localized f-states and conduction electrons. By considering as a starting point a simple hybridized band structure with a direct band gap, the Kondo state can be reached by increasing adiabatically the Coulomb interaction U. As a consequence the coupling constant $J \simeq \frac{V^2}{U}$ reduces and the energy gap is renormalized[2].

M. Dzero *et al.* have proposed a theoretical work which can be considered as a "turning point" for the evolution of KIs. They have suggested that Kondo insulators can develop a strongly interacting-electrons version of topological insulators, thus predicting the birth of the so-called Topological Kondo Insulator (TKI) phase [87]. The authors have proposed $\mathrm{SmB_6}$ as the first candidate of this class of compounds, on the base of its topological classification [17].

[2]This model is often regarded as the renormalized Anderson model. The renormalization involves in general other important parameters in addition to the energy gap which are determined by the Kondo temperature.

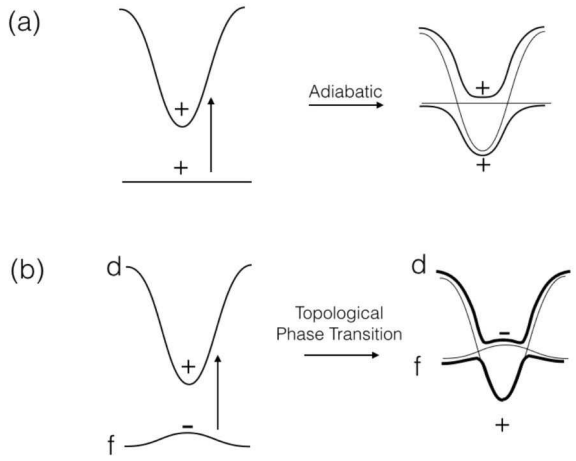

Figure 5.2: (a) Two bands of the same parity repel one-another and do not cross when the interaction is turned on adiabatically. (b)The two bands have opposite parities, like in the topological insulator case. In this case the interactions can cause f-band to move up into a d-band, leading to band-crossing and to a topological phase transition. Adapted from [80].

M. Dzero and coworkers have suggested that there is a subset of KIs which is topologically non trivial and which displays a strong spin orbit coupling associated to f-electrons. The f-electrons spin-orbit coupling, which is of the order of 0.5 eV, is much larger then the narrow Kondo gap (10 meV). The parity of f-states and d-bands, odd and even respectively, would lead to a change in the Z_2 topological invariants at each band-crossing point. Depending on the number of crossing along an high symmetry direction which connects two TRIMs, (as we seen in the previous chapter), KIs can be TIs. The electron-interaction U_f, depending on the band parities, can lead to the formation of a topological phase in a KI. If two bands of same parity are considered, when the interaction U is turned on they "repeal" each other, as shown in fig. 5.2 (a). In the case of a d- and f-band with different parity (fig. 5.2 (b)), switching on the interaction opens the possibility of a band crossing. If, as as a result of this process, the f- and d- bands cross at an odd number of points, then a topological phase transition will take place into a topological insulator [87].

Several studies, based on tight-binding models, have been proposed to better understand the physical properties of $\mathrm{SmB_6}$. Calculations performed in [92, 93] have predicted that the non interacting-electron band structure is topologically non trivial and Sm-4f orbitals hybridize only with Sm-5d orbitals. T. Takamoto [94] has adopted a tight-binding model based on the ALM

hamiltonian in which the hopping amplitudes are extended to near and next-near neighbours. As a result, a single d-like orbital is supposed to invert his energy ordering with a f-like orbital at the X point the in bulk Brillouin zone and three Dirac cones are expected to form at the surface with vacuum.

5.3 Recent Experimental Progress on the SmB_6 Topological Kondo Insulator

The main experimental findings previously discussed, allow us to draw the conclusions that SmB_6 behaves as a weakly correlated metal at high temperature, becoming insulating[3] below 40 K, with the opening of the Kondo gap. However, SmB_6 also presents a residual saturating resistance al low temperature.

Originally the resistance observed below 4K, has been ascribed to bulk impurities. However, later on, thanks to the improved sample quality, this hypothesis has been confuted [83, 95, 96]. The prediction of the topological nature of SmB_6 has shed new light on the possible interpretation of such a phenomenon. Indeed, the low temperature resistivity has been assigned to the existence of a topological surface state. Various experiments were carried out, with the aim of revealing the presence of in-gap states, hence confirming the topological nature of the SmB_6.

Various transport experiments have been performed in order to distinguish surface and bulk derived contributions [95, 97, 98]. Zhang et al. have measured the capacitive self-oscillation effect in SmB_6 single crystals, observing an anomalous capacitance which has been ascribed to surface carriers [53]. To distinguish among surface- or bulk-dominated conduction, they have studied the bulk density of states (DOS) by means of point contact spectroscopy (PCS). They have revealed that in the 10 to 2 K temperature range the conductance spectra remain unchanged, hence the bulk remains insulating during the resistance saturation. The most "natural" explanation, as the authors claim, consists in the surface metallic conduction [53].

Surface and bulk contributions are, as expected, strictly related to the size and shape of the sample under investigation. By considering this basic principle the SmB_6 Hall coefficient has been measured at different temperatures by varying the sample thickness [95]. In the high tem-

[3]The formation of the insulating phase is observed when the Fermi level lies within the Kondo energy gap.

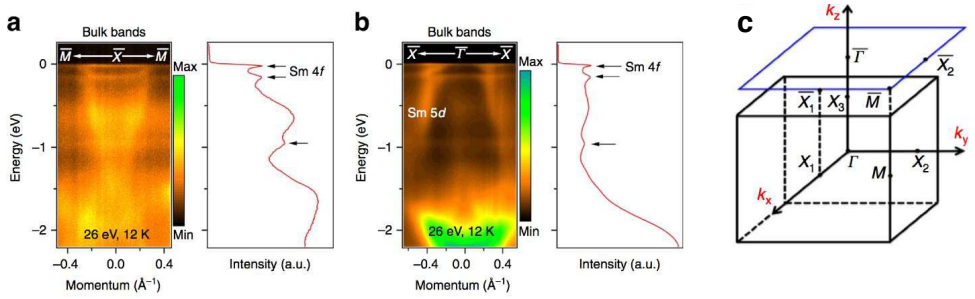

Figure 5.3: Synchrotron-based ARPES maps along the $\bar{M}-\bar{X}-\bar{M}$ (a) and $\bar{X}-\bar{\Gamma}-\bar{X}$ (b) momentum space directions. The dispersive Sm 5d band and the non-dispersive flat Sm 4f bands are observed, confirming the key ingredient of a heavy fermion Kondo system. The momentum-integrated energy distribution curves are also shown. The bulk and surface BZs of SmB_6 and the high-symmetry points are marked. Adapted from [81].

perature regime the Hall resistance was found to be inversely proportional to the sample thickness, which is consistent with a bulk transport behaviour. On the contrary, below 4 K, the Hall resistance has become linearly proportional to the thickness, indicating a surface conduction.

The ARPES technique, thanks to its ability to probe with high energy- and momentum-resolutions the surface electronic band structure, has been adopted to look for a direct signature of the topological nature of SmB_6. This last part of the chapter is devoted to a review of relevant works dealing with the SmB_6 electronic band structure, measured by means of high-resolution ARPES and spin-resolved ARPES (SARPES) measurements.

The work of Neupane et al. has filled the lack of high-resolution studies of the SmB_6 surface electronic structure as a function of the temperature [81]. They state that a "better energy resolution than 5 meV and 7 K temperature combination" is required to identify the in-gap states and to perform a Fermi surface mapping. In order to fulfil these conditions the authors both high-resolution laser based and synchrotron based ARPES study. In figure 5.3 (a-b) the band structure measured at low temperature (12 K) and along two inequivalent high symmetry directions is shown. Directions are $\bar{M}-\bar{X}-\bar{M}$ and $\bar{X}-\bar{G}-\bar{X}$, in (a) and (b) respectively. In fig. 5.3 In proximity of the Fermi level the flat f-bands are clearly visible. Their energy position can be inferred from the integrated energy distribution curves. The non-dispersive f-bands correspond to the ${}^6H_{5/2}$, ${}^6H_{7/2}$ and ${}^6F$ multiplets of the Sm^2 (f^6 - f^5) final states, respectively [81]. Sm 5d-derived dispersive bands are also indicated in fig. 5.3 panel (b).

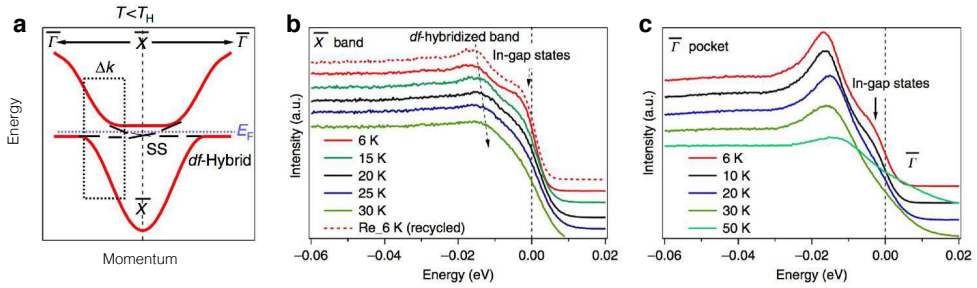

Figure 5.4: Cartoon sketch depicting the electronic band structure in the insulating phase, with the hybridization gap opened (a). The black dash rectangle indicates the approximate momentum window of ARPES spectra reported in panel (b-c). Temperature dependent momentum-integrated ARPES spectral intensity centred at the X point (b) and at the Γ pocket (c). Adapted from [81].

The Kondo hybridization process is predicted to occur in proximity of the X points in the bulk BZ and near their projections on the (100) surface: $\bar{X}_1$, $\bar{X}_2$, $\bar{\Gamma}$ (indicated in fig. 5.3 panel (c)). As Neupane *et al.* have investigated by integrating in a narrow (± 0.15) Å^{-1} momentum region around the $\bar{X}$ point, the evolution of the ARPES spectral intensity with temperature. The corresponding ARPES EDCs, reported in fig. 5.4, revealed the onset of a shoulder at E_F that they attribute to the presence of in-gap metallic states. Such spectral feature is observed in proximity of both $\bar{X}$ and $\bar{\Gamma}$ points.

The authors have also studied the Fermi surface topology, reporting that their experimental results are consistent with the theoretically predicted contour of the topologically protected surface state in the TKI ground-state phase [81]. As the authors have noticed, the details of the bands dispersion within the Kondo gap are not well resolved and this is attributed to the unavoidable quasi particle life-time broadening. Finally, they have performed a photon-energy study to confirm the two-dimensional dispersion of the topological surface states within a narrow energy region around the Fermi level (10 meV). By comparing the momentum cuts measured at different photon energies they have concluded that the states show no evident k_z dispersion, hence supporting the two-dimensional nature of the in-gap states. However, also bands lying 10 meV above the E_F, which are not predicted to be surface-derived, show no evident k_z dispersion. As noticed in the last part of the work, the lack of k_z dispersion shown by out-of-gap states is unexpected. The authors propose different interpretations, without clarifying the question at all.

TIs posses, with respect to trivial material, a linear dispersive surface state with unique spin

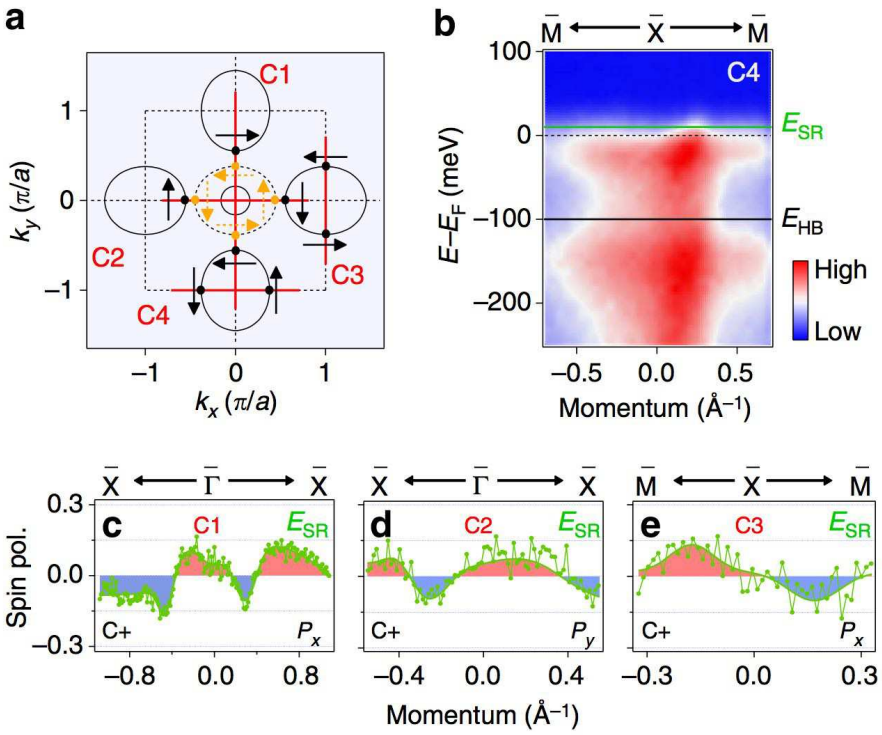

Figure 5.5: In panel (a) the spin polarization of the surface states observed along the high-symmetry lines is reported. The red lines - (C_1, C_2, C_3 and C_4) indicate the locations of the spin measurements in the k_x, k_y plane (a). In panel (b) the states along the high-symmetry $\bar{M} - \bar{X} - \bar{M}$direction near the E_F and measured with 30 eV photon energy are shown. Panel (c) - (e) show the spin signal measured at 30, 30 and 26 eV respectively at points C1, C2 and C3, with the spin polarization along the x, y and x directions respectively. Adapted from [99].

texture. SARPES has been often adopted to probe this spin polarized Dirac cone and hence to distinguish TIs from topologically-trivial insulars. Xu et al., by exploiting this technique, have carried out a spin-resolved ARPES investigation of SmB_6 in order to observe the predicted spin polarized topological surface states [99]. The spin polarization signal, which has been attributed to the surface state, has been acquired by measuring along high symmetry directions, in proximity of the $\bar{X}$ points and at 20 K (Kondo gap fully opened). Figure 5.5 (c-e) show the SARPES measurements performed at 10 meV above the Fermi level and along the C cuts [99].

Xu *et al.* claim that their findings, consisting of a clear spin texture and n-odd number of pockets, are fully consistent with their prediction of SmB_6 as a TKI. Their SARPES data

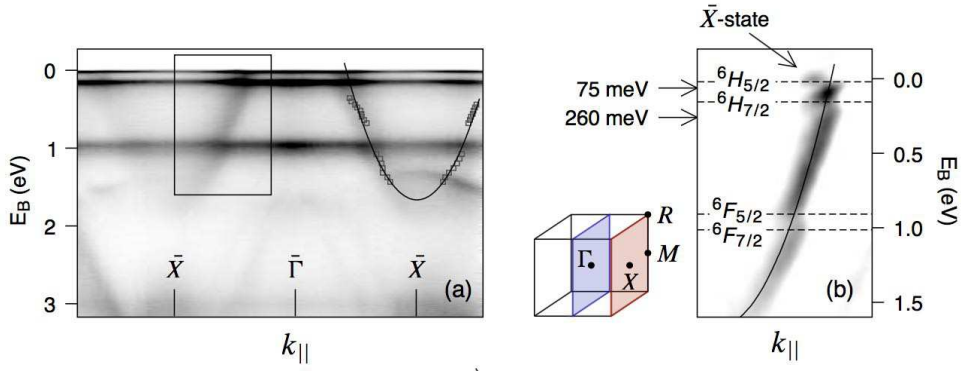

Figure 5.6: Photoemission intensity along $\bar{X} - \bar{\Gamma} - \bar{X}$ obtained with $h\nu$ = 70 eV. Markers indicate position of maxima in fits of momentum distribution curves, solid line is a parabolic fit to these points. (b) Second derivative (d^2I/dk^2) of the area marked in (a) [82].

assign to the surface band located at the $\bar{X}$ points a anti-clock wise spin polarization, in analogy to the case of 3D TIs [99]. The ARPES [81] and SARPES [99] studies reviewed previously, represent the state-of-the-art of experimental works supporting the non-trivial topological nature of SmB_6. However, we conclude this section by briefly describing a relevant study which seems to invalidate the previous findings, asserting that the SmB_6 is a trivial surface conductor [82].

Hlawenka et al. have measured, at low temperature (1K), bands located at the $\bar{\Gamma}$ point in the surface Brillouin zone (SBZ), reporting trivial metallic state instead of a topological surface state. From their ARPES data, they have evinced a topologically-trivial scenario, which is illustrated schematically in fig. 5.7.

At the $\bar{X}$ point of the SBZ a massive free-electron like states are observed instead of a topological surface state, shown in fig. 5.7. The fact that the surface remains metallic in the low temperature regime is explained by considering that the gap is shifted away from the Fermi level due to a surface core level shift of the 4f level [82]. Moreover, as has been previously observed in [100], the metallic state measured at the $\bar{X}$ point [81], is considered by the authors in this work as the continuation of the bulk d-band. Concerning the topological spin texture which has been observed by Xu et al [99], the authors point out the possibility that it could also be a spin-polarized Rashba-split state of considerable extent in k-space, as they have observed at $\bar{\Gamma}$. They finally conclude by asserting that the ultimate energy resolution of spin-resolved ARPES measurements is too poor to distinguish between the surface state and the f-orbital multiplet.

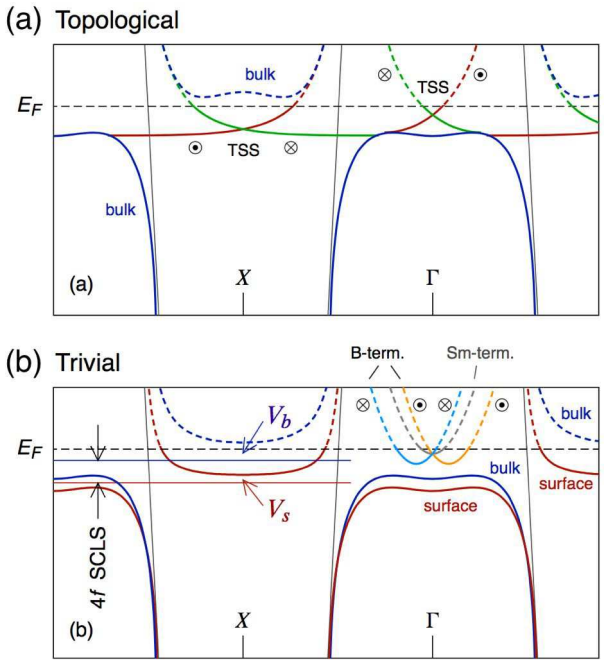

Figure 5.7: Sketch of the situation predicted by works supporting the topological nature of SmB6 (a), and the different scenario based on the experiment of Hlawenka et al (b). Extracted from [82].

5.4 A Preliminary Pump and Probe Photoemission Spectroscopy Investigation

Recently, Ishida and coworkers carried out the first TR-ARPES study on $\mathrm{SmB_6}$, aimed at revealing pump-induced effects on pico-to-microseconds time scale [101]. The most remarkable result that they have reported consists of a pump-induced energy shift of the ARPES spectra, in the valence band at low temperature (10 K). The observed shift of the chemical potential ($\Delta\mu$) presents both a a pump-power dependence and a remarkable temperature-dependence. By evaluating the response to different pump fluences, the authors have excluded that the shift $\Delta\mu$ could be originated from charging of the sample surface. Whereas the temperature dependence, reported in fig. 5.8 (a), shows that the shift is negligible above 90 K and increases, up to ~ 4 meV, at temperature lower than T_K.

Ishida *et al.* have ascribed this effect to a surface photovoltage (SPV), which is supposed to

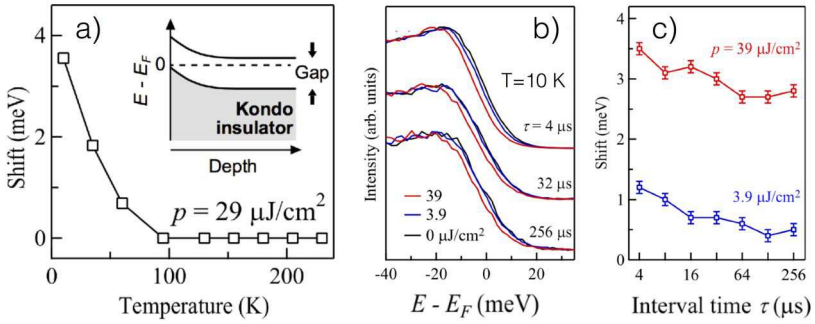

Figure 5.8: $\Delta\mu$ as extracted at three values of delay time and with three pump fluences, panel (a). Duration of the shift with respect to different delay times. Panel (b). [101].

be a consequence of an optically-induced surface bend bending [101]. This SPV effect persists, after the arrival of the pump, up to 200 μs. Such a long lasting duration is displayed in fig. 5.8 (c). As shown by fig. 5.8 (b) and fig. 5.8 (c), the optically induced shift monotonically decreases as the delay time increases. To probe a temporal windows in the order of hundreds of μs, they have adopted the following approach. The delay τ between pump and probe pulses has been fixed, while varying the repetition rate. Hence, the sample has been irradiated at the interval of 4 μs and at multiples values (repetition rate is 250 KHz).

The second part of their study is focused on the initial electron dynamics induced by the pump in the femto-to-picoseconds probed by changing mechanically the optical path as for typical pump-probe experiments. The signal has been measured, in that case, by fixing the repetition rate and by varying the delay τ by changing mechanically the length of the pump optical path.

The photoemission intensity, integrated above the Fermi level, is presented in fig. 5.9 with respect the delay time and at different temperatures, in different colors. The x-axis is plotted in both a linear and a logarithmic time scale. The linear time scale allows to appreciate the temporal evolution during the first pico-seconds, and the second (logarithmic) shows long dynamics which persist up to 100 ps. The authors have noticed that dynamics shown in fig. 5.9 present a cross-over point at 0.5 ps, which has been interpreted as the presence of a bottleneck effect during the electron end phonon thermalization process. The bottleneck is clearly visible in the temperature regime under 90 K, however as authors have showed, is it present also above this value. The slow relaxation after 0.5 ps is attributed to the heat transfer from the electronic to the lattice system.

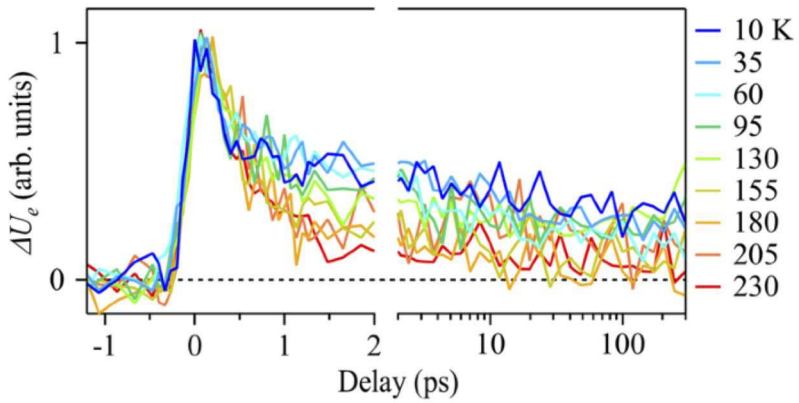

Figure 5.9: $\Delta\mu$ as extracted at three values of delay time and with three pump fluences, panel (a). Duration of the shift with respect to different delay times. Panel (b). [101].

The study proposed Y.Ishida et al., provides important informations about the overall response of the electronic system following the optical excitation. The authors claim that the observed relaxation dynamics may be interpreted by means of a two-temperature (2T) model. However, to clarify this point and to establish the metallic or semi-conducting response of the this material, a more qualitative study is needed. Inspired by Ishida's work we have performed a TR-ARPES study aimed at evaluating the temporal evolution of the electronic temperature of the system. Successively, as we will show in the next chapter, a 2T- based model has been adopted to extract further important informations as the characteristic electron-phonon coupling constant λ_{e-ph}.

Chapter 6

Samarium Hexaboride Electron-Phonon Coupling Constant from Tr-ARPES

We have investigated the SmB_6 out-of-equilibrium electron dynamics by means of time and angle resolved photoelectron spectroscopy (tr-ARPES). The transient electronic population above the Fermi level can be described by a time dependent Fermi-Dirac distribution. By solving a two temperature model, that well reproduces the relaxation dynamics of the effective electronic temperature, we estimate the electron-phonon coupling constant λ to range from 0.13 ± 0.03 to 0.04 ± 0.01. These extrema are obtained by assuming a coupling of the electrons with either a phonon mode at 10 meV or at 19 meV. A realistic value of the average phonon energy will give an actual value of λ within this range. Our results provide a new experimental report on the electron-phonon coupling of this material, contributing to both the electronic transport and the macroscopic thermodynamic properties of SmB_6.

6.1 Introduction and Motivations

The electronic transport properties of SmB_6, introduced in the previous chapter, have been the subject of intense studies since the first report of its mixed valence nature [102] and the observation of a Kondo gap opening when cooling it below $T_K \sim 50$ K [83]. This Kondo gap

opens as a result of the interaction between the delocalized d-electrons and the f-electrons acting as localized magnetic impurities [103]. Despite the observation of a gap opening at the Fermi level by spectroscopic measurements, transport experiments show signs of residual conductivity [96]. The origin of this residual conductivity has puzzled the scientific community until the recent discovery of low temperature metallic surface states [104], of potential, albeit debated, topological character [17, 78, 81, 82, 99, 100, 105, 106, 107]. The advent of topological insulators (TIs) has fuelled the fast development of time-resolved ARPES (tr-ARPES) [10, 11, 12, 13, 14, 32, 65]. This technique has been successfully exploited to access the unoccupied electronic states [12, 14] as well as the temporal evolution of both the chemical potential (μ) and the electronic temperature ($\mathrm{T_e}$) after optical excitation [12, 13].

In this chapter we report on the out-of-equilibrium electronic properties of $\mathrm{SmB_6}$ as revealed by tr-ARPES. This study is motivated by the possibility to address the scattering mechanisms in $\mathrm{SmB_6}$, as similarly reported for Bi based binary TIs. Ishida and coworkers have pioneered this out-of-equilibrium approach to the study of $\mathrm{SmB_6}$, reporting a shift of the chemical potential ($\Delta\mu$) lasting up to hundreds of μs after optical excitation, for $\mathrm{T} < \mathrm{T_k}$ [101]. By assessing the out-of-equilibrium dynamics of $\mathrm{T_e}$, here we provide new insights on the temporal evolution of the time-dependent Fermi-Dirac (FD) distribution.

A two temperatures model (2TM) is applied to mimic the relaxation dynamics of $\mathrm{T_e}$. By considering a coupling to phonon energies corresponding to the lowest energy Sm modes at 10 meV [108, 109] or 19 meV [110] $-$ 20 meV [109], we estimate an interval for the possible values of the electron-phonon coupling constant λ: 0.13 ± 0.03 to 0.04 ± 0.01. This range is mostly determined by the fact that among the phonon modes detected for this material those derived from the $\mathrm{B_6}$ cage, i.e. those at energies > 20 meV, are expected to weakly contribute. This finding can be of relevance to account for the details of the electronic transport and thermodynamical properties of $\mathrm{SmB_6}$ [111]. In addition to the temporal evolution of the FD function, we reveal a difference in the effect of the optical excitation on the d- and f-states. In particular, the depletion of intensity which follows the optical excitation mainly affects the f-bands. The electrons, which are excited in the f-state above the Fermi level ($\mathrm{E_F}$), successively relax towards $\mathrm{E_F}$ where intensity is observed over a broad momentum range. This observation suggests the transient population of empty f-states above $\mathrm{E_F}$[112].

Tr-ARPES experiments have been performed at the T-ReX Laboratory, Elettra (Trieste,

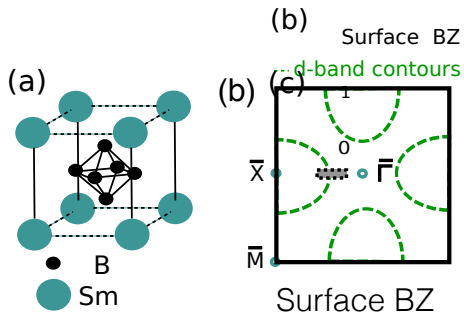

Figure 6.1: (a) SmB_6 unit cell of the CsCl-type. Sm atoms (teal) and a B_6 cage (black) occupy the corners and the body-centered position of the cubic cell. (b) Brillouin zone projected on the (001) cleavage plane. The measured momentum range along the $\overline{\Gamma X}$ high symmetry direction is indicated by a grey rectangle.

Italy). More details about the setup can be found in the second chapter. The photoelectrons are collected and analyzed by a SPECS Phoibos 225 hemispherical spectrometer, with energy and angular resolution set in the present experiment to 30 meV and 0.2°, respectively. The overall temporal resolution is about 250 fs. In the following, two data sets are analyzed with an absorbed fluence equal to $120 \pm 25\,\mu$J/cm^2 and $75 \pm 15\,\mu$J/cm^2, corresponding to an absorbed energy density equal to 30 ± 6 J/cm^3 and 19 ± 4 J/cm^3, calculated by considering a penetration depth of 40 nm, as estimated from optical studies [113]. For the calculation of the absorbed fluence and energy density, a reflectivity R=0.5 at 1.55 eV has been considered [113].

Single crystals of SmB_6 were grown via optical floating zone technique, as described in Ref. [114]. They are cleaved in UHV at room temperature and transferred to a variable temperature cryostat. Measurements are performed at an equilibrium temperature of $\sim$120 K. At this temperature the Kondo gap is fully closed and the material transport properties are metallic, a condition necessary for the use of a 2TM.

6.2 Equilibrium and Out-of-Equilibrium Electronic Band Structure

SmB_6 crystallizes in the CsCl-type structure with $Pm3m$ point group symmetry and lattice constant $a = 4.13$ Å. Sm atoms and a B_6 cage occupy the corners and the body-centered position of the cubic cell, as depicted in fig 6.1 (a). Sample cleavage exposes the (001) surface, and the

corresponding projected surface Brillouin zone is shown in fig. 6.1 (b).

Tr-ARPES measurements have been carried out along the $\overline{\Gamma X}$ high symmetry direction, in the region indicated by the grey rectangle. The d-bands are expected to cross $\mathrm{E_F}$ within this momentum window, as illustrated by the green dashed lines schematizing the d-band contour [78, 82, 99, 100, 106, 115].

Figure 6.2 (a) shows the band structure ~ -500 fs before optical excitation.Two non dispersive bands, traced by white dashed lines, are identified and attributed to the Sm 4f-states multiplets ${}^6H_{5/2}$ and ${}^6H_{7/2}$ at binding energy ~ 0.035 eV and ~ 0.180 eV, respectively. These flat states intersect a highly dispersive band derived from the Sm d-orbitals indicated by a dashed green line, crossing E_F at $\mathrm{k_F} \sim 0.35$ Å^{-1}. The intensity of this state is found to be highly suppressed in s-polarization, in agreement with the literature [100, 82]. The momentum distribution curve (MDC) integrated in the energy window $\mathrm{E} - \mathrm{E_F} = 10 \pm 10$ meV (inset of Fig. 6.2 (a)) shows the d-state peak, whose width is comparable with synchrotron based measurements performed at higher photon energy (30-70 eV). The dispersion of the d-band resembles the results obtained for $\mathrm{k_z}$ far from the bulk high symmetry directions [100]. This is in agreement with our estimated $\mathrm{k_z} \sim 2.7\pi/\mathrm{a}$.

Figure 6.2 (b) shows the modification of the electronic properties after optical excitation, for the highest absorbed energy density, resulting from the difference between the ARPES data 300 fs after and 500 fs before the arrival of the optical excitation. The color scale indicates with red (blue) the positive (negative) signal variation. The first noticeable feature, that characterizes the out-of-equilibrium electronic properties of $\mathrm{SmB_6}$, is the different response of the two sets of bands to the optical excitation. A depletion of intensity (blue) is visible in the two non dispersive f-states, whereas it is not observed along the dispersive d-band. We ascribe this effect to the higher density of states (DOS) of the f-state, which seems to dominate the optical absorption process.

Since the experiments are performed at $\mathrm{T} > \mathrm{T_K}$ and E_F is crossed by the dispersive d-band, we expect the material response to the optical excitation to be metallic. Hence, at short timescale immediately after optical excitation, electrons thermalize due to electron-electron scattering and relax towards $\mathrm{E_F}$ where their distribution is described by a time dependent FD function [14, 12, 28]. This process is assumed to occur within the pump pulse duration [37]. Figure 6.2 (b) shows that, after thermalization, electrons occupy a broad momentum region above $\mathrm{E_F}$, thus

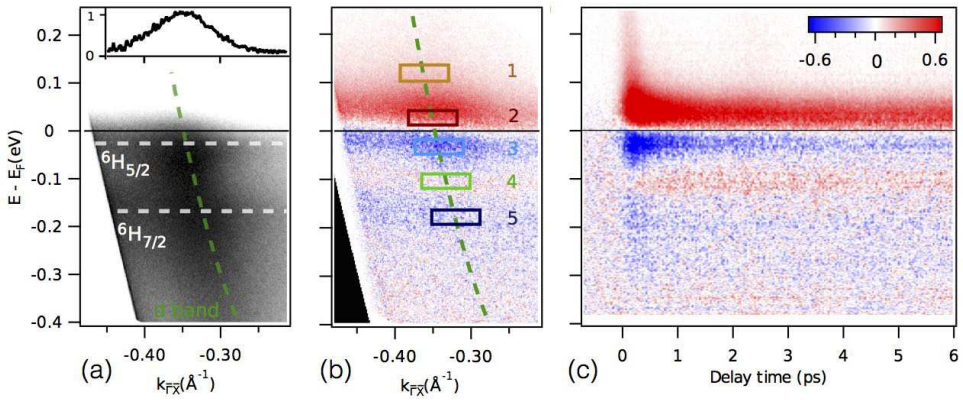

Figure 6.2: (a) Electronic properties measured at 120 K, 500 fs before optical excitation. Three spectral features are present, two non dispersive Sm f-bands and a dispersive d-derived state, whose momentum distribution curve at E_F is shown in the inset. (b) Difference between the out-of-equilibrium electronic properties 300 fs after and 500 fs before optical excitation. Depletion of intensity (blue) is revealed only in the f-state, and not in the d-band. (c) Temporal evolution of the change in intensity along the d band dispersion, green dashed line in (d).

suggesting the possible existence of unoccupied non-dispersing f-like states above E_F [112].

6.3 Electronic Temperature and Electron-Phonon Coupling Constant

Aim of our work is to evaluate the electron-phonon coupling constant from the temporal evolution of T_e, thus in the following we will focus only on the out-of-equilibrium dynamics of the time-dependent effective FD distribution, without entering in the details of the dispersion of the unoccupied states. In order to estimate the timescale over which the electronic temperature relaxes, we now turn our attention to the temporal evolution of the ARPES signal.

Figure 6.2 (c) shows the temporal evolution of the change in photoemission intensity integrated along the dashed green line in fig. 6.2 (a). In order to quantitatively describe the characteristic relaxation times, traces are extracted from fig. 6.2 (b) in representative regions of the band structure, within the energies indicated by the colored rectangles. Figure 6.3 (a) displays

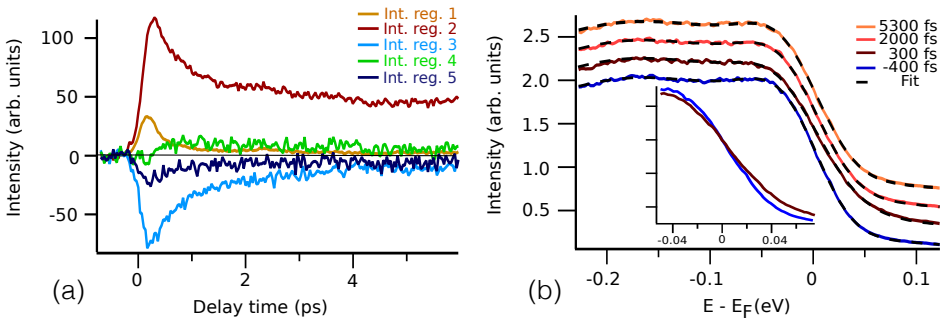

Figure 6.3: (a) Non-equilibrium dynamics as obtained by integrating the recorded intensity within selected energy regions along the d-band dispersion. The color code is the same of the rectangles shown in Fig. 6.2 (b). Regions 2 and 3, located symmetrically around E_F, display a similar characteristic timescale. Region 4, between the f states, is characterized by a small positive and delayed dynamics, different with respect to the negative dynamics of the f-states in regions 3 and 5. (b) Energy distribution curves along the d band dispersion at selected delay times before (-400 fs) and after (+300, +2000, +5300 fs) optical excitation. Black dashed lines indicate the best fit. The inset shows a zoom at E_F of the EDCs at -400 and +300 fs.

the resulting traces.

Region 1 (orange), at $E - E_F \sim 0.125$ eV, is characterized by a peak whose relaxation dynamics is comparable to our experimental temporal resolution. This prevents us from accessing the fast electronic dynamics responsible for the thermalization process. At energies closer to E_F the dynamics slows down, as expected in a thermalized electron system [12, 65]. The intensity relaxes to a plateau value larger than the equilibrium one. The full relaxation of the excited population is obtained through a second relaxation channel, having a timescale exceeding that achievable by the present experiment.

From a single exponential fit to the traces, we observe that the relaxation dynamics in proximity of E_F has the same characteristic time $\tau = 800$ fs $\pm$ 50 fs both above (region 2, brown) and below (region 3, light blue) E_F. This points to the fact that the dynamics is dominated by the thermal broadening of the FD distribution. The positive dynamics of region 4 (green), between the f-multiplets, is delayed and we ascribe this finding to a thermal broadening of the f-states, rather than a purely electronic effect. This point will be clarified later within the frame of the 2TM.

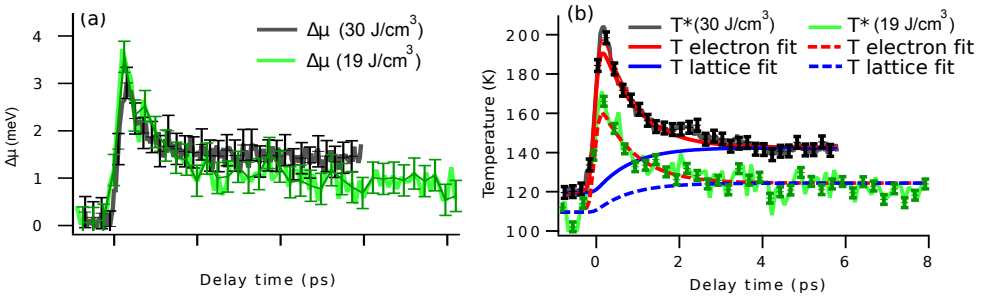

Figure 6.4: Temporal evolution of the chemical potential shift $\Delta\mu$ (a) and of the electronic temperature T_e (b), as obtained from the fit of the EDCs extracted from Figure 1(e). The results for two excitation energy densities are shown, equal to $\sim 30 \pm 6$ J/cm^3 (black) and $\sim 19 \pm 4$ J/cm^3 (green). Both $\Delta\mu$ and T_e relax after optical excitation with a single exponential behaviour, with characteristic time $\tau = 800$ fs $\pm$ 50 fs. The evolution of T_e is modelled within a 2TM, and the best fit is shown in panel (b). Red and blue lines indicate the dynamics of the electron and lattice temperature, respectively.

In order to evaluate the evolution of the electronic temperature T_e, as well as of the chemical potential shift $\Delta\mu$, we fit a time-dependent FD function to the energy distribution curves (EDCs) extracted from fig. 6.2 (e) for all the delay times. Figure 6.3 (b) shows selected EDCs at -400, +300, +2000, +5300 fs, vertically offset for clarity, along with the corresponding fits (black dashed lines). The broadening of the FD distribution is more clearly visible in the inset, which shows a zoom at E_F of the two EDCs at -400 and +300 fs. The fitting function results from the convolution of a Gaussian function, accounting for the experimental energy resolution, with the result of the product of a time dependent FD distribution and a function describing the density of states [11]. In the present study, the latter is the sum of two Lorentzian components for the f-multiplets in the occupied density of states, at -0.18 eV and -0.035 eV, and a constant accounting for the DOS of the d-band.

In performing the fit of the experimental EDCs, we only let T_e and $\Delta\mu$ vary with time. The reason for letting free only two fitting parameters is phenomenological: the parameters in the density-of-state function, when allowed to vary, do not produce an improvement of the χ^2 of the fit.

Figure 6.4 (a) and (b) show the dynamics of $\Delta\mu$ and T_e, respectively. Results are reported for both the two data sets, with excitation energy densities equal to 30 ± 6 J/cm^3 (black) and 19 ± 4 J/cm^3 (green).

After optical excitation, both $\Delta\mu$ and $\mathrm{T_e}$ relax with a single exponential behaviour, with characteristic time $\tau = 800\ \mathrm{fs} \pm 50\ \mathrm{fs}$. The values of $\Delta\mu$ are small but comparable with the previous work of Ishida *et al.* [101]. However, we point out that in the present study we are not sensitive to surface photo-voltage effect which is expected to slow the $\Delta\mu$ relaxation dynamics for $\mathrm{T} < \mathrm{T_K}$ [101]. The fact that the relaxation of $\mathrm{T_e}$ is well mimicked by a single decaying exponential justifies the choice of a 2TM for extracting λ. The evolution of the electron and lattice temperatures ($\mathrm{T_l}$) is described by the following rate equations, [39, 28] as previously reported in chapter 3:

$$\frac{\partial T_e}{\partial t} = \frac{S(t)}{C_e} - \frac{3\lambda\Omega^3(n_e - n_l)}{\hbar\pi k_b^2 T_e} \tag{6.1}$$

$$\frac{\partial T_l}{\partial t} = \frac{C_e}{C_l}\frac{3\lambda\Omega^3(n_e - n_l)}{\hbar\pi k_b^2 T_e} \tag{6.2}$$

$S(t)$ describes the optical excitation with gaussian profile and absorbed energy density equal to $\sim 30 \pm 6$ J/cm^3 and $\sim 19 \pm 4$ J/cm^3, respectively. $\mathrm{k_b}$ is the Boltzmann constant and n_e and n_l are the Bose-Einstein (BE) distribution functions for phonons calculated at temperature $\mathrm{T_e}$ and $\mathrm{T_l}$, respectively. The error bar associated to the energy density propagates into an error bar on the free fitting parameters in the 2TM, including λ. Ω corresponds to the phonon frequency. From optics, neutron scattering and symmetry analysis we expect only phonon modes at 10 meV (acoustic) [108, 109], $19 - 20$ meV [110, 109] ($\mathrm{T_{1u}}$), and three higher energies vibrational and rotational modes of the $\mathrm{B_6}$ cage at 89.6 meV ($\mathrm{T_{2g}}$) and 141.7 meV ($\mathrm{E_g}$) and 158.3 meV ($\mathrm{A_{1g}}$) [108].

In fig. 6.5 (a-b) the $\mathrm{SmB_6}$ phonon dispersion curve obtained from inelastic neutron scattering [108] and Raman spectra [109] are reported. In the Eliashberg formalism, λ results from the coupling of all the phonon modes, where the contribution from each mode is divided by its phonon energy. For this reason we expect the contribution of the high energy $\mathrm{B_6}$ modes to λ to be weak. This hypothesis is well supported by analogy with the calculations performed on a similar compound, $\mathrm{YB_6}$, which show that the electron-phonon coupling constant λ is dominated by the low energy Y phonon modes, while the high energy phonons associated to the $\mathrm{B_6}$ modes only weakly contribute to λ [99].

For these reasons, we have performed our analysis by considering the coupling to the low energy Sm modes at 10 meV [108, 109] and 19 meV [110] - 20 meV [109], respectively. In the

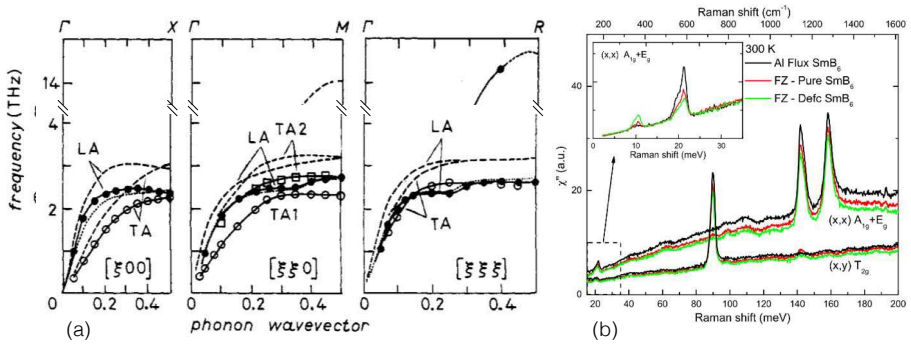

Figure 6.5: (a) SmB_6 phonon dispersion curves from inelastic neutron scattering in the range between 2 and 3 THz (8.3-12.4 meV). Dashed lines indicate the phonon branches for LaB_6 [108]. (b) Raman spectra show 3 active high energy Raman phonons and 2 low energy peaks (shown in the inset). [109]

model we assumed a particular form for the electron-phonon coupling, i.e. $\alpha^2 F(\omega) \propto \delta(\omega - \Omega)$, but no approximations are applied to the BE statistics. This is because the measured electronic temperature is not high enough to justify the commonly used "high-temperature" approximation of the BE statistics [83].

The lattice specific heat, C_l, for lattice base temperature of 120 K (110 K for 19 ± 4 J/cm^3) is taken from reference [111], while the electronic specific heat is $C_e = \gamma T_e$, with γ left free to vary as well as λ. The best fit to T_e is shown by continuous and dashed red lines in Figure 6.4 (b), for the two excitation energy densities, respectively, whereas blue lines indicate the dynamics of T_l. The electronic and lattice temperatures equilibrate after approximately 2 ps, and T_l is expected to recover its equilibrium value through lattice heat diffusion on a timescale longer than the temporal window of our measurements [28].

The 2TM reproduces well the evolution of T_e thus indicating that additional mechanisms, such as electronic heat diffusion, do not need to be taken into account for the case of the bad metal SmB_6, in contrast to case of conventional metals like Ru(001) [72] and Gd(0001) [73]. The increase in T_l accounts for the long lasting plateau observed in the dynamics across E_F in regions 2 and 3 in fig. 6.2 (b). The increase in T_l is delayed with respect to the optical excitation, as it turns out from the 2TM. This suggests a possible interpretation for the positive dynamics of (see 6.4 (a)) recorded in region 4 of 6.3 (b), whose maximum is reached at a later time than that of the other regions, as a consequence of thermal broadening of the f-multiplets due to the larger T_l. From the model we estimate a value of γ equal to $5.8 \pm 1.5\,\mathrm{mJ/molK^2}$, in good agreement

with the literature, where values of $7\,\mathrm{mJ/molK^2}$ [116] and $2\,\mathrm{mJ/molK^2}$ [117] are found.

The most important result of our analysis is quantitative evaluation of the electron-phonon coupling constant. From the 2TM, by considering the coupling dominated by the low energy Sm phonons, either with $\Omega = 10\,\mathrm{meV}$ [108, 109] or $\Omega = 19\,\mathrm{meV}$ [110] -20 meV [109], we obtain a value of $\lambda\Omega^3$ equal to 130 ± 30 meV^3 or 270 ± 70 meV^3, respectively. From $\lambda\Omega^3$ we extract two extreme values for λ equal to 0.13 ± 0.03 and 0.04 ± 0.01.

We can conclude that, for a realistic value of the average phonon energy between 10 meV and 19-20 meV, depending on the phonon density of states, λ will lie between 0.13 ± 0.03 and 0.04 ± 0.01. Unfortunately, no theoretical or experimental estimations of λ are available for $\mathrm{SmB_6}$ in the literature. From a comparison with different hexaborides, we note that the range in which λ falls for $\mathrm{SmB_6}$ is slightly lower than those reported for $\mathrm{LaB_6}$ ($\lambda = 0.17 - 0.26$ [118]), $\mathrm{MgB_6}$ ($\lambda = 0.39$ [119]) $\mathrm{YB_6}$ ($\lambda = 0.86$ [120]).

6.4 Conclusion

Our estimation of λ provides an insight in a fundamental physical property of $\mathrm{SmB_6}$. The slightly smaller value, compared to other hexaborides, might reflect an intrinsic difference in the electron-phonon coupling. Nonetheless, it might also be ascribed to the fact that tr-ARPES is momentum selective. We point out that the λ value is evaluated along the $\overline{\Gamma X}$ high symmetry direction, and far from the zone boundary, owing to the small momentum window accessible with the available photon energy. We believe that our results represent a reference for future momentum integrated measurements of λ, that might extend further the comparison between the electron-phonon coupling in different hexaboride compounds.

In conclusion, we have exploited tr-ARPES to investigate the out-of-equilibrium electronic properties of $\mathrm{SmB_6}$. After optical excitation, electrons are transferred predominantly from the localized f-multiplets to the unoccupied density of states. After thermalization, electrons can be described by a time-dependent Fermi Dirac distribution. The temporal evolution of the electronic temperature is described within a two temperature model. The phonon density of states is unknown for $\mathrm{SmB_6}$, hence we can only establish a range of values for λ. Indeed, a precise determination of lambda would require to exactly weight the contribution of both phonon modes

with their density of states. By assuming that the electron-phonon coupling, along the $\overline{\Gamma X}$ direction of the surface BZ, is preferentially mediated by the two lowest energy Sm modes at 10 meV [108, 109] or 19 meV [110] - 20 meV [109], we estimate λ to fall in the range 0.13 ± 0.03 - 0.04 ± 0.01.

Chapter 7

Linear dichroic signal in the ARPES study of $GeBi_2Te_4$ TI

In this chapter we report on the photon-energy dependent synchrotron-based investigation we have performed on the septuple layers (SL) topological insulator $GeBi_2Te_4$ by means of Linear-Dichroic Angle resolved Photoelectron Spectroscopies (LD-ARPES). From the observation of a linear dichroic signal both in the valence band states and in the topologically protected surface state we propose to interpret our LD ARPES as a probe of the symmetry related to the orbital character of the bulk valence band (VB). The observation of a change in the LD ARPES signal at the top of VB is attributed to the band parity inversion which is predicted by theory for all materials entering the topologically protected phase. By varying the photon energy we observed a different dichroic response of bulk valence bands with respect to previous results obtained on quintuple-layers TIs. Finally, the opening of a peculiar gap in the surface state dispersion has been observed, along non-high symmetry directions. This results from the interaction between the surface state and the VB, leading to the formation of surface resonances.

7.1 Introduction

The analysis of the dichroic signal in ARPES has recently proved the capability to add, in an indirect way, several important informations to the simple band mapping. While Circular dichroic ARPES (CD-ARPES) is deeply related to the material spin texture [11, 121], the orbital charac-

ter of the band structure can be evaluated from the linear dichroic ARPES (LD-ARPES) signal, as recently shown for the case of Bi_2Se_3 [78]. Even though, it is well known that final state effects must be adequately taken into account [12, 121, 122], as well as interference from the layer structure [78]. The LD-ARPES capability to indirectly probe the orbitals parity is of paramount importance when this technique is applied to materials as the TIs. The key mechanism which leads to the formation of the TSS relies, indeed, on the band parity inversion between CB and VB, which is a consequence of the large spin orbit coupling (SOC) of the atoms in the compounds. This fundamental concept at the base of the topological phase formation has not been subject of study, so far.

Motivated by previous studies, our work is aimed at investigating the inverted orbital ordering between the VB and CB states at the edge of the TI bulk band gap. In order to do so, we have carried out a photon energy dependent LD-ARPES study of the septuple layer TI $GeBi_2Te_4$ [115]. We start by showing the main features of the $GeBi_2Te_4$ band structure, where the TSS dispersion is well separated and clearly recognizable from the bulk VB states. Successively the results of our photon energy dependent linear dichroism investigation on the bulk valence bands are presented. Finally we report on the TSS and VB, which will be discusses in terms of a hybridization resulting in the formation of surface resonances.

7.2 Experiment

We have investigated high quality $GeBi_2Te_4$ single crystals grown by transport method. According to the position of the Fermi level, E_F, which lies within the bulk band gap, we can classify this compound as an intrinsic TI. The crystal structure is composed by seven-layer (7L) blocks formed by the sequence Te-Bi-Te-Ge-Te-Bi-Te, as shown in Fig.7.1 panel (a). The 7L blocks are bounded by van der Waals forces, thus offering a natural cleavage plane for this system. The hexagonal surface Brillouin zone is reported in Fig.7.1 (b), along with the investigated directions. Besides the $\overline{\Gamma K}$ and $\overline{\Gamma M}$ high symmetry direction, we indicate the investigated non high-symmetry directions along with we measured as $\overline{\Gamma Q}$ (green) and $\overline{\Gamma Q'}$ (violet), respectively.

ARPES experiments have been carried out, in this case, at the BaDELPh beamline[123] at the Elettra Synchrotron, in Trieste. Samples are measured, after being cleaved, in ultra high vacuum (10^{-11} mbar) at 80 K. We have used linear polarized synchrotron light (σ and π polar-

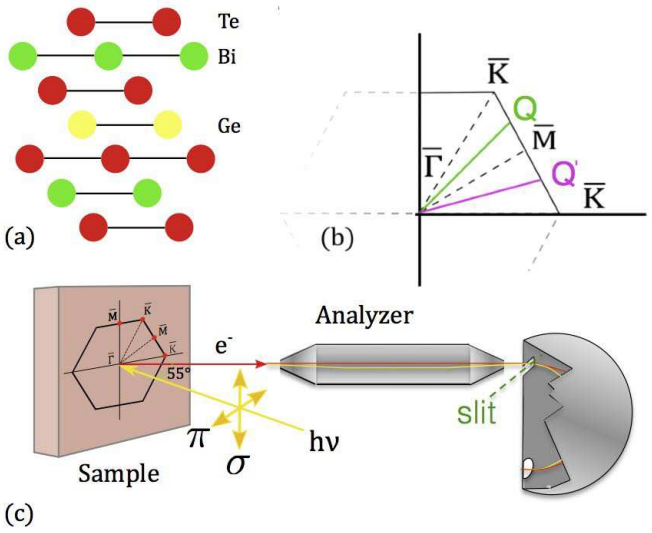

Figure 7.1: (a) Schematic of the seven-layer building blocks structure of the $GeBi_2Te_4$ crystal. (b) Portion of the hexagonal Surface Brillouin zone (SBZ) showing all the directions investigated in our study. Non-high symmetry directions $\overline{\Gamma Q}$ (green) and $\overline{\Gamma Q'}$ (violet) are located in between $\overline{\Gamma K}$ and $\overline{\Gamma M}$ respectively. (c) Experimental geometry for ARPES measurements. The analyzer slit is parallel to the scattering plane, as indicated.

ization), in the energy range 14-28 eV. A sketch of the setup geometry is shown in Fig.7.1 (c). The angle between the UV light direction and sample surface is $55°$. These directions form the scattering plane, which contains also the analyzer slit direction. In this particular acquisition geometry the π polarization is even and the σ-polarization is odd. As a result, the former has access purely to even states and the latter purely to odd states.

7.3 Electronic band structure

Figures 7.2(a) and 7.2(b) show the band structure of $GeBi_2Te_4$ measured along $\overline{\Gamma K}$ and $\overline{\Gamma M}$ high-symmetry directions, respectively. We have selected 14 eV photon energy and linear π-polarization. Panel (c) schematizes the prominent spectral features experimentally resolved in our study. We report the presence of a linearly dispersing state, crossing the Fermi level with k_F = 0.15 Å^{-1}, thus supporting the TI nature of $GeBi_2Te_4$, in good agreement with similar recent observation [124, 115]. No bulk conduction bands are present at the E_F, making surface state

more visible. In addition, figure 7.2 panel (c) allows to clearly distinguish it. In the sample investigated in our study the Dirac point is located ~ 120 meV below the Fermi level, similarly to ref. [125]. However, the position in energy of the Dirac point may differ because of different doping resulting from different growth technique [124, 126].

Approximately 0.5 eV below the Fermi level, we resolve several states dispersing with hole-like character and constituting the bulk VB. The VB dispersion is clearly sketched in fig.7.2(c) with blue and teal colour, along with the dispersion of the TSS in orange.

Below surface derived state we observe a complex scenario; many "M-type" shape bands intersect each other. We resolve two couples of states, that appear split in momentum, probably as a consequence of the large atomic spin orbit coupling. These findings are in agreement with the results of similar studies [124] and [125]. We do not notice relevant differences between bands shown in panel (a) and (b), apart a small region located at $\overline{\Gamma}$ and ~ -0.25 eV below the Dirac point. The TSS measured along the $\overline{\Gamma K}$ (7.2(a)) presents a non vanishing spectral weight below the Dirac point. We suggest, that valence bands may overlap surface states, in analogy to the similar scenario observed in ref. [125].

It is well known that in TIs the formation of topologically protected surface states relies on the inversion of the band ordering at the time reversal invariant points [59]. Most of the TI compounds show a negative band gap at the Γ point. As a consequence of the large atomic SOC, the direct gap is closed and re-opened with a hybridization between the conduction and valence band states. This results in a change of the parities of the states forming the gap.

In the prototypical case of Bi_2Se_3 the state with odd parity is pushed down at energy lower the one with even parity. The scenario of the evolution of the band structure from a trivial insulators into a TIs is sketched in figure 7.3 panel (a). In this cartoon we sketch the most general case in which the conduction and valence band have different character. We indicate that with the letter α (red) and β (blue). We adopt the same red-blue colour scale for our data to show π and σ contribution. The panel (c) summarizes the data of Fig. 7.3 panes (e-h) in a sketch view.

Armed with the will to experimentally evidence this scenario, we have performed LD-ARPES measurements along $\overline{\Gamma K}$ and $\overline{\Gamma M}$ directions. In order to resolve and parity of the several spectral features in the band structure we probed them with π and σ polarized light (see fig. 7.1 (c)). For each direction we evaluate the differential image, obtained as difference

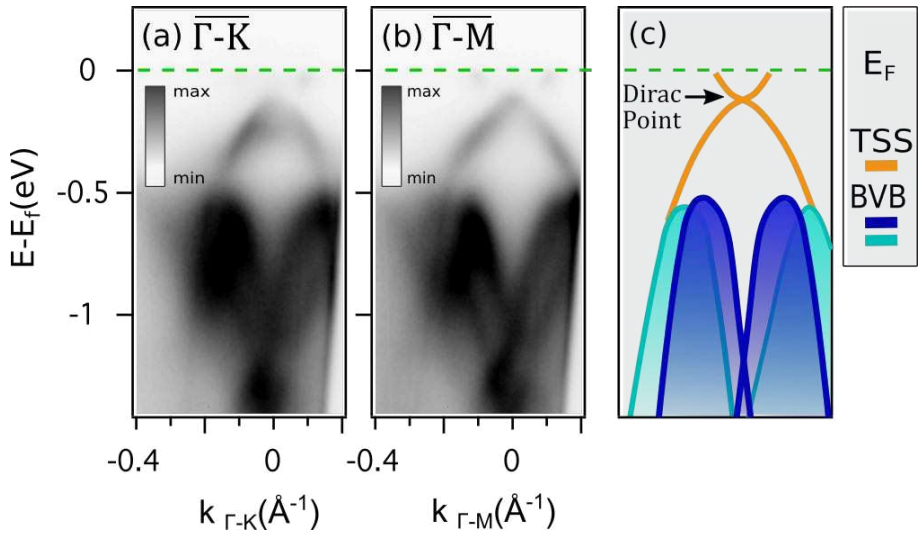

Figure 7.2: (a-b) ARPES images of the TI $GeBi_2Te_4$ measured with 14 eV π and polarized photon along $\overline{\Gamma K}$ and $\overline{\Gamma M}$ high-symmetry directions. The Fermi level is indicated by a green dashed line, the Dirac Point is marked by a black arrow. Sketch of surface-and bulk-derived bands shown in panel (a) and (b),TSS is indicated an by orange line and BVBs are indicated by blue filled lines.

between the data set with π and σ polarization. The differential images enable the reader to appreciate the different band character and symmetry of the states,as will be later discussed.

Figure 7.3 shows measurements performed with π and σ polarization and the dichroism ($\pi - \sigma$) image along $\overline{\Gamma K}$ (c-e) and $\overline{\Gamma M}$ (f-h). The maximum of the VB in fig. 7.3 shows a M-like shape, typical of a wide set of TIs [115, 127, 53] and resulting from the negative band gap opening. The dichroic signal of fig. 7.3 (e) and (h) show a change in colour, i.e. parity, at the Γ point. Figure 7.3 (b) synthetizes the dichroic signal results. We notice that the measured dichroic signal is in good agreement with the expected scenario of fig. 7.3 (b) and with the simplified cartoon (a). Therefore, we propose to interpret the dichroic signal as a direct experimental evidence of band inversion which characterizes the TI phase [128].Finally the SS is also visible in the differential image, with mainly odd parity (red signal).

The ARPES data shown in Fig 7.3 have been acquired with a photon energy of 22 eV, however it is well known that the dichroic signal in ARPES can be severely affected by final state effect [121]. For this reason we have carried out a systematic investigation of the dichroic

signal for different photon energy, as it will be discussed here below.
In Figure 7.4 panels (a-d) we report the polarization dependent band structure as measured for four different photon energy in the range of 16 eV to 22 eV. We show the data acquired 0.4 eV below the Fermi level at the $\overline{\Gamma}$ point, in the region of the M-shape where the inverted gap is expected along with the change in the parity of the states.

We adopt the same colour code of figure 7.3. Even though we might expect the linear dichroism to show a large change in intensity and in sign as a function of the photon energy, as a consequence of final state effect (ref [121, 129]), we notice that the top part of the VB, at the M-shape, shows mainly odd parity, which is conserved in the investigated photon energies range. Whereas, band locate at larger k-values show consistently a greater even-contribution, independent on the photon energy.

7.4 Bulk and Surface State Hybridization and Surface Resonance Formation

We compare now the ARPES maps acquired along the four different directions in the SBZ represented in Fig. 7.1. We can immediately notice an interesting effect along the dispersion of the topological surface state. Figure 7.5 reports the maps acquired at 14 eV photon energy and π polarization. Panels (b) and (d) report measurements along $\overline{\Gamma Q}$ and $\overline{\Gamma Q'}$, while panels (a) and (c) show the $\overline{\Gamma K}$ and $\overline{\Gamma M}$ high symmetry directions, respectively.

The bulk states forming the M-shaped VB around the $\overline{\Gamma}$ point do not show appreciable differences for the four measured directions. Similarly, the upper part of the Dirac cone disperses across E_F with very little dependence on the particular in-plane direction. By focusing on the touching point between BVB and the the bottom part of the TSS, at -0.2 Å, we resolve a change in the TSS dispersion when probed along a non-high symmetry direction.

Fig.7.5 (b) reports clearly that the left side of the TSS bends, deviating from the Dirac cone. This change in dispersion is accompanied by a reduction in spectral weight, which we attempt to interpret as a hybridization effect between VB and CB. An additional state with weak intensity disperses in this novel band gap, with a band velocity which closely resembles the the TSS one.

We propose that this additional state might be a surface resonance of the bulk states at the surface, as a consequence of the partial hybridization between VB and TSS. Calculation are

needed to better describe the nature of this gap and to infer about the possible mechanisms responsible for the hybridization between surface and bulk states, and the subsequent formation of the surface resonance [65, 78, 130, 131].

7.5 Conclusion

In summary we have performed linear-dichroic ARPES photon-energy dependent investigation of $GeBi_2Te_4$ TI, with the aim to directly evidence the inversion of parity in the states forming the bulk gap. We have focus in particular on the energy region of the bulk band gap where the topologically protected surface state disperse across the Fermi level. We have investigated the maximum of the BVB state, in the region characterized by the M-shape dispersion typical of the inverted band gap.

The VB states are characterized by a peculiar change in the dichroic signal, in the M-shape region. We propose to interpret this effect as change in the orbital ordering, as a consequence of the inverted band gap, characteristic of the topological phase. The overall dichroic signal does not exhibit a clear photon-energy dependence, this suggests that, if final state effects are at play, their contribution to the linear dichroic signal is small.

Topological surface state shows deviation from linear dispersion, accompanied by a large reduction in spectral weight, when probed along non high symmetry direction. We propose to interpret this as signature of an hybridization gap with the BVB states. Residual spectral weight within the hybridization gap indicates the formation of surface resonances, as similarly reported in other TIs. This might indicate that the coupling between TSS and surface resonances is general to all TIs.

Our experimental work would certainly benefit by a benchmark with ab-initio photoemission calculation. Calculated matrix elements would provide important informations about the orbitals parities supporting the dichroic ARPES measurements. Moreover, final states effects should be considered and included in simulations, in order to better comprehend the formation of the surface resonance.

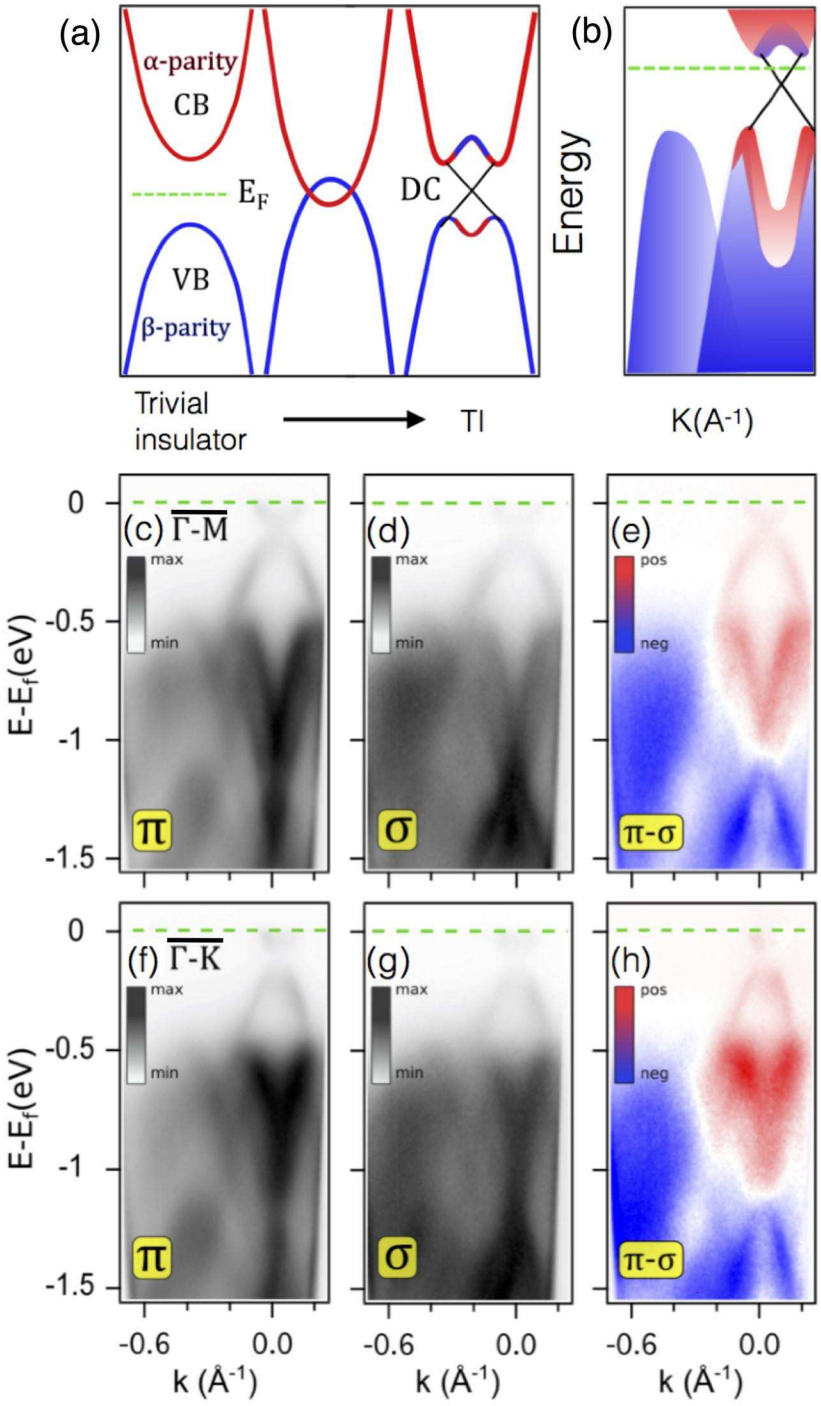

Figure 7.3: (a) Sketch of the band parity inversion, red and blue colours represent α and β-like states respectively. Panel (b) Panels (c-d) and (f-g): LD-ARPES measurements along high symmetry directions $\overline{\Gamma M}$ and $\overline{\Gamma K}$ performed with 22 eV photon energy, (e-h) corresponding dichroic signal. The Fermi level is indicated by a green dashed line.

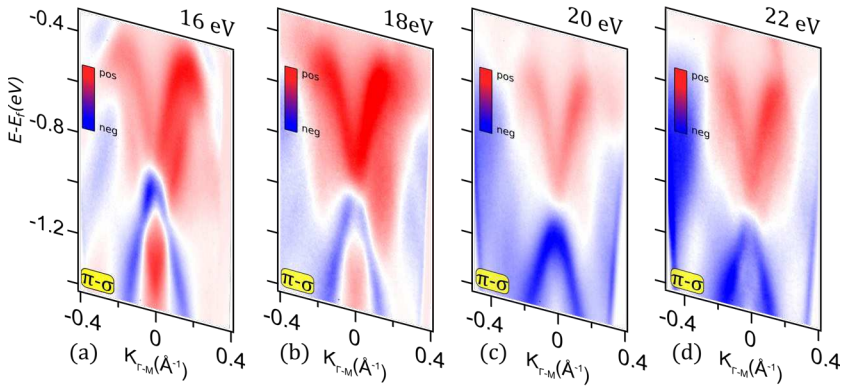

Figure 7.4: Linear dichroic ARPES measurements along $\overline{\Gamma M}$, performed with π and σ polarization. Panels (a-b-c-d) report 16, 18, 20, 22 eV photon energy respectively.

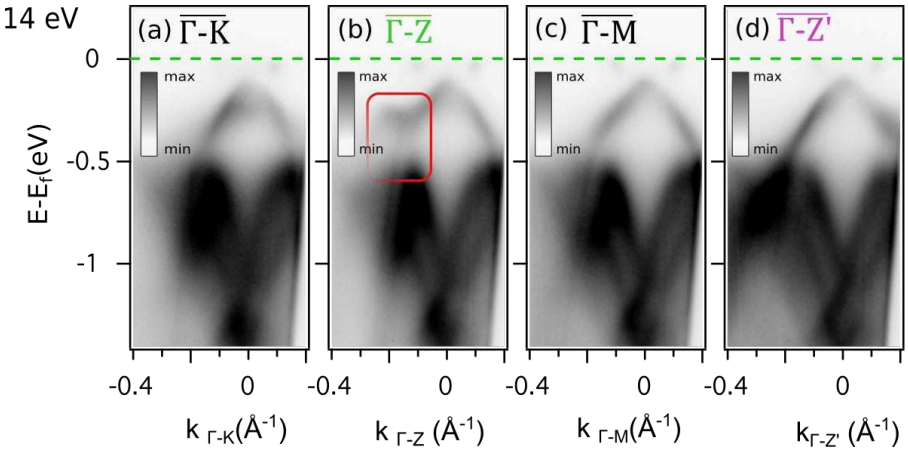

Figure 7.5: ARPES images along $\overline{\Gamma K}$ (a) and $\overline{\Gamma M}$ (c) high-symmetry direction and within $\overline{\Gamma Q}$ (b) and $\overline{\Gamma Q'}$ (d). The Fermi level is indicated by a green dashed line, the red rectangle indicates the possible TSS hybridization.

Chapter 8

Weyl Semimetals

This chapter deals with the new intriguing class of Weyls semimetals (WSMs). In the first part, after a brief introduction to the physics of WSMs, we review the ARPES studies which have reported the observation of the first type-I WSM, TaAs. In the following section, the type-II WSMs are introduced. The second half of the chapter is devoted to our recent experimental investigation of the type-II WSM candidate $MoTe_2$.

8.1 Introduction to Weyl Semimetals

Recently, topologically non-trivial materials have gained a spotlight in condensed matter, thanks to the discovery of a new class of material known as Weyl semimetals (WSMs). First examples of WSMs, have been theoretically predicted in the class of pyrochlore iridates by Wan et al. in 2011 [18]. Four years later, in 2015, an ARPES study of the electronic properties of TaAs has proposed this material as the first experimental observation of a WSM phase [19].

WSMs are materials characterized by either inversion or Time Reversal (TR)-symmetry. Evidences of the Weyl phase have been initially researched in magnetic materials, as pyrochlore iridates, where the TR-symmetry is broken. Successively, the investigation has moved to class of non-centrosymmetric systems. As topological insulators, WSMs are identified by topological invariants and they are characterized by a strong spin-orbit coupling. However, it is worth noticing that WSMs and TIs differs in many important aspects.

The band structure of Weyl materials presents a quite complex nature, both in the bulk and at

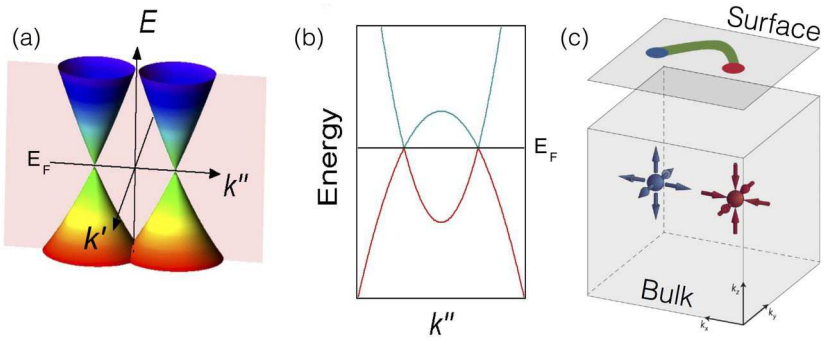

Figure 8.1: Representation of the energy-momentum dispersion of two Weyl cones in the k'-k" plane (a) and along k" direction (b). The most simple Weyl state showing a Fermi arc on the surface connecting the projections of two Weyl nodes with opposite chirality (c). Adapted from [133].

the surface. While TIs are bulk insulators, WSMs are gapless semimetals in which the valence and the conduction bands touch each other at special points, called Weyl points (WPs) or Weyl nodes [1] (WPs). Figure 8.1 (a,b) shows sketches of the Weyl nodes, the point of degeneracy of linear dispersing bulk states called Weyl cones. The Weyl cones and the Dirac cones at the surface of TIs are different. While Weyl cones present a linear dispersion in the 3D momentum space, surface Dirac particles exhibit a 2D linear dispersion. WPs can be founded at the Fermi level (as represented in fig. 8.1 (a,b)), for specific value of (k_x, k_y, k_z), due to the 3D dispersive nature of the bulk states. Furthermore, they are not located at high symmetry points, but only in their vicinity. They always appear in pairs with opposite chiralities and can be formally viewed as monopoles and anti-monopoles of the chiral charges in the momentum space [132].

WSMs present, as TIs, unique surface states whose properties are intimately connected to the dispersion of bulk states. In WSMs, the topological surface states form disjoint segments of 2D Fermi contours (Fermi arcs) which emerge and terminate onto the projections of the Weyl points at the surface BZ. In fig. 8.1 (c) the simplest WS state consisting of a Fermi arc and two Weyl points, is schematized.

The possible applications of Weyl fermions in novel transport devices have motivated several experimental and theoretical works. These have culminated in the observation of the so-called chiral anomaly resulting in a negative magnetoresistance when both the electric and magnetic

[1] These points are often called fermion nodes, since Weyl fermions are considered to rise as low energy excitation at Wely points in the momentum space.

field are applied parallel to the sample surface [19, 134]. Additionally to their unique transport properties, in the case of TaAs a superconductivity under pressure has been also reported [135, 136]. Fermi arcs have been object of intense studies because of their intriguing spin polarization textures. Moreover, they have been predicted to show unconventional quantum oscillations in magneto-transport and unusual quantum interference effects in tunnelling spectroscopy [137, 138].

8.1.1 The First Evidence of a Weyl Fermion Semimetal

Xu *et al.* have reported, in 2015, the discovery of the first WSM candidate by studying a TaAs single crystal, a semimetal that crystallizes in the non-centrosymmetric $I4_1md$ space group [19]. Electrical transport measurements have confirmed its semimetallic nature, along with a negative magnetoresistance, which have been interpreted in terms of Weyl fermions anomalies [19]. Calculations have predicted for TaAs a total number of 24 bulk Weyl nodes located at different k_z planes. These points, depending on their projections on the (001) surface BZ, have been divided in two sub-group due to their location, namely W1 and W2.

Xu *et al.* have performed a photoemission spectroscopy investigation of TaAs aimed at revealing the fingerprints of the WSM phase. By combining surface-sensitive ARPES and bulk-sensitive soft x-ray ARPES (SX-ARPES), they have observed some of the main features of the WSM phase, such as the Fermi arcs at the surface, the Weyl fermion cones and bulk Weyl nodes.

Figure 8.2 (a) shows an overview of the Femi surface at the (001) TaAs cleaving plane, as acquired by low-photon energy ARPES. In the vicinity of the mid-points of each $\bar{\Gamma} - \bar{X}$ or $\bar{\Gamma} - \bar{Y}$ lines, "lollipop" shapes with arcs state inside are observed. One of the criteria proposed to determine the topological nature of the arcs shown in fig. 8.2 (b), consists of observing how their constant-energy contour evolves as a function of the binging energy [139]. If the "lollipop" consisted of topological Fermi arcs, one orc should evolve with respect to the binding energy in a hole-like way, while the other should evolve in a electron like way [139]. Such as behaviour is visible in fig. 8.2 (c), by observing the dispersion of open-shape states extracted from cut 1 and cut 2 parallel to the $\bar{\Gamma} - \bar{X}$ and $\bar{\Gamma} - \bar{Y}$ lines. In fig. 8.2 (d) the observed energy-dependent behaviour of the Fermi arcs in the $k_x - k_y$ plane is sketched. Finally, as the authors have noticed, the different dispersion exhibited by the lollipop pockets arises from the non zero chiral charge

of the projected bulk nodes[2] [19]. Thus, the open contours of the arcs are supporting the Weyl nature of this material.

Surface states calculations have been carried out, revealing that Fermi arcs connect projected W2 Weyl nodes near the midpoint of each $\bar{\Gamma} - \bar{X}$ and $\bar{\Gamma} - \bar{Y}$ lines. Another set of Fermi arcs is predicted by the theory to disperse at the $\bar{X}$ point. However, due to the limited experimental resolution, it is not well resolved. The second part of the study carried out by Xu *et al.* presents the bulk band investigation performed by means of SX-ARPES. W2 Weyls points, in the 3D k-space have been fully mapped by varying the photon energy. The W2 points have been identified for specific photon energies corresponding to the $k_z = 0$ planes, and they are visible in the $k_x - k_y$ Fermi surface of fig. 8.3 (a).

Figure 8.3 (c,d) shows the energy-momentum maps as a function of k_y and k_z along the direction indicated by cut 1 and cut 2 in panel (b), respectively. In panel (c) two linearly dispersing cones are clearly visible. These correspond to the two W2 Weyl nodes, as indicated by arrows indicated in panel (b). The k_z out-of-plane dispersion, extracted at the k_x, k_y points indicated by black cross (cut 2) of panel (b), is shown in panel (d). The second pair of WPs (W1), which are not visible in fig. 8.3, are observed at a different k_z values and are associated to the second set of Fermi arcs previously mentioned.

As these authors have noticed, in general point-like linear band crossing in a bulk crystal with strong SOC, can either be Weyl cones or Dirac cones. However, cones in fig. 8.3 (c), are located neither at Kramers points nor on a rotational axis, hence they cannot be identified as bulk Dirac cones, so they have to be Weyl cones according to topological theories [19].

8.1.2 Type I and Type II Weyl Semimetals

After the discovery of the TaAs WSM, Soluyanov *et al.* have proposed the existence a new type of Weyl point, called type-II, which has been predicted through the generalization of the Dirac equation [4]. In the original work of Weyl, this particle has not been considered, since it is characterized by the breaking of the stringent Lorentz invariance [4]. However, as it has been pointed out in the work of Soluyanov *et al.*, this symmetry breaking in condensed matter physics is not forbidden, and it thus results in a new type of Weyl fermions emerging at the boundary between electron and hole pockets on the FS. Type II WSMs, which show physical properties

[2]The chiral charge carried by the Weyl nodes, and represented in fig. 8.2 (d), is $\pm$ 2.

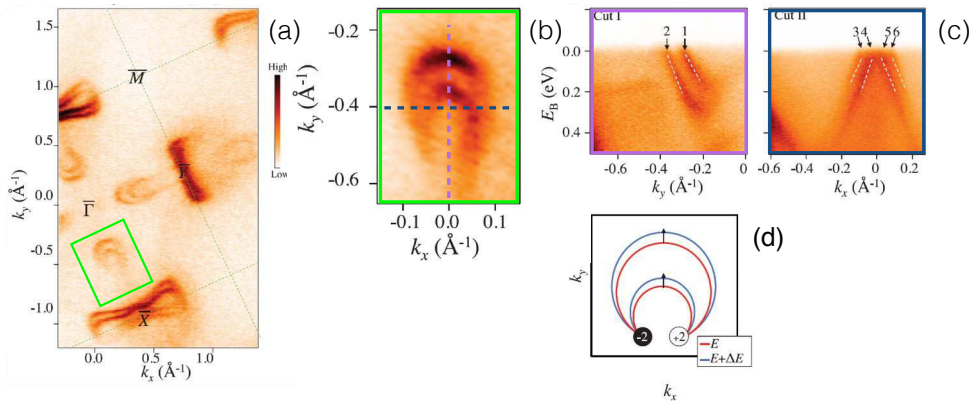

Figure 8.2: . (a) Fermi surface of the (001) surface of TaAs with high symmetry points of the SBZ indicated. The green rectangle marks the open-shape bands. (b) High resolution ARPES Fermi map of the "lollipop" shape containing Fermi arcs, marked by the green rectangle. (c) Energy dispersion maps along cuts I (violet) and II (blue), indicated on panel (b). A scheme showing the evolution of the Fermi arcs as a function of energy, distinguishing between two Fermi arcs and a closed contour (d). Adapted from [133].

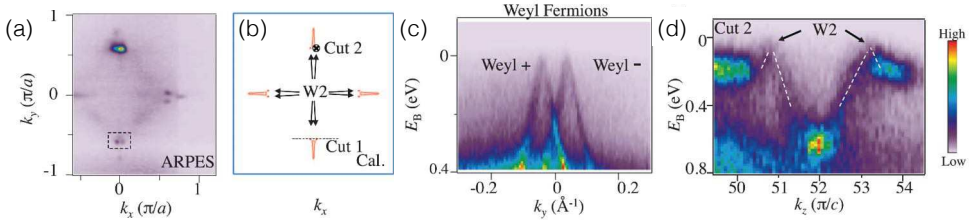

Figure 8.3: (a-b) Measured and first principles calculated $k_x - k_y$ Fermi surface maps at the k_z value that corresponds to the W2 Weyl nodes. The dotted line defines the k-space cut direction for cut 1, which goes through two nearby W2 Weyl nodes along the k_y direction. The black cross defines cut 2, which means that the k_x-k_y values are fixed at the location of a W2 Weyl node, whereas the k_z value varies. (c) ARPES $E - k_y$ dispersion map along the cut 1 direction, showing the two linearly dispersive W2 Weyl cones. (d) $E - k_z$ dispersion map along the cut 2 direction. Adapted from [133].

distinct from the type-I, have been suggested to lead to new intriguing possible applications.

Soluyanov and coworkers, have proposed a formal distinction between type I and type-II WPs based on the general hamiltonian which describes a WP. The energy spectrum derived

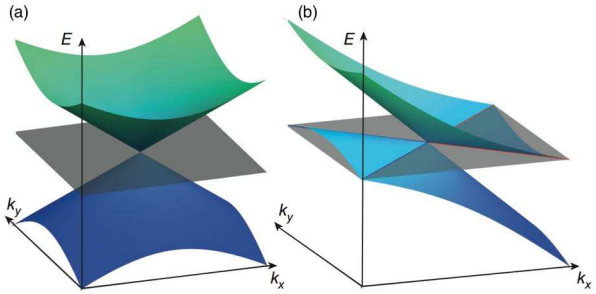

Figure 8.4: (a) Type-I WP with a point-like FS. (b) Type-II WP which appearing at the touching point between the electron and hole pockets. The grey plane represents the Fermi level, the blue (red) lines mark boundaries of hole (electron) pockets. Adapted from [4].

from the WP hamiltonian can be written as [4]:

$$\epsilon_{\pm}(\mathbf{k}) = \sum_{i=x,y,z} k_i A_{i0} \pm \sqrt{\sum_{j=x,y,z} \left(\sum_{j=x,y,z} k_i A_{ij} \right)^2} = T(\mathbf{k}) \pm U(\mathbf{k}) \tag{8.1}$$

where $T(\mathbf{k})$ and $U(\mathbf{k})$ represent the kinetic energy and the potential energy components, respectively. $A_{i,j}$ is a matrix of coefficients and $\mathbf{k}$ is the crystal momentum vector. Since the kinetic term $T(\mathbf{k})$ is linear in momentum, the resulting cone-like spectrum is tilted [4]. This tilt, which is responsible for the breaking of the Lorentz invariance of the Weyl fermions, leads to a finer double-classification of Fermi surfaces. As a consequence, two distinct types of WPs, namely type-I and type-II, are expected to appear at the touching points between electron and holes pockets, due to the "tilt effect".

Type-I and type-II WPs and two different Weyl cones are represented in fig. 8.4. Tilted Weyl cones can be observed for particular directions in the reciprocal space, where the kinetic $T(\mathbf{k})$ contribution dominates over the potential $U(\mathbf{k})$. A WP is considered type-II if along al least one k'- direction $T(k') > U(k')$.

Soluyanov and coworkers have identified in WTe_2 the first type-II WSM candidate. The authors have described, through band structure calculations, of the main features of WTe_2 bands considering and neglecting spin orbit coupling (SOC). Interestingly, they have noticed that SOC does not determine the presence of the WPs, but it affects their position in the reciprocal space. Then, they have determined the nature of the WPS, by analyzing their energy-spectrum. The kinetic component in proximity of these Weyl nodes is found to dominate, thus confirming the nature of type-II WPs. Moreover, calculations have suggested that the FS at the (001) surface

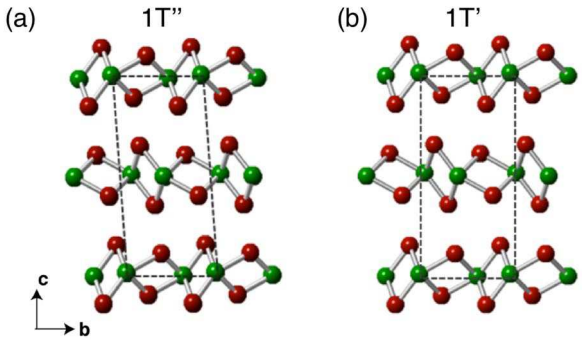

Figure 8.5: Crystal structure of $MoTe_2$ in the 1T” (a) trivial phase and 1T’(b) Weyl semimetal phase. Green and red atoms correspond to Mo e Te atoms respectively. Adapted from [141].

hosts a topological Fermi arc which connect projections of the electron and hole pockets. In the final part of their work another strong type-II WSM candidate is proposed, the transition metal dichalcogenide $MoTe_2$, that is treated more in details in the next section.

8.1.3 The $MoTe_2$ Type-II Weyl Semimetal candidate

A direct experimental confirmation of WTe_2 as type-II WSM, has been elusive, so far due to its bands structure features. Opposite WPs present a small momentum separation and detecting the Fermi arcs is challenging. Recently, $MoTe_2$ has been proposed to realize the type II WSM phase. This material seems to be promising, since the Fermi arcs are expected to be more extended and thus falling within the resolution of the present state-of-the-art ARPES experiments [21, 140, 141, 142, 143, 144, 145].

$MoTe_2$ presents the breaking of inversion symmetry, but only in the low temperature crystalline phases (1T’) while in the room temperature (1T”) phase type-II Weyl fermions are not predicted. In fact, that material at room temperature can crystallize in two phases: a semiconducting phase (2H) and a semimetallic 1T” phase. The semimetallic 1T” phase exhibits, at ~ 240 K, a structural transition to the so-called 1T’ phase. While the 1T” shows a monoclinic crystal cell the 1T’ phase, due to relative shift of Mo and Te layers, is orthorhombic. The two $MoTe_2$ crystal structures are shown in fig. 8.5.

A number of experimental investigations have been carried out to reveal the presence of type-II Weyl fermions in $MoTe_2$ [21, 140, 141, 142, 143, 144, 145]. These studies reported in the literature, have proposed different and partially conflicting interpretations of the topological

surface states of this material. However, a high-resolution ARPES investigation performed by Tamai *et al.*, has recently clarified this open question [21]. The experimental results are supported by a remarkable agreement with *ab-initio* calculations, which shows the simultaneous existence of both topological trivial surface state and Fermi arc. Being the dispersion of the former insensitive to variation of the crystal structure resulting in the change of the number of Weyl points from 4 to 8.

Tamai *et al.* have noticed that in $MoTe_2$ the broken of inversion symmetry which accompanies the 1T' structural phase, implies in fact the existence of two different possible (001) crystal surfaces terminations, denoted with A and B as indicated in fig. 8.6. The corresponding band structure, measured by synchrotron-based ARPES, is shown in fig. 8.7.

The FS, shown in fig. 8.7 (b), presents hole-like sheets centred at the Γ point and two electron-like pockets on the two sides. The prominent spectral feature is a arc-shaped state located in the gap between the electron- and hole-pockets, labelled in fig. 8.7 (b) with SS. Figure 8.7 (c) shows the k_z dispersion, revealing that SS is a two-dimensional state.

Figure 8.7 (d) reports the band structure measured along the k_y= 0 high-symmetry direction with an ARPES "zoom" in proximity of the SS state (blue inset) carried out by exploiting an ultra high-resolution laser-based ARPES setup. Thanks to the better resolution of the low photon energy setup, in the inset of fig. 8.7 (d) two sharp dispersing states are visible within the gap [21]. To better resolve the surface states located in the region marked by the red rectangle in fig. 8.7 (b), two high resolution FSs corresponding to the A and B terminations are presented in fig. 8.8. In the case of termination A, fig. 8.8 (a,c), in addition to the evident SS, a set of shorter arcs is visible. For surface B, shown in fig. 8.8 (b,d), the FS presents only one state, with a curvature closely resembling the one of SS. No additional shorter arc is present. Interestingly, according to the calculation, the SS surface state is topologically trivial, whereas the shorter arcs, labelled by CTSS in fig. 8.8 (a,b), are predicted to be topologically protected[3].

As these authors have noticed, only one of the two (001) surface terminations of $MoTe_2$ shows clearly the CTSS state. This fact is explained by asserting that a trivial value for the topological invariant Z_2 in compatible with two possible arc connectivities [21]. The CTSS state, which according to calculations can not be explained in a topologically trivial scenario, is regarded as a fingerprint of the type-II Weyl state.

[3] According to the calculated Cern number.

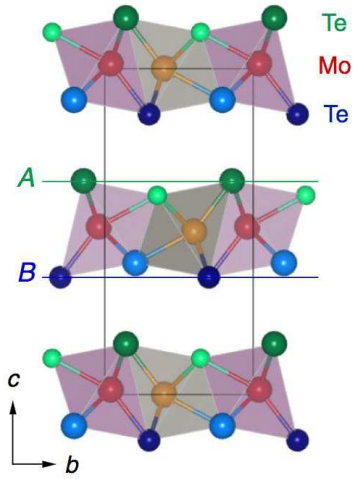

Figure 8.6: Crystal structure of $MoTe_2$ in the 1T' phase. The two inequivalent terminations are labeled with A and B Green and red atoms correspond to Mo e Te atoms respectively. Adapted from [141].

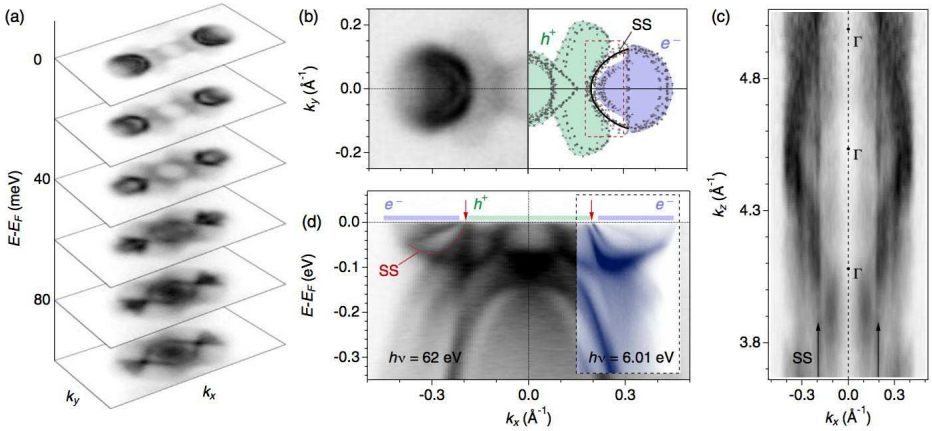

Figure 8.7: Band structure of $MoTe_2$. (a) Constant energy maps stacked. (b) Measured FS (left) and sketched FS (right). Blue and green indicate the maximum extension of electron and hole pockets corresponding to the projected bulk states, respectively. The thin black arc in between the two pockets, indicates the SS surface state. (c) k_z dispersion map at the Fermi level and in the k_y= 0 plane. (d) Overview of the band structure as measured along the k_y= 0 high-symmetry direction, at 62 eV and at low photon-energy (blue inset). Taken from [21].

In addition, the authors have compared the evolution of the Fermi arcs emerging from different simulated WPs arrangements. In particular, the surface DOS calculated in their work is compared with the crystal structure reported in [146]. While this structural configuration cor-

responds to 8 WPs, Wang *et al.* have predicted 4 WPs [146], starting from a slightly different crystal structure. Calculations have indicated that a spin-polarized Fermi arc is present for both WPs arrangements. However, the topological nature of the predicted Fermi arc is different. Whereas in the first case (8 WPs) the state is topological, in the latter (4 WPs) is predicted to be topologically trivial.

These findings indicate that the topological character of the Fermi arcs can not be uniquely determined from a qualitative comparison between of experimental and theoretical band dispersion. The determination of the spin structure can not fully prove the Weyl nature of surface states. As a matter of fact, bulk states of a non-centrosymmetrical material can be spin-polarized as the predicted SS state can be simultaneously spin-polarized and topologically trivial. As shown by Tamai et *et al.*, in order to clearly identify WSM states, high resolution experiments and systematic calculations to determinate the Cern number are needed.

The next part of this chapter is entirely devoted in to our ARPES investigation on $\mathrm{MoTe_2}$, performed in collaboration between the Laboratory of Photoelectron Spectroscopy (LSE) at EPFL (Lausanne) and the Time-Resolved X-Ray spectroscopy Laboratory (T-Rex) at Elettra in Trieste. Our work, is supported by *ab-initio* calculations carried out at the Swiss National Supercomputing Centre (CSCS). In order to better appreciate differences between the trivial and Weyl phase of this material, the ARPES study has been performed at different temperatures across the structural phase transition.

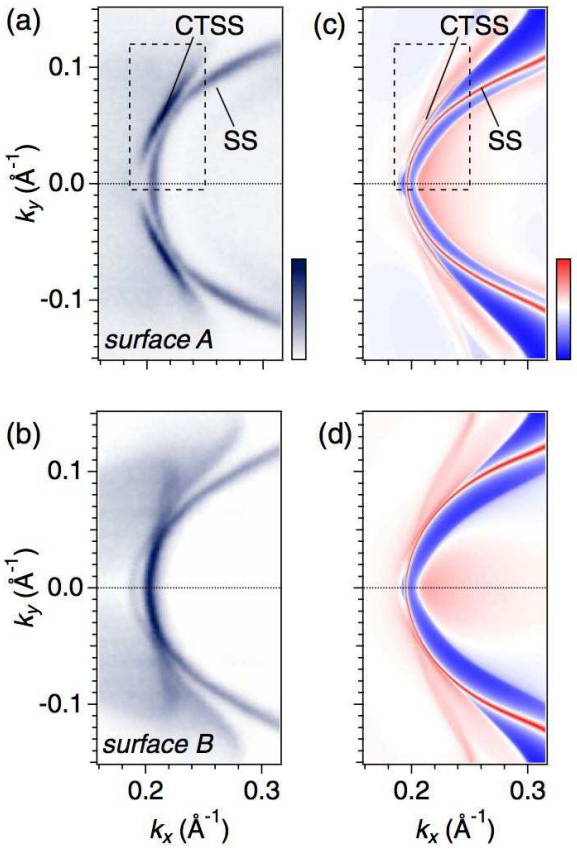

Figure 8.8: Detail study of the Fermi arcs on the A and B $MoTe_2$ surfaces. (a-b) High-resolution measured FSs for the surface terminations A and B respectively. (c-d) Surface DOS, for the two surface terminations, calculated 10 meV below the Fermi level. Adapted from [21].

8.2 Experimental Results: Persistence of a Surface State Arc in the Topologically Trivial Phase of $MoTe_2$

The prediction of Weyl fermions in the low temperature non-centrosymmetric $1T'$ phase of $MoTe_2$ still awaits a clear experimental confirmation. Here we report angle resolved photoemission (ARPES) data and *ab initio* calculations that reveal a surface state arc dispersing between the valence and the conduction band, as expected for a Weyl semimetal. However, we find that the arc survives in the high temperature centrosymmetric $1T''$ phase. Therefore, the presence of a surface Fermi arc cannot be an unambiguous fingerprint of a topologically non-trivial phase. We have also investigated the surface state spin texture of the $1T'$ phase by spin resolved

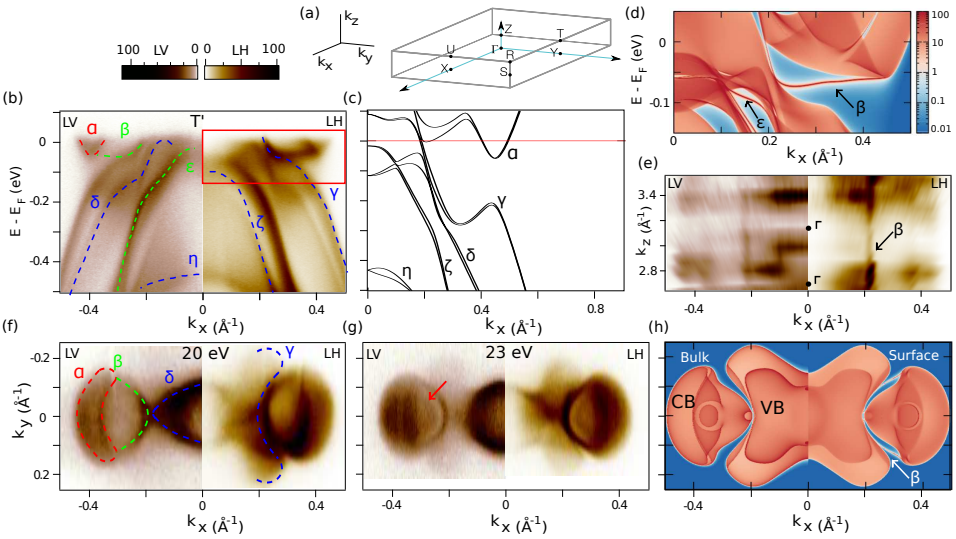

Figure 8.9: (a) Sketch of the bulk Brillouin zone (BZ) of orthorhombic $1T'$ $MoTe_2$. (b) ARPES image along the k_x direction measured with 20 eV photon energy at 77 K, with both LV and LH polarizations, for negative and positive wavevectors, respectively. Dashed lines trace the preeminent spectral features, labelled with greek letters $\alpha - \eta$. (c) Calculated bulk band structure for the $1T'$ phase along ΓX. (d) Bulk and surface momentum-resolved local density of states calculated within a semi-infinte crystal method and integrated over k_z. Two surface states, labelled β and ϵ, disperse within two different projected gaps. (e) Experimental Fermi surface in the (k_x, k_z) plane, obtained from a photon energy scan between 16 and 40 eV, for an inner potential $V_0 = 14$ eV. (f - g) Experimental Fermi surface in the (k_x, k_y) plane measured with 20 eV photon energy at 77 K (f) and with 23 eV photon energy at 30 K (g). β forms an arc (green line) dispersing between the electron pocket centered at $k_x = \pm 0.4$ Å^{-1} (red line) and the hole pockets centered at Γ (blue line). (h) A comparison of the projected local density of states at the Fermi level, calculated within the semi-infinte crystal method for the bulk (negative wavevectors) and the surface (positive wavevectors), highlights the β surface state arc.

ARPES, and identified additional topologically trivial spin-split states within the projected band gap at higher binding energy.

Transition metal dichalcogenides (TMDs) MX_2, where M is a transition metal and X = S, Se or Te, have been a paradigm for many exotic ground states [147, 148]. Te-based semimetallic TMDs, in particular, have been recently in the limelight. Interest was initially motivated by their

unique transport properties, such as non-saturating linear magnetoresistance [134] and superconductivity under pressure [135, 136]. More recently, the prediction of a novel Weyl semimetal phase in the non-centrosymmetric compound WTe_2 has shifted the focus to the topological nature of their electronic phases [149].

Weyl semimetals (WSMs) are a novel quantum phase of matter, emerging in systems where either inversion or time reversal symmetries are broken [150, 151]. Conduction and valence band states cross the Fermi energy (E_F) at special nodes, called Weyl points. The Fermi surface, formed by isolated Weyl points, is responsible for unusual magnetotransport properties [152, 153] and it guarantees topological protection to open surface states, Fermi arcs [154]. Point-like bulk Fermi surface and surface Fermi arcs are Hallmarks of the so-called type-I WSM, experimentally reported in TaAs [154, 155, 156, 157] and similar compounds [158].

The WSMs classification has been enlarged by the recent prediction of a type-II topological phase. This is characterized by the topologically-protected degeneracy of the conduction and valence band states forming highly distorted Weyl cones [149]. WTe_2 was proposed as a first candidate for realizing this type-II WSM, but the small momentum separation between opposite Weyl points has so far hampered a direct experimental evidence.

More recently, the isostructural orthorhombic $MoTe_2$ [159, 146, 160] and Mo/WP_2 [161] were predicted to host more extended surface Fermi arcs, which should be observable with the resolution of present angle resolved photoemission spectroscopy (ARPES) experiments. This prediction has prompted a number of experimental investigations [140, 141, 142, 143, 144, 21, 145], with partially conflicting results. In particular, the number of surface states and their topological nature are still under debate [21, 140, 141, 144, 142, 143, 145].

Here we combine *ab initio* calculations with polarization-dependent ARPES studies to discriminate the bulk and surface electronic structure of $MoTe_2$. We report the dispersion within the projected band gap of a surface state (SS) that might be interpreted as the surface Fermi arc of a WSM, as proposed elsewhere [140, 142, 143]. However we find that the SS survives also at high temperature, topologically trivial, centrosymmetric $1T''$ phase, as confirmed by *ab initio* calculations. This shows that it is not possible to draw a definite conclusion about the occurrence of the type-II WSM phase just on the basis of the observation of this surface state. We have also investigated the in-plane spin texture of the $1T'$ phase, looking for evidences supporting the type-II WSM phase, and found more topologically trivial spin-split states dispersing in

the projected band gaps.

High quality $\mathrm{MoTe_2}$ single crystals were grown by vapour transport, see the next section 8.3 for further details. At room temperature $\mathrm{MoTe_2}$ can crystallize in the semiconducting 2H phase and in the semimetallic $1\mathrm{T}''$ phase (also called β [21, 146] phase or $1\mathrm{T}'$ phase [159]). The $1\mathrm{T}''$ phase exhibits at $T\sim 240\,\mathrm{K}$ a transition to the $1\mathrm{T}'$ structure (also called γ phase or $\mathrm{T_d}$ phase [162]). The $1\mathrm{T}''$ monoclinic crystal cell is centrosymmetric with space group $P12_1/m1$, whereas the $1\mathrm{T}'$ phase is orthorhombic as a consequence of the relative sliding of Mo and Te layers and it belongs to the $Pmn2_1$ space group. Inversion symmetry is broken in the $1\mathrm{T}'$ phase, which is the only structure capable of supporting the WSM phase [146, 21].

We performed ARPES experiments at the APE beamline of the Elettra synchrotron. The end-station is equipped with a DA30 Scienta hemispherical analyzer with a novel high efficiency V-LEED spin detector [163]. The energy and angular resolution were 15 meV and 0.2 ° for ARPES, and 45 meV and 0.75 ° for the spin-resolved ARPES (SR-ARPES) measurements. Data were collected in the 300 K - 30 K temperature range, at photon energies between 16 eV and 40 eV. The electronic band structure of $\mathrm{MoTe_2}$ has been calculated within the density functional theory (DFT) framework employing the generalized gradient approximation (GGA) as implemented in the QUANTUM ESPRESSO package [164, 165, 166]. Spin-orbit effects were accounted for using fully relativistic norm-conserving pseudopotentials [167]. The calculations for the $1\mathrm{T}''$ phase have been carried out for crystal lattice parameters $\beta = 93.917°$, $\mathrm{a} = 6.33$ Å, $\mathrm{b} = 3.47$ Å, $\mathrm{c} = 13.86$ Å[168]. Whereas the low temperature $1\mathrm{T}'$ structure is characterized by $\mathrm{a} = 3.46$ Å, $\mathrm{b} = 6.30$ Å, $\mathrm{c} = 13.86$ Å[146].

Figure 8.9 (a) shows the $1\mathrm{T}'$ bulk BZ with the high symmetry points along the $\mathrm{k_x}$, $\mathrm{k_y}$ and $\mathrm{k_z}$ directions, of relevance for the discussed measurements. The broken inversion symmetry of the $1\mathrm{T}'$ phase results in two possible surface terminations. However, our *ab initio* calculations show that ultra high momentum and energy resolution is required to distinguish the two band structures. This has been experimentally achieved by means of laser-based ARPES [140, 21].

Figure 8.9 (b) displays the band structure measured with 20 eV photon energy at 77 K in the $1\mathrm{T}'$ phase along $\mathrm{k_x}$ (for the band dispersion on a larger energy window see section 8.3). Several sharps states are identified, testifying our samples quality. In figure 8.9 (b) and in the following we show for negative and positive wavevectors the dataset acquired with LV and LH polarizations, respectively. This provides a powerful method for distinguishing the various

bands, which we label with greek letters $\alpha - \eta$. LV corresponds to purely *s* polarization, while LH is a mixture of *p* and *s* polarization, due to the setup geometry (for more details see Refs. [169, 170]).

The experimental results are well reproduced by the calculated bulk band structure shown in fig. 8.9 (c). The conduction band (CB) intersects $\mathrm{E_F}$ and forms a sHallow electron pocket α, indicated by a red dashed line in fig. 8.9 (b). The valence band (VB) dispersion is more complex, with several hole-like bands $\gamma - \eta$, traced by blue dashed lines in fig. 8.9 (b). The β and ϵ dispersions, indicated by green dashed lines, are not captured by the bulk calculations, thus suggesting their surface origin.

Figure 8.9 (d) shows the momentum-resolved local density of states calculated along $\mathrm{k_x}$, by projecting all the possible $\mathrm{k_z}$ values, within a semi-infinite crystal method, including also the surface contribution. Concentrating on the energy-momentum region traced by the red rectangle in panel (b), we see the CB and VB appearing as a broad continuum due to the projection from various $\mathrm{k_z}$. Additional sharp states disperse within two projected gaps. We interpret them as the β and ϵ SSs. β touches CB and it crosses $\mathrm{E_F}$ at $\mathrm{k_F} \sim 0.2$ Å^{-1}, in good agreement with the experimental findings of fig.8.9 (b).

Figure 8.9 (e) shows the Fermi surface in the $\mathrm{k_x}$-$\mathrm{k_z}$ plane, extracted from a photon energy scan in the range 16-40 eV. The absence of $\mathrm{k_z}$ dispersion confirms the two dimensional character of the β SS. This state, which is indicated by an arrow, is sharp and well resolved over the entire 3D BZ. Also the ϵ SS has no appreciable $\mathrm{k_z}$ dispersion, as shown in section 8.3.

Figure 8.9 (f) shows the Fermi surface in the $\mathrm{k_x}$-$\mathrm{k_y}$ plane for the experimental conditions of panel (b). CB forms a closed banana-shaped contour centered at $k_x \sim \pm 0.4$ Å^{-1} indicated by a red dashed line, while VB displays multiple Fermi surface sheets, traced by blue dashed lines. In LV polarization we resolve an inner diamond-shaped contour derived from δ, while in LH polarization we resolve an external flower-shaped state derived from γ. The β SS forms an arc, indicated by a green dashed line. This is more clearly seen in fig. 8.9 (g) for the Fermi surface acquired with 23 eV photon energy at 30 K. At this photon energy we resolve an additional Fermi surface sheet arising from CB, indicated by a red arrow in panel (g).

All these features are well reproduced by our calculated Fermi surface. Figure 8.9 (h) shows the Fermi surface calculated within the semi-infinite crystal method, projected from all the possible $\mathrm{k_z}$ values. Negative and positive wavevectors show the calculations for the bulk and at the

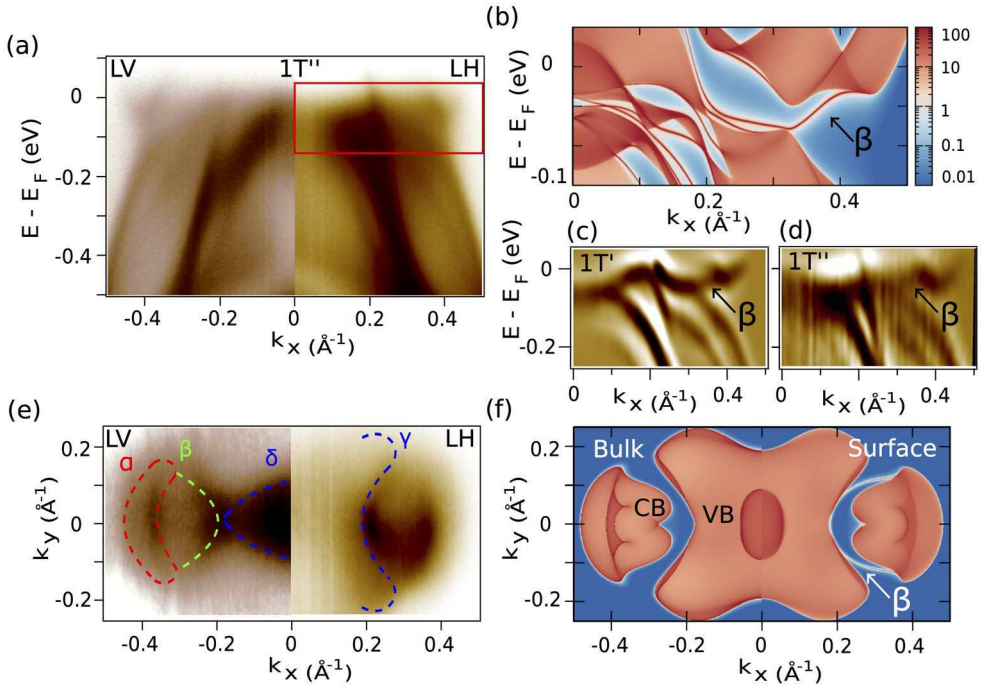

Figure 8.10: (a) ARPES image of $1T''$ $MoTe_2$ along the k_x direction measured at 20 eV photon energy at room temperature. (b) Calculated band structure within the semi-infinte crystal model. The β SS disperse between CB and VB also in the centrosymmetric phase. (c, d) second derivative of the ARPES intensity measured along k_x in the $1T'$ and $1T''$ phases, respectively. (e) Fermi surface measured at 20 eV photon energy. Dashed color lines outline the contours of the different Fermi sheets. (f) Calculated Fermi surface in the bulk and at the surface, showing that the SS arc persists in the centrosymmetric $1T''$ phase.

surface, respectively. By comparing the two, we immediately recognize the β SS Fermi arc. Its open contour dispersing between the bulk bands suggests the possibility to interpret it as the fingerprint of the WSM phase, as recently proposed [140, 142, 143].

However, hereafter we show that this observation alone is not sufficient to confirm the type II WSM nature of $MoTe_2$. Additional surface states, which might also be interpreted as Fermi arcs [141, 144, 21], are predicted by our calculations. Unfortunately, they are too close to be resolved in the experiment.

We have investigated the evolution of the band structure with temperature across the structural transition from the $1T'$ to the $1T''$ phase. Figure 8.10 (a) shows the ARPES band structure

of the $1T''$ phase measured along the k_x direction with 20 eV photon energy at room temperature. All states previously described are still visible, albeit thermally broadened. The persistence of the SS in the $1T''$ phase is confirmed by the band structure calculations, shown in figure 8.10 (b). In order to increase the contrast of the β SS, fig. 8.10 (c) and (d) show the second derivative of the ARPES intensity measured along k_x in the $1T'$ and $1T''$ phases. The β SS, indicated by black arrows, is clearly resolved in both phases.

This observation is further supported by a close look at the $1T''$ phase Fermi surface, in fig. 8.10 (e). For LV polarization, we detect the banana-shaped electron pocket and the inner diamond-shaped hole pocket, in agreement with fig. 8.9 (f). For LH polarization, we resolve intensity along the arc connecting the outer flower-shaped hole state to the electron pocket, thus confirming the presence of the SS also in the $1T''$ phase. Finally, figure 8.10 (f) shows the calculated Fermi surface in the bulk (negative wavevectors) and at the surface (positive wavevectors) for $1T''$ $MoTe_2$. Similarly to the low temperature $1T'$ case, the β SS forms an arc dispersing between CB and VB. Hence, SS survives in the centrosymmetric structure and it alone cannot be a fingerprint of the Weyl semimetal phase. Our experimental findings extend theoretical calculations showing that the topological nature of β can be changed by artificially varying the low temperature $1T'$ crystal lattice [21].

We discuss now the results of our investigation of the spin properties of the $1T'$ phase of $MoTe_2$. Figure 8.11 summarizes our SR-ARPES results, measured at 30 K with 23 eV photons and LH polarization. Figure 8.11 (a) shows a zoom on the β SS Fermi contour. White circles mark the 9 regions of the BZ where we have evaluated the spin up (S_{up}) and down (S_{down}) projections along the k_x direction. Green solid and dashed lines indicate the directions along which the calculations shown in panel (d) and (e) were performed.

From the spin polarized ARPES intensity (I_+, I_-), measured from the VLEED targets, we extracted the spin polarization P_x and the spin up and down components $S_{up/down}$, as detailed in the next additional section. Figure 8.11 (b) and (c) show in red and blue the $S_{up/down}$ signals in regions 1 and 9, respectively. We resolve several spectral features: the β SS crossing E_F and two peaks with large spin polarization (up to $50\,\%$), centered at $E - E_F \sim -0.5$ eV and $E - E_F \sim -0.7$ eV, respectively. We interpret these as the two spin components of the spin-split ϵ state and we label them ϵ^+ and ϵ^-.

Figure 8.11 (d) displays the calculated band structure along k_y, at $k_x = 0.3$ Å^{-1}, for a 20

layer thick slab. The colors encode the P_x component of the spin polarization of the β and ϵ SSs. It supports our experimental findings, in particular the spin-splitting in ϵ^+ and ϵ^- and the reversal of the spin polarization in the two branches for opposite k_y values. Additional weak spin signals are observed in proximity of the bulk states due to the partial hybridization of the ϵ states with the bulk states.

A small spin polarization is observed in β (for a zoom at E_F see section 8.4). However, the total spin polarization integrated at E_F is smaller than 10%, and the actual experimental energy and momentum resolution is not sufficient to fully describe the spin polarization in the β SS. Calculations show that a second branch with opposite spin disperses in proximity of the bulk states. This can be more clearly seen in fig. 8.11 (e), showing the calculated bands along k_x, at at $k_y = 0$ Å^{-1}. Here, the colors encode the P_y component, which was not directly investigated in our study. Black arrows indicate the β and ϵ^+ states, while the green arrow points to the second spin-polarized state in proximity of β.

We propose that, owing to the limited experimental energy resolution, the contribution of the two spin states cannot be resolved, thus explaining the small experimental spin polarization in proximity of E_F. Figure 8.11 (f) shows the evolution of the spin polarization, P_x. When going from region 1 to 5, we observe that the absolute value of P_x in ϵ^+ and ϵ^- decreases, it becomes null in region 5, and it changes sign for opposite values of k_y, from regions 6 to 9.

In summary, we have investigated the electronic structure of the type-II Weyl semimetal candidate $MoTe_2$, by means of combined *ab initio* calculations and ARPES. We have reported the existence of two-dimensional β and ϵ surface states, dispersing in different projected band gaps. The β SS forms an arc connecting the bulk conduction and valence bands. Similar observations has been recently interpreted as the smoking gun of the WSM phase[140, 142, 143]. However, our data show that the β SS persists in the centrosymmetric $1T''$ phase. Therefore, the observation of a surface Fermi arc alone does not establish the type II Weyl phase.

We also investigated the spin polarization of the band structure, and found a large spin signal in the ϵ SS, which is formed by a pair of spin-split branches. This observation is supported by *ab initio* calculations. The calculations also predict the β SS to be spin polarized. However, the β SS shows very small spin polarization, probably as a consequence of the close proximity with another state with opposite spin polarization, which we could not resolve in the experiment.

Finally, our results can neither prove nor refute the type-II Weyl semimetal nature of $MoTe_2$.

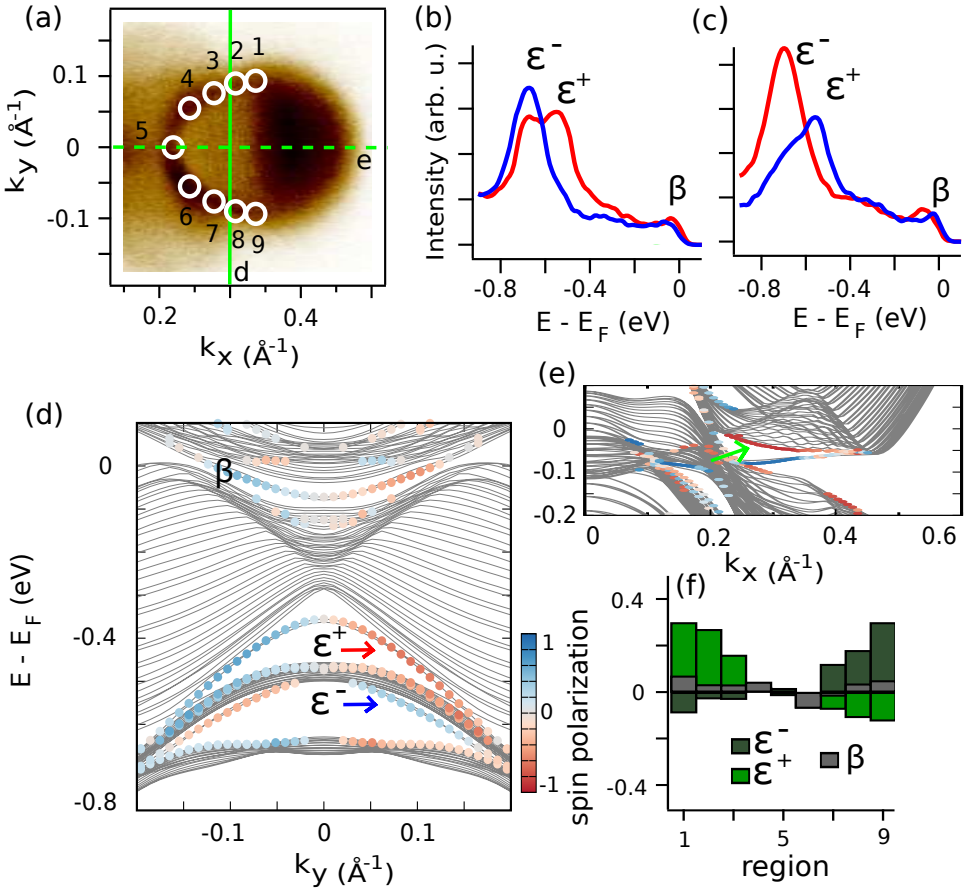

Figure 8.11: (a) Fermi surface of 1T′ $MoTe_2$ at 30 K as measured with 23 eV photon energy and LH polarization. White circles indicate the regions where we have extracted the spin up and down projections along the k_x direction. Green continuous and dashed lines indicate the directions of the calculations shown in panel (d) and (e), respectively. (b, c) S_{up} (red) and S_{down} (blue) in regions 1 and 9. The spin projections are evaluated from the raw data accounting for the experimental asymmetry and the detector Sherman function [171]. (d) Calculated surface spin polarization along k_x of the β and ϵ SS superimposed to the calculated band structure along $k_x = 0.3$ Å^{-1} for a 20 layers thick slab. (e) Calculated surface spin polarization along k_y in proximity of E_F for the band structure along k_x for a 20 layers thick slab. A second spin polarized state (green arrow) disperses close to β (black arrows) with opposite spin projection. (f) Evolution of P_x along k_x in the β SS and in the two branches of the spin-split ϵ SS.

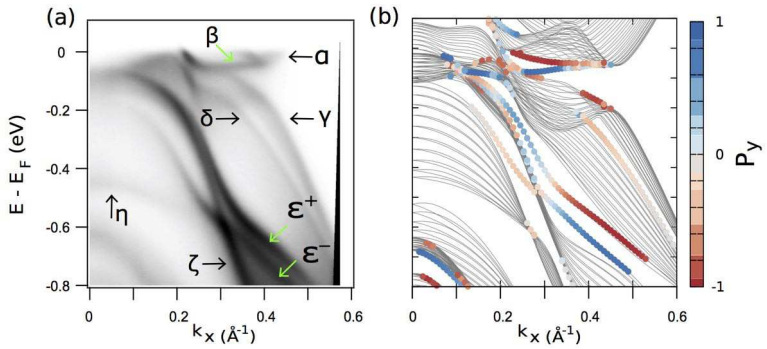

Figure 8.12: (a) ARPES data along the k_x direction at 20 eV photon energy with LH polarization. The wider energy range, compared to the data of fig.1 allows to identify the dispersion of the two spin split components of the ϵ SS, indicated by two green arrows at energies lower than 0.5 eV. The dispersion of the various bulk and surface states is well supported by the *ab initio* calculations of panel (b). The calculations show the spin projections (up in red, down in blue) along k_y of the states at the surface as obtained for a 20 layer thick slab. (c) Constant energy map (CEM) in the (k_x, k_z) plane as extracted from the photon energy scan 0.7 eV below the Fermi level.

Besides β and ϵ, additional surface states might disperse in proximity of the bulk states, but elude our detection capabilities owing to the limited energy and angular resolution. These additional states are predicted by our calculations and similarly suggested in Ref. [21, 144, 141]. Only SR-ARPES measurements with energy and momentum resolution comparable to the laser based ARPES setup of Refs. [21, 140] will be able to settle this issue, by resolving the spin texture of all the bulk and surface state contributions.

8.3 Supplementary Material

8.3.1 Experimental and Calculated Band Structure Over a Wider Energy Range

High quality single crystals were produced by the chemical vapour transport method. Stoichiometry mixture of high purity Mo and Te was encapsulated in a quartz ampule together with Iodine used as transport agent. The source and sink temperature were 1000°C and 940°C, respectively. At the end of the process, elongated crystals are obtained exposing flat (001) surfaces large sev-

eral mm^2. The samples were cleaved in UHV at room temperature by scotch tape technique and the orientation was controlled by means of low energy electron diffraction (LEED).

In order to identify more clearly the dispersion of the two spin split components of the ϵ SS, we draw in fig. 8.12 a comparison between the experimental (a) and calculated (b) band structure, on a wider energy range than the one shown in fig. 8.9. The data of panel (a) are measured along the $\mathrm{k_x}$ direction at 20 eV photon energy with LH polarization. The calculations of panel (b) result from a 20 layer thick slab. The spin projections along the $\mathrm{k_y}$ direction at the surface are shown in red (spin up) and blue (spin down). All the spectral features, labelled by α - η are clearly visible. Moreover, at energies lower than 0.5 eV we clearly resolved the two spin components ϵ^+ and ϵ^-, indicated by green arrows. The spin split SSs disperse between the bulk valence band states δ and ζ. Tracking the dispersion of these states at energies closer to E_F is hampered by the partial hybridization of the surface states with the bulk valence band, as it is more clearly shown by the calculations of figure 8.12 (b).

Figure 8.12 (c) shows a constant energy map (CEM) 0.7 eV below the Fermi level in the ($\mathrm{k_x}$, $\mathrm{k_z}$) plane, as extracted from a photon energy dependent study in the range 16 eV - 40 eV. The CEM intersects the spin split ϵ^+ and ϵ^- states, as indicated by the red dashed line in fig. 8.12 (a). The two states, indicated by green arrows, show no appreciable $\mathrm{k_z}$ dispersion, in agreement with the interpretation in terms of surface states.

8.3.2 Analysis of the Spin Resolved ARPES Data

We extend the discussion about the analysis of the spin resolved ARPES data. Figure 8.13 (a) and (b) shows $\mathrm{I_+}$ and $\mathrm{I_-}$, the measured signal from the VLEED target for the majority and minority spin direction, as measured in region 1 and 9, respectively. Red and blue lines show the two opposite spin projections. From the measured $\mathrm{I_+}$ and $\mathrm{I_-}$, we calculated the spin polarization, which is defined as $\mathrm{P_x} = \frac{(\mathrm{I_+ - I_-})}{\mathrm{S} \times (\mathrm{I_+ + I_-})}$, where S is the detector Sherman function, whose value of 0.3 has been calibrated from reference measurements of the spin polarized Au(111) surface.

Figure 8.13 (e) show the energy distribution of $\mathrm{P_x}$ in region 1 (orange) and region 9 (black). Two spin polarized features are clearly resolved, centred at -0.7 eV and -0.5 eV. We extract the average spin polarization below the peak, and the evolution in the nine investigated regions is shown in fig. 8.11 (f). The spin polarization of ϵ_- and ϵ_+ are averaged in the energy region between (-0.9 eV, -0.6 eV) and (-0.6 eV, -0.3 eV) respectively, while the spin polarization of β

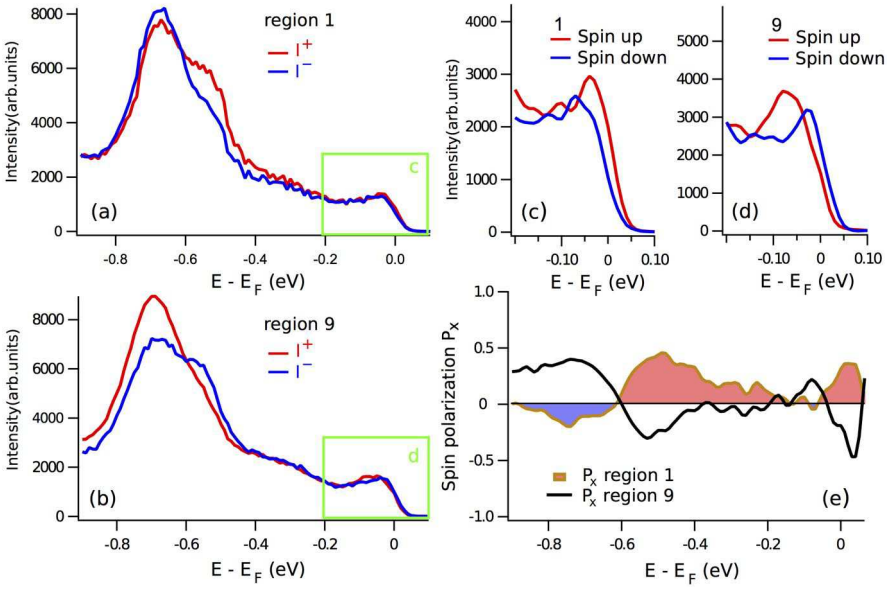

Figure 8.13: (a) and (b) I_+ and I_- signal from the VLEED target, for the majority and minority spin direction, measured in region 1 and 9 for the spin projection along k_x, respectively. (c) and (d) Zoom at the Fermi level, in the region indicated by green rectangles, of the spin up and down signal, evaluated from I_+ and I_- according to the relations$S_{up/down} = (1 \pm P_x) \times (I_+ + I_-)$. (e) Energy distribution of the spin polarization along the k_x directions in region 1 (orange) and region 9 (black).

is averaged in the range (-0.15 eV , 0 eV).

Figure 8.11 (b) and (c) show the spin up and down projections corresponding to the $I_+/-$ of figure 8.13 (a) and (b), respectively. The spin up/down are calculated following the relations $S_{up/down} = (1 \pm P_x) \times (I_+ + I_-)$. Figure 8.13 (c) and (d) show a zoom of the spin up and down projections, in proximity of E_F, in the energy region indicated by green rectangles in figure 8.13 (a) and (b). A small spin polarization is observed at E_F which is attributed to the β surface state. However the value of the spin polarization in β is always $< 10\%$, and for this reason a quantitative analysis is beyond the scope of the present study. However, we stress the fact that the calculations of figure 8.12(b) predict the β surface state to be spin polarized.

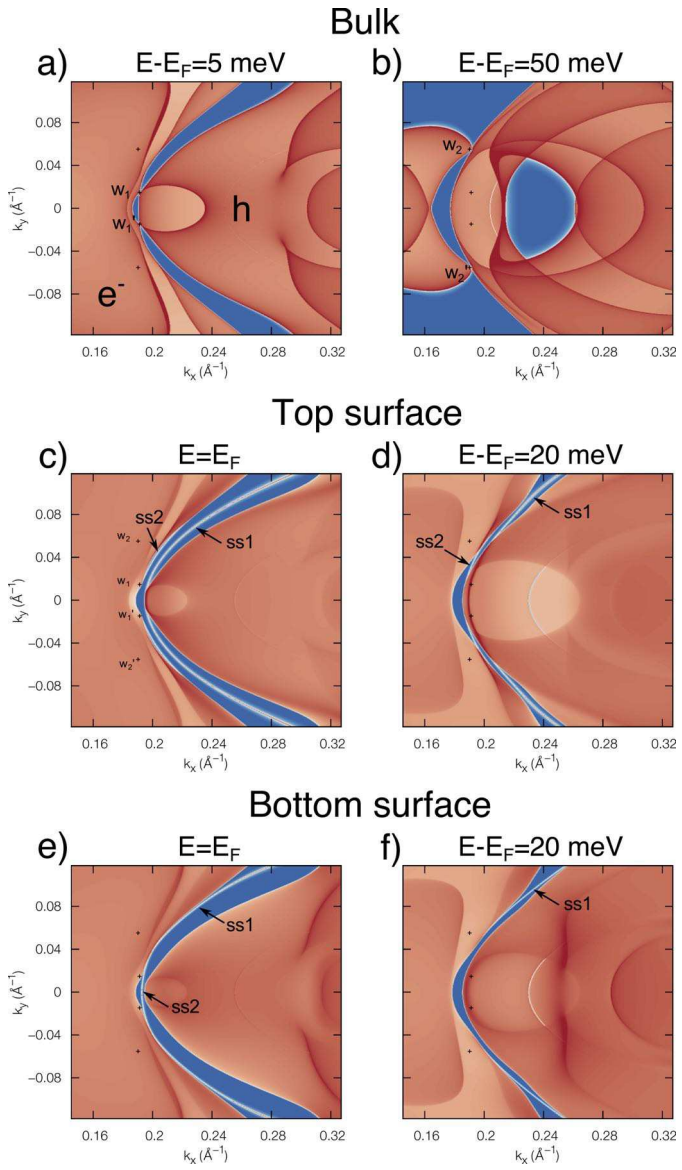

Figure 8.14: (a) and (b) k_x and k_y-resolved bulk density of states projected on the (001) surface at the energy of Weyl point w_1 (a) and w_2 (b). (c)-(f) k_x and k_y-resolved surface density of states on the (001) top (c,d) and bottom (e,f) surface at the Fermi level (c,e) and between the two Weyl points (d,f).

8.3.3 First principles calculations: Weyl points and surface states

First-principles calculations of the electronic structure of $MoTe_2$ in the orthorhombic 1T' phase were performed within the density functional theory framework using the generalized gradient

approximation as implemented in the Quantum-Espresso package [164]. We used the crystal structure of Ref. [146] and norm-conserving relativistic pseudopotentials. In accordance with previous calculations [146], we find that the band structure host two nonequivalent Weyl points w_1 and w_2 whose time-reversal and mirror images give a total of 8 Weyl points in the Brillouin zone. Both Weyl points are of type-II appearing at touching point of hole and electron pockets at 5 meV (w_1) and 50 meV (w_2) above the Fermi level (fig. 8.14 a and b).

The (001) surface density of states was computed from the semi-infinite Green function [165] derived from a tight-binding Hamiltonian in the Mo-d and Te-p projected Wannier basis [166]. At the Fermi level, two surface states $SS1$ and $SS2$ are present on the top surface (fig.8.14c). The long surface state $SS1$ corresponds to the β surface state seen in ARPES experiments previously shown. Both surface states reconnect to the bulk pocket from which they emerge so that no conclusion can be made about their topological character. By examining the same two states at an energy between the two Weyl points ($E - E_F = 20$ meV, fig.8.14 d), we can see that the states $SS2$ connect the hole and electron pockets, and correspond thus to the topological Fermi arc, while the $SS1$ state is trivial. On the bottom surface, the situation is reversed. Again, at the Fermi level (fig.8.14 e), two surface states can be seen, including the long $SS1$ state which corresponds to the β surface state seen in ARPES. At the Fermi level, no conclusion can be drawn about the topological character of the two states. At $E-E_F = 20$ meV, the $SS2$ state disappears while the $SS1$ state clearly connects the electron and hole pocket and is thus the topological Fermi arc.

To confirm the topological character of the states connecting electron and hole pockets, we computed the $\mathbb{Z}_2$ invariant of the time-reversal symmetric plane $\mathcal{P}$ of the Brillouin zone passing between the w_1 and w_2 point (fig.8.15a). Using the Wannier center technique [172] as implemented in the Z2Pack package [173], we found that the plane $\mathcal{P}$ has a non-trivial $\mathbb{Z}_2$ invariant $\nu = 1$ (fig.8.15 b) and thus that topologically protected states are expected to cross the projection of $\mathcal{P}$ on the (001) surface. these states correspond to the $SS1$ and $SS2$ on the bottom and top surface respectively.

Our calculations thus show that depending on the observed surface, the $SS1$ (β) state is trivial (top surface) or topologically protected (bottom surface). Moreover, as shown before, the β states remains in the topologically trivial 1T" phase. As a consequence, the observation of the β state alone does not provide any experimental confirmation of the presence of a Weyl

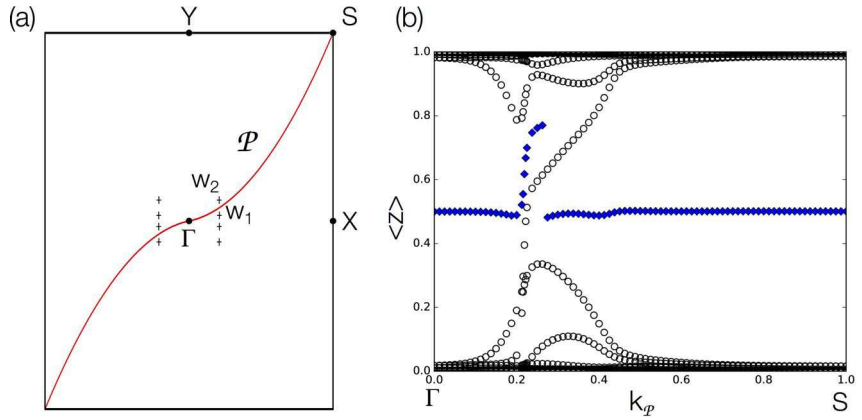

Figure 8.15: (a) Cut of the time reversal invariant plane $\mathcal{P}$ with the $k_z = 0$ plane, (b) evolution of the Wannier charge center position along the half-plane $\mathcal{P}$, showing $\mathcal{P}$ is non-trivial with $\mathbb{Z}_2$ invariant $\nu = 1$.

semimetal phase in 1T' $MoTe_2$. Only the observation of both $SS1$ and $SS2$ is a proof of the presence of the type-II Weyl points, as proposed in Ref.[21, 141].

Chapter 9

Conclusions

This chapter contains conclusive remarks and summarizes the main results of the thesis.
The work consists of an experimental investigation of the equilibrium and out-of-equilibrium electronic properties of different materials belonging to the class of Topological Insulators (TIs), Topological Kondo Insulators (TKIs) and Weyl Semimetals (WSMs).

By exploiting TR-ARPES, I have studied six distinct TIs having different $\mathrm{E_F}$ positions with respect to the electronic band structure. This part of my work was aimed at the comprehension of the bulk and surface states contributions to the electronics relaxation processes that follow an optical excitation. Regardless of the material specific band structure, when $\mathrm{E_F}$ intersects bulk states (as for n-type and p-type TIs) the electron populations dynamics relax with a characteristic time scale of few ps. Differently, when $\mathrm{E_F}$ lies within the bulk band gap (intrinsic TIs), the relaxation dynamics is more than one order of magnitude slower. The temporal evolution of the electronic temperature $\mathrm{T_e}$ has shown that bulk states provide an efficient channel to dissipate the extra-energy provided by the optical excitation.

We have ascribed this effective removal of hot charges in n- and p-doped TIs to a diffusion process, mediated by the presence of 3D states at $\mathrm{E_F}$. In intrinsic TIs, 2D surface states restrain part of the energy. Indeed, in-plane diffusion and electron-phonon scattering are not as efficient as for the 3D diffusion to remove the energy from the sHallow surface region investigated by the surface-sensitive ARPES. Bulk diffusion mechanisms have been often overlooked in the recent TR-ARPES studies on TIs. However, these processes might play, in a more general form, an important role also in the out-of-equilibrium physics of other materials.

Concerning the study of SmB_6 compound, that have been proposed as the first strongly-correlated TIs, electronic correlations are of particular relevance. Hence, we have performed a detailed investigation of SmB_6 transient electronic structure aimed at estimating the electron-phonon coupling constant λ. A 2TM model has been adopted to mimic the evolution of the extracted electronic temperature. By assuming that the electron-phonon coupling is mostly mediated by low energy Sm phonon modes, we have estimated a range for λ spanning from 0.13 ± 0.03 to 0.04 ± 0.01. Interestingly, the average value of λ is slightly smaller with respect to other hexaborides. Our results can be considered not only as a reference for future for momentum-integrated measurement of λ, but may also for promoting further investigations of the SmB_6 electron-phonon coupling.

A fundamental aspect for the formation of TIs, as we have pointed out in chapter 3, is the inversion of parity in the states forming the bulk gap. To directly prove this mechanism I have performed a linear-dichroic ARPES photon-energy dependent investigation of the $GeBi_2Te_4$ TI. My study has focused on bulk valence band states, in proximity of the region where the band gap is expected to invert. The measurements have successfully revealed a change in the dichroic signal which has been interpreted as a change in the nature of the orbitals responsible for the emergence of the topological phase. Moreover, I have revealed evidences of a possible surface resonance effect between topological surface states and the bulk valence band.

The recently discovered Weyl semimetals have been treated in the last part of the thesis work. We have investigated the type-II Weyl semimetal candidate $MoTe_2$ by means of combined *ab initio* calculations and ARPES. Recent studies have proposed controversial interpretations regarding the number and the nature of the Fermi arcs. Our data have shown the presence of two-dimensional surface states forming Fermi arcs connecting the bulk conduction and valence bands. Unexpectedly, these arcs persist in the centrosymmetric $1T''$ phase, in which $MoTe_2$ is not expected to be a WSM. As a result, we claim that the observation of a surface Fermi arc alone does not constitute a fingerprint of the type II Weyl phase.

The present research work provides a comprehensive picture of the optically-induces electron dynamics and relaxation processes in TIs.

List of Publications

1. "*Bulk diffusion relaxation mechanisms in optically excited Topological Insulator*", A. Sterzi, G. Manzoni, A. Crepaldi, F. Cilento, L. Sbuelz, M. Zacchigna, Ph. Bugnon, H. Berger, A. Magrez, M. Grioni, and F. Parmigiani, Phys. Rev. B accepted (2017).

2. "*Persistence of a surface state arc in the topologically trivial phase of* $\mathrm{MoTe_2}$", A. Crepaldi, G. Autes, A. Sterzi, G. Manzoni, M. Zacchigna, F. Cilento, I. Vobornik, J. Fujii, Ph. Bugnon, A. Magrez, H. Berger, F. Parmigiani, O. V. Yazyev, and M. Grioni, Phys. Rev. B 95, 041408(R) (2017).

3. "$\mathrm{SmB_6}$ *electron-phonon coupling constant from time-and angleresolved photoelectron spectroscopy*", A. Sterzi, A. Crepaldi, F. Cilento, G. Manzoni, E. Frantzeskakis, M. Zacchigna, E. van Heumen, Y. K. Huang, M. S. Golden, and F. Parmigiani, Phys. Rev. B 94, 081111(R) (2016).

4. "*Linear dichroic signal in the ARPES study of the topological insulator* $\mathrm{GeBi_2Te_4}$", A. Sterzi, G. Manzoni, A. Crepaldi, F. Cilento, M. Zacchigna, M. Leclerc, Ph. Bugnon, H. Berger, L.Petaccia, M.Grioni and F. Parmigiani. (In preparation).

5. "*Ultrafast Optical Control of the Electronic Properties of* $\mathrm{ZrTe_5}$", G. Manzoni, A. Sterzi, A. Crepaldi, M. Diego, F. Cilento, M. Zacchigna, Ph. Bugnon, H. Berger, A. Magrez, M. Grioni, and F. Parmigiani, Phys. Rev. Lett. 115, 207402 (2015).

6. "*Advancing non-equilibrium ARPES experiments by a 9.3 eV coherent ultrafast photon source*", F. Cilento, A. Crepaldi, G. Manzoni, A. Sterzi, M. Zacchigna, Ph. Bugnon, H. Berger, and F. Parmigiani J. Electr. Spectrosc. Relat. Phenom. 207, 7 (2016).

7. "*Evidence for a Strong Topological Insulator Phase in* $\mathrm{ZrTe_5}$", G. Manzoni, L. Gragnaniello, G. Autes, T. Kuhn, A. Sterzi, F. Cilento, M. Zacchigna, V. Enenkel, I. Vobornik, L. Barba, F. Bisti, Ph. Bugnon, A. Magrez, V.N. Strocov, H. Berger, O.V. Yazyev, M. Fonin, F. Parmigiani, and A. Crepaldi, Phys. Rev. Lett. 117, 237601 (2016).

8. "*Temperature dependent non-monotonic bands shift in* $\mathrm{ZrTe_5}$", G. Manzoni, A. Crepaldi, G. Autes, A. Sterzi, F. Cilento, A. Akrap, I. Vobornik, L. Gragnaniello, Ph. Bugnon, M. Fonin, H. Berger, M. Zacchigna, O.V. Yazyev and F. Parmigiani, J. Electr. Spectrosc. Relat. Phenom. (2016).

Acknowledgements

First of all I would like to thank my supervisor, Prof. Fulvio Parmigiani, who has always been a reference point of reference for me as a person, but also for my research work. I am also extremely grateful to my co-supervisors, Alberto Crepaldi and Federico Cilento, for providing me with a constant support over all these past years, from the beginning to the end of my PhD.
Hereafter, thanks to all people working in the T-Rex group in Trieste, in particular to Michele Zacchigna who supported me, and a thank to my colleague Giulia Manzoni, who shared with me my same itinerary. Last but not least, the results presented in this thesis work, have also been obtained through important collaborations with some research groups. I want to mention the important collaboration with Marco Grioni and with the Laboratory of Photoelectron Spectroscopy (LSE) at EPFL (Lausanne), and to Helmut Berger for growing and providing the samples analysed in this thesis. I want also to remark the cooperation with the M. Golden's group (Golden spectroscopy lab) and with Erik Van Heumen (Van Heumen Optical Spectroscopy lab) in Amsterdam.
Finally, thanks to my family for the encouragement they have constantly provided me.

Bibliography

[1] J M Kosterlitz and D J Thouless. Ordering, metastability and phase transitions in two-dimensional systems. *Journal of Physics C: Solid State Physics*, 6(7):1181, 1973.

[2] K. v. Klitzing, G. Dorda, and M. Pepper. New method for high-accuracy determination of the fine-structure constant based on quantized hall resistance. *Phys. Rev. Lett.*, 45:494–497, Aug 1980.

[3] J. Michael Kosterlitz David J. Thouless, F. Duncan M. Haldane. Nobel prize in physics 2016 for theoretical discoveries of topological phase transitions and topological phases of matter. `http://www.nobelprize.org/nobel_prizes/physics/laureates/2016/`, 2016.

[4] B. Andrei Bernevig and Shou-Cheng Zhang. Quantum spin hall effect. *Phys. Rev. Lett.*, 96:106802, 2006.

[5] Liang Fu and C. L. Kane. Topological insulators with inversion symmetry. *Phys. Rev. B*, 76:045302, Jul 2007.

[6] A. R. Mellnik, J. S. Lee, A. Richardella, J. L. Grab, P. J. Mintun, M. H. Fischer, A. Vaezi, A. Manchon, E. A. Kim, N. Samarth, and D. C. Ralph. Spin-transfer torque generated by a topological insulator. *Nature*, 511(7510):449–451, 07 2014.

[7] A. A. Baker, A. I. Figueroa, L. J. Collins-McIntyre, G. van der Laan, and T. Hesjedal. Spin pumping in ferromagnet-topological insulator-ferromagnet heterostructures. *Scientific Reports*, 5:7907 EP –, 01 2015.

[8] R. Valdés Aguilar, A. V. Stier, W. Liu, L. S. Bilbro, D. K. George, N. Bansal, L. Wu,

J. Cerne, A. G. Markelz, S. Oh, and N. P. Armitage. Terahertz Response and Colossal Kerr Rotation from the Surface States of the Topological Insulator Bi_2Se_3. *Phys. Rev. Lett.*, 108:087403, Feb 2012.

[9] J. W. McIver, D. Hsieh, H. Steinberg, P. Jarillo-Herrero, and N. Gedik. Control over topological insulator photocurrents with light polarization. *Nat Nano*, 7(2):96–100, 02 2012.

[10] J. A. Sobota, S. Yang, J. G. Analytis, Y. L. Chen, I. R. Fisher, P. S. Kirchmann, and Z.-X. Shen. Ultrafast Optical Excitation of a Persistent Surface-State Population in the Topological Insulator Bi_2Se_3. *Phys. Rev. Lett.*, 108:117403, 2012.

[11] Y. H. Wang, D. Hsieh, E. J. Sie, H. Steinberg, D. R. Gardner, Y. S. Lee, P. Jarillo-Herrero, and N. Gedik. Measurement of intrisinsic Dirac fermion cooling on the surface of a topological insulator Bi_2Se_3 using time- and angle-resolved photoemisison spectroscopy. *Phys. Rev. Lett.*, 109:127401, 2012.

[12] A. Crepaldi, B. Ressel, F. Cilento, M. Zacchigna, C. Grazioli, H. Berger, Ph. Bugnon, K. Kern, M. Grioni, and F. Parmigiani. Ultrafast photodoping and effective fermi-dirac distribution of the dirac particles in $bi2se_3$. *Phys. Rev. B*, 86:205133, Nov 2012.

[13] A. Crepaldi, F. Cilento, B. Ressel, C. Cacho, J. C. Johannsen, M. Zacchigna, H. Berger, Ph. Bugnon, C. Grazioli, I. C. E. Turcu, E. Springate, K. Kern, M. Grioni, and F. Parmigiani. Evidence of reduced surface electron-phonon scattering in the conduction band of bi_2se_3 by nonequilibrium arpes. *Phys. Rev. B*, 88:121404, Sep 2013.

[14] J. Sobota, S.-L. Yang, A. Kemper, J. Lee, F. Schmitt, W. Li, R. Moore, J. Analytis, I. Fisher, P. Kirchmann, T. Devereaux, and Z.-X. Shen. Direct optical coupling to an unoccupied dirac surface state in the topological insulator bi_2se_3. *Phys. Rev. Lett.*, 111:136802, 2013.

[15] M Hajlaoui, E Papalazarou, J Mauchain, L Perfetti, A Taleb-Ibrahimi, F Navarin, M Monteverde, P Auban-Senzier, C. R. Pasquier, N Moisan, D Boschetto, M Neupane, M. Z. Hasan, T Durakiewicz, Z Jiang, Y Xu, I Miotkowski, Y. P. Chen, S Jia, H. W. Ji, R. J. Cava, and M Marsi. Tuning a schottky barrier in a photoexcited topological insulator with

transient dirac cone electron-hole asymmetry. *Nature Communications*, 5:3003 EP –, 01 2014.

[16] Madhab Neupane, Su-Yang Xu, Yukiaki Ishida, Shuang Jia, Benjamin M. Fregoso, Chang Liu, Ilya Belopolski, Guang Bian, Nasser Alidoust, Tomasz Durakiewicz, Victor Galitski, Shik Shin, Robert J. Cava, and M. Zahid Hasan. Gigantic surface lifetime of an intrinsic topological insulator. *Phys. Rev. Lett.*, 115:116801, Sep 2015.

[17] Maxim Dzero, Kai Sun, Victor Galitski, and Piers Coleman. Topological kondo insulators. *Phys. Rev. Lett.*, 104:106408, Mar 2010.

[18] Xiangang Wan, Ari M. Turner, Ashvin Vishwanath, and Sergey Y. Savrasov. Topological semimetal and fermi-arc surface states in the electronic structure of pyrochlore iridates. *Phys. Rev. B*, 83:205101, May 2011.

[19] Su-Yang Xu, Ilya Belopolski, Nasser Alidoust, Madhab Neupane, Guang Bian, Chenglong Zhang, Raman Sankar, Guoqing Chang, Zhujun Yuan, Chi-Cheng Lee, Shin-Ming Huang, Hao Zheng, Jie Ma, Daniel S. Sanchez, BaoKai Wang, Arun Bansil, Fangcheng Chou, Pavel P. Shibayev, Hsin Lin, Shuang Jia, and M. Zahid Hasan. Discovery of a weyl fermion semimetal and topological fermi arcs. *Science*, 349(6248):613–617, 2015.

[20] Lunan Huang, Timothy M. McCormick, Masayuki Ochi, Zhiying Zhao, Michi-To Suzuki, Ryotaro Arita, Yun Wu, Daixiang Mou, Huibo Cao, Jiaqiang Yan, Nandini Trivedi, and Adam Kaminski. Spectroscopic evidence for a type II Weyl semimetallic state in $MoTe_2$. *Nat Mater*, 15(11):1155–1160, 11 2016.

[21] A. Tamai, Q. S. Wu, I. Cucchi, F. Y. Bruno, S. Riccò, T. K. Kim, M. Hoesch, C. Barreteau, E. Giannini, C. Besnard, A. A. Soluyanov, and F. Baumberger. Fermi Arcs and Their Topological Character in the Candidate Type-II Weyl Semimetal $MoTe_2$. *Phys. Rev. X*, 6:031021, Aug 2016.

[22] Stephan Hüfner. *Photoelectron Spectroscopy*. 1439-2674. Springer-Verlag Berlin Heidelberg, 2003.

[23] Andrea Damascelli. Probing the electronic structure of complex systems by arpes. *Physica Scripta*, 2004(T109):61, 2004.

[24] Yulin Chen. Studies on the electronic structures of three-dimensional topological insulators by angle resolved photoemission spectroscopy. *Frontiers of Physics*, 7(2):175–192, 2012.

[25] Andrea Damascelli, Zahid Hussain, and Zhi-Xun Shen. Angle-resolved photoemission studies of the cuprate superconductors. *Rev. Mod. Phys.*, 75:473–541, Apr 2003.

[26] L. Perfetti, . P. A Loukakos, M. Lisowski, U. Bovensiepen, H. Berger, S. Biermann, P. S. Cornaglia, A. Georges, and M.Wolf. Time Evolution of the Electronic Structure of 1T-TaS_2 through the Insulator-Metal Transition. *Phys. Rev. Lett.*, 97:067402, Aug 2006.

[27] F. Schmitt, P. S. Kirchmann, U. Bovensiepen, R. G. Moore, L. Rettig, M. Krenz, J.-H. Chu, N. Ru, L. Perfetti, D. H. Lu, M. Wolf, I. R. Fisher, and Z.-X. Shen. Transient Electronic Structure and Melting of a Charge Density Wave in $TbTe_3$. *Science*, 321(5896):1649–1652, 2008.

[28] L. Perfetti, P.A.Loukakos, M. Lisowski, U. Bovensiepen, H. Eisaki, and M. Wolf. Ultrafast electron relaxation in superconducting bi2sr2cacu2o8 by time-resolved photoelectron spectroscopy. *Phys. Rev. Lett.*, 99:197001, 2007.

[29] R. Cortés, L. Rettig, Y. Yoshida, H. Eisaki, M. Wolf, and U. Bovensiepen. Momentum-Resolved Ultrafast Electron Dynamics in Superconducting $Bi_2Sr_2CaCu_2O_{8+\delta}$. *Phys. Rev. Lett.*, 107:097002, Aug 2011.

[30] L. Rettig, R. Cortés, S. Thirupathaiah, P. Gegenwart, H. S. Jeevan, M. Wolf, J. Fink, and U. Bovensiepen. Ultrafast Momentum-Dependent Response of Electrons in Antiferromagnetic $EuFe_2As_2$ Driven by Optical Excitation. *Phys. Rev. Lett.*, 108:097002, Feb 2012.

[31] I. Avigo, R. Cortés, L. Rettig, S. Thirupathaiah, H. S. Jeevan, P. Gegenwart, T. Wolf, M. Ligges, M. Wolf, J. Fink, and U. Bovensiepen. Coherent excitations and electron–phonon coupling in Ba/$EuFe_2$ As_2 compounds investigated by femtosecond time- and angle-resolved photoemission spectroscopy. *Journal of Physics: Condensed Matter*, 25(9):094003, 2013.

[32] M Hajlaoui, E. Papalazarou, J. Mauchain, G. Lantz, N. Moisan, D. Boschetto, Z. Jiang, I. Miotkowski, Y. P. Chen, A. Taleb-Ibrahimi, L. Perfetti, and M. Marsi. Ultrafast surface carrier dynamics in the topological insulator bi2te3. *NanoLett.*, 12:3532–3536, 2012.

[33] S. K. Sundaram and E. Mazur. Inducing and probing non-thermal transitions in semiconductors using femtosecond laser pulses. *Nat Mater*, 1(4):217–224, 12 2002.

[34] Mathias Wagner. Expansions of nonequilibrium green's functions. *Phys. Rev. B*, 44:6104–6117, Sep 1991.

[35] L Perfetti, P A Loukakos, M Lisowski, U Bovensiepen, M Wolf, H Berger, S Biermann, and A Georges. Femtosecond dynamics of electronic states in the Mott insulator 1T-TaS_2 by time resolved photoelectron spectroscopy. *New Journal of Physics*, 10(5):053019, 2008.

[36] J. D. Koralek, J. F. Douglas, N. C. Plumb, Z. Sun, A. V. Fedorov, M. M. Murnane, H. C. Kapteyn, S. T. Cundiff, Y. Aiura, K. Oka, H. Eisaki, and D. S. Dessau. Laser Based Angle-Resolved Photoemission, the Sudden Approximation, and Quasiparticle-Like Spectral Peaks in $Bi_2Sr_2CaCu_2O_{8+\delta}$. *Phys. Rev. Lett.*, 96:017005, Jan 2006.

[37] W. S. Fann, R. Storz, H. W. K. Tom, and J. Bokor. Electron thermalization in gold. *Phys. Rev. B*, 46:13592–13595, Nov 1992.

[38] T.L. Perel'man S.I. Anisimov, B.L. Kapeliovich. Electron emission from metal surfaces exposed to ultrashort laser pulses. *Journal of Experimental and Theoretical Physics*, 39(2), 1974.

[39] P. B. Allen. Theory of thermal relaxation of electrons in metals. *Phys. Rev. Lett.*, 59:1460, 1987.

[40] D.I. Khomskii T.S. Al'tshuler, G.G. Khaliullin. Investigation of the energy gap in SmB_6 by the ESR method. *Journal of Experimental and Theoretical Physics*, 63(6):1234, 1986.

[41] Marta Zonno. A glance on hot quasiparticles dynamics at the surface of bulk rashba materials. Master's thesis, Università degli studi di Trieste, 2013.

[42] Newport. Application note 29.

[43] Xiao-Liang Qi and Shou-Cheng Zhang. The quantum spin hall effect and topological insulators. *Physics Today*, 63(1):33–38, 2010.

[44] R. B. Laughlin. Quantized hall conductivity in two dimensions. *Phys. Rev. B*, 23:5632–5633, May 1981.

[45] M. V. Berry. Quantal phase factors accompanying adiabatic changes. *Proceedings of the Royal Society of London A: Mathematical, Physical and Engineering Sciences*, 392(1802):45–57, 1984.

[46] D. J. Thouless, M. Kohmoto, M. P. Nightingale, and M. den Nijs. Quantized hall conductance in a two-dimensional periodic potential. *Phys. Rev. Lett.*, 49:405–408, Aug 1982.

[47] J. E. Avron, R. Seiler, and B. Simon. Homotopy and quantization in condensed matter physics. *Phys. Rev. Lett.*, 51:51–53, Jul 1983.

[48] Shuichi Murakami, Naoto Nagaosa, and Shou-Cheng Zhang. Dissipationless quantum spin current at room temperature. *Science*, 301(5638):1348–1351, 2003.

[49] C. L. Kane and E. J. Mele. Z_2 topological order and the quantum spin hall effect. *Phys. Rev. Lett.*, 95:146802, Sep 2005.

[50] C. L. Kane and E. J. Mele. Quantum spin hall effect in graphene. *Phys. Rev. Lett.*, 95:226801, Nov 2005.

[51] Markus König, Steffen Wiedmann, Christoph Brüne, Andreas Roth, Hartmut Buhmann, Laurens W. Molenkamp, Xiao-Liang Qi, and Shou-Cheng Zhang. Quantum spin hall insulator state in hgte quantum wells. *Science*, 318(5851):766–770, 2007.

[52] Liang Fu, C. L. Kane, and E. J. Mele. Topological insulators in three dimensions. *Phys. Rev. Lett.*, 98:106803, Mar 2007.

[53] Haijun Zhang, Chao-Xing Liu, Xiao-Liang Qi, Xi Dai, Zhong Fang, and Shou-Cheng Zhang. Topological insulators in Bi_2Se_3, Bi_2Te_3 and Sb_2Te_3 with a single Dirac cone on the surface. *Nat Phys*, 5(6):438–442, 06 2009.

[54] Rashba E. I. Bychkov Yu. A. Properties of a 2d electron gas with lifted spectral degeneracy. *Journal of Experimental and Theoretical Physics*, 39:278, 1984.

[55] Jeffrey C. Y. Teo, Liang Fu, and C. L. Kane. Surface states and topological invariants in three-dimensional topological insulators: Application to $Bi_{1-x}Sb_x$. *Phys. Rev. B*, 78:045426, Jul 2008.

[56] Wei Zhang, Rui Yu, Hai-Jun Zhang, Xi Dai, and Zhong Fang. First-principles studies of the three-dimensional strong topological insulators Bi_2Te_3 , Bi_2Se_3 and Sb_2Te_3. *New Journal of Physics*, 12(6):065013, 2010.

[57] Binghai Yan, Lukas Müchler, and Claudia Felser. Prediction of weak topological insulators in layered semiconductors. *Phys. Rev. Lett.*, 109:116406, Sep 2012.

[58] Philip Hofmann. *Synchrotron-Radiation Studies of Topological Insulators*, pages 211–238. Springer International Publishing, Cham, 2013.

[59] M. Z. Hasan and C. L. Kane. Colloquium: Topological insulators. *Rev. Mod. Phys.*, 82:3046, 2010.

[60] D. Hsieh, Y. Xia, L. Wray, D. Qian, A. Pal, J. H. Dil, J. Osterwalder, F. Meier, G. Bihlmayer, C. L. Kane, Y. S. Hor, R. J. Cava, and M. Z. Hasan. Observation of unconventional quantum spin textures in topological insulators. *Science*, 323(5916):919–922, 2009.

[61] Marco Bianchi, Dandan Guan, Anna Stróżecka, Celia H. Voetmann, Shining Bao, Jose Ignacio Pascual, Asier Eiguren, and Philip Hofmann. Surface states on a topologically nontrivial semimetal: The case of sb(110). *Phys. Rev. B*, 85:155431, Apr 2012.

[62] Y. L. Chen, J. G. Analytis, J.-H. Chu, Z. K. Liu, S.-K. Mo, X. L. Qi, H. J. Zhang, D. H. Lu, X. Dai, Z. Fang, S. C. Zhang, I. R. Fisher, Z. Hussain, and Z.-X. Shen. Experimental Realization of a Three-Dimensional Topological Insulator, Bi_2Te_3. *Science*, 325(5937):178–181, 2009.

[63] Y. Xia, D. Qian, D. Hsieh, L. Wray, A. Pal, H. Lin, A. Bansil, D. Grauer, Y. S. Hor, R. J. Cava, and M. Z. Hasan. Observation of a large-gap topological-insulator class with a single dirac cone on the surface. *Nat Phys*, 5(6):398–402, 06 2009.

[64] R. Bistritzer and A. H. MacDonald. Electronic cooling in graphene. *Phys. Rev. Lett.*, 102:206410, May 2009.

[65] C. Cacho, A. Crepaldi, M. Battiato, J. Braun, F. Cilento, M. Zacchigna, M. C. Richter, O. Heckmann, E. Springate, Y. Liu, S. S. Dhesi, H. Berger, Ph. Bugnon, K. Held, M. Grioni, H. Ebert, K. Hricovini, J. Minár, and F. Parmigiani. Momentum-resolved spin dynamics of bulk and surface excited states in the topological insulator bi_2se_3. *Phys. Rev. Lett.*, 114:097401, Mar 2015.

[66] Alberto Crepaldi. *Strong spin-orbit coupling in low dimensional systems investigated by static and time-resolved ARPES*. PhD thesis, EPFL Lousanne, 2012.

[67] E. Frantzeskakis, N. de Jong, B. Zwartsenberg, T. V. Bay, Y. K. Huang, S. V. Ramankutty, A. Tytarenko, D. Wu, Y. Pan, S. Hollanders, M. Radovic, N. C. Plumb, N. Xu, M. Shi, C. Lupulescu, T. Arion, R. Ovsyannikov, A. Varykhalov, W. Eberhardt, A. de Visser, E. van Heumen, and M. S. Golden. Dirac states with knobs on: Interplay of external parameters and the surface electronic properties of three-dimensional topological insulators. *Phys. Rev. B*, 91:205134, May 2015.

[68] Elettra-sincrotrone, s.c.p.a. di interesse nazionale, strada statale 14 - km 163,5 in area science park 34149 basovizza, trieste (italy).

[69] J. C. Johannsen, G. Autès, A. Crepaldi, S. Moser, B. Casarin, F. Cilento, M. Zacchigna, H. Berger, A. Magrez, Ph. Bugnon, J. Avila, M. C. Asensio, F. Parmigiani, O. V. Yazyev, and M. Grioni. Engineering the topological surface states in the $(\mathrm{Sb}_2)_m - \mathrm{sb}_2\mathrm{te}_3\,(m = 0\tilde{}3)$ superlattice series. *Phys. Rev. B*, 91:201101, 2015.

[70] Matteo Michiardi, Irene Aguilera, Marco Bianchi, Vagner Eustáquio de Carvalho, Luiz Orlando Ladeira, Nayara Gomes Teixeira, Edmar Avellar Soares, Christoph Friedrich, Stefan Blügel, and Philip Hofmann. Bulk band structure of bi_2te_3. *Phys. Rev. B*, 90:075105, Aug 2014.

[71] A. Marcinkova, J. K. Wang, C. Slavonic, Andriy H. Nevidomskyy, K. F. Kelly, Y. Filinchuk, and E. Morosan. Topological metal behavior in $gebi_2te_4$ single crystals. *Phys. Rev. B*, 88:165128, Oct 2013.

[72] M. Lisowski, P.A. Loukakos, U. Bovensiepen, and M. Wolf. Femtosecond dynamics

and transport of optically excited electrons in epitaxial cu films on si(111)-7×7. *Applied Physics A*, 79(4):739–741, 2004.

[73] U. Bovensiepen. Coherent and incoherent excitations of the gd(0001) surface on ultrafast timescales. *J. Phys.: Condens. Matter*, 19:083201, 2007.

[74] Justin C. W. Song, Michael Y. Reizer, and Leonid S. Levitov. Disorder-assisted electron-phonon scattering and cooling pathways in graphene. *Phys. Rev. Lett.*, 109:106602, Sep 2012.

[75] Jens Christian Johannsen, Søren Ulstrup, Federico Cilento, Alberto Crepaldi, Michele Zacchigna, Cephise Cacho, I. C. Edmond Turcu, Emma Springate, Felix Fromm, Christian Raidel, Thomas Seyller, Fulvio Parmigiani, Marco Grioni, and Philip Hofmann. Direct view of hot carrier dynamics in graphene. *Phys. Rev. Lett.*, 111:027403, Jul 2013.

[76] Zhi Ren, A. A. Taskin, Satoshi Sasaki, Kouji Segawa, and Yoichi Ando. Optimizing $Bi_{2-x}Sb_xTe_{3-y}Se_y$ solid solutions to approach the intrinsic topological insulator regime. *Phys. Rev. B*, 84:165311, Oct 2011.

[77] J. Reimann, J. Güdde, K. Kuroda, E. V. Chulkov, and U. Höfer. Spectroscopy and dynamics of unoccupied electronic states of the topological insulators Sb_2Te_3 and Sb_2Te_2S. *Phys. Rev. B*, 90:081106, Aug 2014.

[78] Z.-H. Zhu, A. Nicolaou, G. Levy, N. P. Butch, P. Syers, X. F. Wang, J. Paglione, G. A. Sawatzky, I. S. Elfimov, and A. Damascelli. Polarity-Driven Surface Metallicity in SmB_6. *Phys. Rev. Lett.*, 111:216402, Nov 2013.

[79] Pedram Roushan, Jungpil Seo, Colin V. Parker, Y. S. Hor, D. Hsieh, Dong Qian, Anthony Richardella, M. Z. Hasan, R. J. Cava, and Ali Yazdani. Topological surface states protected from backscattering by chiral spin texture. *Nature*, 460(7259):1106–1109, 08 2009.

[80] A. Menth, E. Buehler, and T. H. Geballe. Magnetic and Semiconducting Properties of SmB_6. *Phys. Rev. Lett.*, 22:295–297, Feb 1969.

[81] M. Neupane, N. Alidoust, S.-Y. Xu, T. Kondo, Y. Ishida, D.J. Kim, C. Liu, I. Belopolski, Y.J. Jo, T.-R. Chang, H.-T. Jeng, T. Durakiewicz, L. Balicas, H. Lin, A. Bansil, S. Shin,

Z. Fisk, and M.Z. Hasan. Surface electronic structure of the topological kondo-insulator candidate correlated electron system smb6. *Nat. Commun.*, 4(2991), 2013.

[82] P. Hlawenka, K. Siemensmeyer, E. Weschke, A. Varykhalov, J. Sánchez-Barriga, N. Y. Shitsevalova, A. V. Dukhnenko, V. B. Filipov, S. Gábani, K. Flachbart, O. Rader, and E. D. L. Rienks. Samarium hexaboride: A trivial surface conductor. *arXiv:1502.01542v1*, 2015.

[83] J. W. Allen, B. Batlogg, and P. Wachter. Large low-temperature Hall effect and resistivity in mixed-valent SmB_6. *Phys. Rev. B*, 20:4807–4813, Dec 1979.

[84] G Aeppli and Z Fisk. Kondo insulators comment. condes. *Matter Phys*, 16(155):1192, 1992.

[85] Hongming Weng, Jianzhou Zhao, Zhijun Wang, Zhong Fang, and Xi Dai. Topological crystalline kondo insulator in mixed valence ytterbium borides. *Phys. Rev. Lett.*, 112:016403, Jan 2014.

[86] M. B. Maple and D. Wohlleben. Nonmagnetic $4f$ shell in the high-pressure phase of sms. *Phys. Rev. Lett.*, 27:511–515, Aug 1971.

[87] Maxim Dzero, Jing Xia, Victor Galitski, and Piers Coleman. Topological kondo insulators. *Annual Review of Condensed Matter Physics*, 7(1):249–280, 2016.

[88] Jun Kondo. Resistance minimum in dilute magnetic alloys. *Progress of Theoretical Physics*, 32(1):37–49, 1964.

[89] Piers Coleman. Heavy fermions and the kondo lattice: a 21st century perspective. arXiv:1509.05769, 2015.

[90] S. Doniach. The kondo lattice and weak antiferromagnetism. *Physica B+C*, 91:231 – 234, 1977.

[91] Richard M. Martin and J. W. Allen. Theory of mixed valence: Metals or small gap insulators (invited). *Journal of Applied Physics*, 50(B11):7561–7566, 1979.

[92] Akira Yanase and Hisatomo Harima. Band Calculations on YbB_{12}, SmB_6 and CeNiSn. *Progress of Theoretical Physics Supplement*, 108:19–25, 1992.

[93] V. N. Antonov, B. N. Harmon, and A. N. Yaresko. Electronic structure of mixed-valence semiconductors in the LSDA + U approximation. II. SmB_6 and YbB_{12}. *Phys. Rev. B*, 66:165209, Oct 2002.

[94] Tetsuya Takimoto. SmB_6: A Promising Candidate for a Topological Insulator. *Journal of the Physical Society of Japan*, 80(12):123710, 2011.

[95] D. J. Kim, S. Thomas, T. Grant, J. Botimer, Z. Fisk, and Jing Xia. Surface hall effect and nonlocal transport in smb6: Evidence for surface conduction. *Scientific Reports*, 3:3150 EP –, 11 2013.

[96] J. C. Cooley, M. C. Aronson, Z. Fisk, and P. C. Canfield. Smb_6: Kondo insulator or exotic metal? *Phys. Rev. Lett.*, 74:1629–1632, Feb 1995.

[97] Xiaohang Zhang, N. P. Butch, P. Syers, S. Ziemak, Richard L. Greene, and Johnpierre Paglione. Hybridization, Inter-Ion Correlation, and Surface States in the Kondo Insulator SmB_6. *Phys. Rev. X*, 3:011011, Feb 2013.

[98] Steven Wolgast, Çağlı yan Kurdak, Kai Sun, J. W. Allen, Dae-Jeong Kim, and Zachary Fisk. Low-temperature surface conduction in the Kondo insulator SmB_6. *Phys. Rev. B*, 88:180405, Nov 2013.

[99] N. Xu, P. K. Biswas, J. H. Dil, R. S. Dhaka, G. Landolt, S. Muff, C. E. Matt, X. Shi, N. C. Plumb, M. Radović, E. Pomjakushina, K. Conder, A. Amato, S. V. Borisenko, R. Yu, H. M. Weng, Z. Fang, X. Dai, J. Mesot, H. Ding, and M. Shi. Direct observation of the spin texture in SmB_6 as evidence of the topological Kondo insulator. *Nature Communications*, 5:4566 EP –, 07 2014.

[100] E. Frantzeskakis, N. de Jong, B. Zwartsenberg, Y. K. Huang, Y. Pan, X. Zhang, J. X. Zhang, F. X. Zhang, L. H. Bao, O. Tegus, A. Varykhalov, A. de Visser, and M. S. Golden. Kondo hybridization and the origin of metallic states at the (001) surface of smb_6. *Phys. Rev. X*, 3:041024, Dec 2013.

[101] Y. Ishida, T. Otsu, T. Shimada, M. Okawa, Y. Kobayashi, F. Iga, T. Takabatake, and S. Shin. Emergent photovoltage on smb6 surface upon bulk-gap evolution revealed by pump-and-probe photoemission spectroscopy. *Scientific Reports*, 5:8160, 2015.

[102] E. E. Vainshtein, S. M. Blokhin, and Y. B. Paderno. *Sov. Phys. Solid State*, 6:2318, 1965.

[103] D. Malterre, M. Grioni, and Y. Baer. Recent developments in high-energy spectroscopies of kondo systems. *Advances in Physics*, 45(4):299, 1996.

[104] G. Li, Z. Xiang, F. Yu, T. Asaba, B. Lawson, P. Cai, C. Tinsman, A. Berkley, S. Wolgast, Y. S. Eo, Dae-Jeong Kim, C. Kurdak, J. W. Allen, K. Sun, X. H. Chen, Y. Y. Wang, Z. Fisk, and Lu Li. Two-dimensional fermi surfaces in kondo insulator smb6. *Science*, 346(6214):1208–1212, 2014.

[105] N. Xu, X. Shi, P. K. Biswas, C. E. Matt, R. S. Dhaka, Y. Huang, N. C. Plumb, M. Radović, J. H. Dil, E. Pomjakushina, K. Conder, A. Amato, Z. Salman, D. McK. Paul, J. Mesot, H. Ding, and M. Shi. Surface and bulk electronic structure of the strongly correlated system SmB_6 and implications for a topological Kondo insulator. *Phys. Rev. B*, 88:121102, 2013.

[106] J. D. Denlinger, J. W. Allen, J.-S. Kang, K. Sun, J.-W. Kim, J.H. Shim, B. I. Min, D.-J. Kim, and Z. Fisk. Temperature dependence of linked gap and surface state evolution in the mixed valent topological insulator smb6. *arXiv:1312.6637v2*, 2013.

[107] S.V. Ramankutty, N. de Jong, Y.K. Huang, B. Zwartsenberg, F. Massee, T.V. Bay, M.S. Golden, and E. Frantzeskakis. Comparative study of rare earth hexaborides using high resolution angle-resolved photoemission. *Journal of Electron Spectroscopy and Related Phenomena*, pages –, 2015.

[108] P. A. Alekseev, B. Dorner A. S. Ivanov, H. Schober, A. S. Mishchenko K. A. Kikoin, V. N. Lazukov, E. S. Konovalova, Y. B. Paderno, A. Y. Rumyantsev, and I. P. Sadikov. Lattice dynamics of intermediate valence semiconductor smb6. *Europhys. Lett.*, 10:457–463, 1989.

[109] Michael E. Valentine, Seyed Koohpayeh, W. Adam Phelan, Tyrel M. McQueen, Priscila F. S. Rosa, Zachary Fisk, and Natalia Drichko. Breakdown of the kondo insulating state in $\mathrm{smb_6}$ by introducing sm vacancies. *Phys. Rev. B*, 94:075102, Aug 2016.

[110] A. Tytarenko, E. van Heumen, and et al. *In preparation*, 2016.

[111] W. A. Phelan, S. M. Koohpayeh, P. Cottingham, J. W. Freeland, J. C. Leiner, C. L. Broholm, and T. M. McQueen. Correlation between bulk thermodynamic measurements and the low-temperature-resistance plateau in smb_6. *Phys. Rev. X*, 4:031012, Jul 2014.

[112] Feng Lu, JianZhou Zhao, Hongming Weng, Zhong Fang, and Xi Dai. Correlated topological insulators with mixed valence. *Phys. Rev. Lett.*, 110:096401, Feb 2013.

[113] G. Travaglini and P. Wachter. Intermediate-valent smb_6 and the hybridization model: An optical study. *Phys. Rev. B*, 29:893–898, 1984.

[114] Li Hong Bao, O. Tegus, Jiu Xing Zhang, Xin Zhang, and Ying Kai Huang. Large emission current density of $\mathrm{La}_x\mathrm{Ce}_{1-x}\mathrm{B}_6$ high quality single crystals grown by floating zone technique. *Journal of Alloys and Compounds*, 558:39 – 43, 2013.

[115] M. Neupane, S.-Y. Xu, L. A. Wray, A. Petersen, R. Shankar, N. Alidoust, Chang Liu, A. Fedorov, H. Ji, J. M. Allred, Y. S. Hor, T.-R. Chang, H.-T. Jeng, H. Lin, A. Bansil, R. J. Cava, and M. Z. Hasan. Topological surface states and dirac point tuning in ternary topological insulators. *Phys. Rev. B*, 85:235406, Jun 2012.

[116] T. Kasuya, K. Takegahara, T. Fujita, T. Tanaka, and E. Bannai. *J. Phys. (Paris)*, 40(5):308, 1979.

[117] S. von Molnar, T. Theis, A. Benoit, A. Briggs, J. Floquet, J. Ravex, z. Fisk, P. Watcher, and H. Boppart. *Valence Instabilities, North Holland, Amsterdam*, page 389, 1982.

[118] YuQi Xia. PhD thesis, Princeton University, 2010.

[119] H. Wang, K. A. LeBlanc, B. Gao, and Y. Yao. Thermodynamic ground state of MgB_6 predicted from first principles structure search methods. *The Journal of Chemical Physics*, 140:044710, 2014.

[120] J. Teyssier, A. Kuzmenko, D. van der Marel, R. Lortz, A. Junod, V. Filippov, and N. Shitsevalova. Electronic and optical properties of zrb12 and yb6. discussion on electron-phonon. *Phys. Stat. Sol. (c)*, 3(9):3114, 2006.

[121] Z.-H. Zhu, C. N. Veenstra, S. Zhdanovich, M. P. Schneider, T. Okuda, K. Miyamoto, S.-Y. Zhu, H. Namatame, M. Taniguchi, M. W. Haverkort, I. S. Elfimov, and A. Damascelli.

Photoelectron Spin-Polarization Control in the Topological Insulator Bi_2Se_3. *Phys. Rev. Lett.*, 112:076802, Feb 2014.

[122] M. Ärrälä, J. Nieminen, J. Braun, H. Ebert, and M. Lindroos. Photon energy dependence of circular dichroism of the au(111) surface state. *Phys. Rev. B*, 88:195413, Nov 2013.

[123] L. Petaccia, P. Vilmercati, S. Gorovikov, M. Barnaba, A. Bianco, D. Cocco, C. Masciovecchio, and A. Goldoni. Bad elph: A 4 m normal-incidence monochromator beamline at elettra. *Nuclear Instruments and Methods in Physics Research Section A: Accelerators, Spectrometers, Detectors and Associated Equipment*, 606(3):780 – 784, 2009.

[124] K. Okamoto, K. Kuroda, H. Miyahara, K. Miyamoto, T. Okuda, Z. S. Aliev, M. B. Babanly, I. R. Amiraslanov, K. Shimada, H. Namatame, M. Taniguchi, D. A. Samorokov, T. V. Menshchikova, E. V. Chulkov, and A. Kimura. Observation of a highly spin-polarized topological surface state in $gebi_2te_4$. *Phys. Rev. B*, 86:195304, Nov 2012.

[125] Masashi Arita, Hitoshi Sato, Kenya Shimada, Hirofumi Namatame, Masaki Taniguchi, Minoru Sasaki, Mamoru Kitaura, Akimasa Ohnishi, and Heon-Jung Kim. *Angle resolved photoemission study of GeBi¡sub¿2¡/sub¿Te¡sub¿4¡/sub¿*.

[126] A. Sterzi, A. Crepaldi, F. Cilento, G. Manzoni, E. Frantzeskakis, M. Zacchigna, E. van Heumen, Y. K. Huang, M. S. Golden, and F. Parmigiani. $\mathrm{SmB_6}$ electron-phonon coupling constant from time- and angle-resolved photoelectron spectroscopy. *Phys. Rev. B*, 94:081111, Aug 2016.

[127] Shuigang Xu, Yu Han, Xiaolong Chen, Zefei Wu, Lin Wang, Tianyi Han, Weiguang Ye, Huanhuan Lu, Gen Long, Yingying Wu, Jiangxiazi Lin, Yuan Cai, K. M. Ho, Yuheng He, and Ning Wang. van der Waals Epitaxial Growth of Atomically Thin Bi_2Se_3 and Thickness-Dependent Topological Phase Transition. *Nano Letters*, 15(4):2645–2651, 2015.

[128] M. Zahid Hasan, Su-Yang Xu, and Madhab Neupane. Topological insulators, topological crystalline insulators, topological semimetals and topological kondo insulators. 2014.

[129] Yue Cao, J. A. Waugh, X-W. Zhang, J-W. Luo, Q. Wang, T. J. Reber, S. K. Mo, Z. Xu, A. Yang, J. Schneeloch, G. D. Gu, M. Brahlek, N. Bansal, S. Oh, A. Zunger, and D. S.

Dessau. Mapping the orbital wavefunction of the surface states in three-dimensional topological insulators. *Nat Phys*, 9(8):499–504, 08 2013.

[130] Chris Jozwiak, Jonathan A. Sobota, Kenneth Gotlieb, Alexander F. Kemper, Costel R. Rotundu, Robert J. Birgeneau, Zahid Hussain, Dung-Hai Lee, Zhi-Xun Shen, and Alessandra Lanzara. Spin-polarized surface resonances accompanying topological surface state formation. *Nature Communications*, 7:13143 EP –, 10 2016.

[131] Christoph Seibel, Hendrik Bentmann, Jürgen Braun, Jan Minár, Henriette Maaß, Kazuyuki Sakamoto, Masashi Arita, Kenya Shimada, Hubert Ebert, and Friedrich Reinert. Connection of a Topological Surface State with the Bulk Continuum in $\mathrm{Sb_2Te_3}(0001)$. *Phys. Rev. Lett.*, 114:066802, Feb 2015.

[132] Leon Balents. Viewpoint: Weyl electron kiss. *Physics*, 4(36), 2011.

[133] N. Xu, Z. J. Wang, A. P. Weber, A. Magrez, P. Bugnon, H. Berger, C. E. Matt, J. Z. Ma, B. B. Fu, B. Q. Lv, N. C. Plumb, M. Radovic, E. Pomjakushina, K. Conder, T. Qian, J. H. Dil, J. Mesot, H. Ding, and M. Shi. Discovery of Weyl semimetal state violating Lorentz invariance in $\mathrm{MoTe_2}$. *arXiv:1604.02116*, 2016.

[134] M. N. Ali, J. Xiong, S. Flynn, J. Tao, Q. D. Gibson, L. M. Schoop, T. Liang, N. Haldolaarachchige, M. Hirschberger, N. P. Ong, and R. J. Cava. *Nature*, 514:205, 2014.

[135] X.-C. Pan, X. Chen, H. Liu, Y. Feng, Z. Wei, Y. Zhou, Z. Chi, L. Pi, F.Yen, F. Song, X. Wan, Z. Yang, B. Wang, G. Wang, and Y. Zhang. Pressure-driven dome-shaped superconductivity and electronic structural evolution in tungsten ditelluride. *Nat. Communication*, 6:7805, 2015.

[136] Pavel Y. Qi, N. Mazhar, N. Ali, C. R. Rajamathi, O. Barkalov, M. Hanfland, S.-C. Wu, C. Shekhar, Y. Sun, V. Su, M. Schmidt, E. Pippel, P. Werner, R. Hillebrand, T. Forster, E. Kampertt, W. Schnelle, S. Parkin, R. J. Cava, C. Felser, B. Yan, and S. A. Medvedev. Superconductivity in weyl semimetal candidate mote2. *Nature Comm.*, 7:11038, 2016.

[137] Pavan Hosur. Friedel oscillations due to fermi arcs in weyl semimetals. *Phys. Rev. B*, 86:195102, Nov 2012.

[138] Teemu Ojanen. Helical fermi arcs and surface states in time-reversal invariant weyl semimetals. *Phys. Rev. B*, 87:245112, Jun 2013.

[139] Ilya Belopolski, Su-Yang Xu, Daniel Sanchez, Guoqing Chang, Cheng Guo, Madhab Neupane, Hao Zheng, Chi-Cheng Lee, Shin-Ming Huang, Guang Bian, Nasser Alidoust, Tay-Rong Chang, BaoKai Wang, Xiao Zhang, Arun Bansil, Horng-Tay Jeng, Hsin Lin, Shuang Jia, and M. Zahid Hasan. Criteria for directly detecting topological fermi arcs in weyl semimetals. Phys. Rev. Lett. 116, 066802 (2016), 2016.

[140] L. Huang, T. M. McCormick nd M. Ochi, Z. Zhao, M. to Suzuki, R. Arita, Y. Wu, D. Mou, H. Cao, J. Yan, N. Trivedi, and A. Kaminski. Spectroscopic evidence for type ii weyl semimetal state in mote2. *Accepted on Nat. Material, arXiv:1603.06482v1*, 2016.

[141] K. Deng, G. Wan, P. Deng, K. Zhang, S. Ding, E. Wang, M. Yan, H. Huang, H. Zhang, Z. Xu, J. Denlinger, A. Fedorov, H. Yang, W. Duan, H. Yao, Y. Wu, S. Fan, H. Zhang, X. Chen, and S. Zhou. Experimental observation of topological fermi arcs in type-ii weyl semimetal mote2. *Accepted on Nat. Phys, arXiv:1603.08508v1*, 2016.

[142] A. Liang, J. Huang, S. Nie, Y. Ding, Q. Gao, C. Hu, S. He, Y. Zhang, C. Wang, B. Shen, J. Liu, P Ai, L. Yu, X. Sun, W. Zhao, S. Lv, D. Liu, C. Li, Y. Zhang, Y. Hu, Y. Xu, L. Zhao, G. Liu, Z. Mao, X. Jia, F. Zhang, S. Zhang, F. Yang, Z Wang, Q. Peng, H. Weng, X. Dai, Z. Fang, Z. Xu, C. Chen, and X. J. Zhou. Electronic evidence for type ii weyl semimetal state in mote2. *arXiv:1604.01706v1*, 2016.

[143] N. Xu, Z. J. Wang, A. P. Weber, A. Magrez, P. Bugnon, H. Berger, C. E. Matt, J. Z. Ma, B. B. Fu, B. Q. Lv, N. C. Plumb, M. Radovic, E. Pomjakushina, K. Conder, T. Qian, J. H. Dil, J. Mesot, H. Ding, and M. Shi. Discovery of weyl semimetal state violating lorentz invariance in mote2. *arXiv:1604.02116v1*, 2016.

[144] J. Jiang, Z. K. Liu, Y. Sun, H. F. Yang, R. Rajamathi, Y. P. Qi, L. X. Yang, C. Chen, H. Peng, C.-C. Hwang, S. Z. Sun, S.-K. Mo, I. Vobornik, J. Fujii, S. S. P. Parkin, C. Felser, B. H. Yan, and Y. L. Chen. Observation of the type-ii weyl semimetal phase in mote2. *arXiv:1604.00139v1*, 2016.

[145] Measuring chern numbers above the fermi level in the type ii weyl semimetal moxw1?xte2. *arXiv:1604.07079v1*, 2016.

[146] Z. Wang, D. Gresch, A. A. Soluyanov, W. Xie, X. Dai, M. Troyer, R. J. Cava, and B. A. Bernevig. $MoTe_2$: A type-ii weyl topological metal. *Phys. Rev. Lett.*, 117:056805, 2016.

[147] W. L. McMillan. Theory of discommensurations and the commensurate-incommensurate charge-density-wave phase transition. *Phys. Rev. B*, 14:1496, 1976.

[148] E. Morosan, H. W. Zandbergen, B. S. Dennis, J. W. G. Bos, Y. Onose, T. Klimczuk, A. P. Ramirez, N. P. Ong, and R. J. Cava. Superconductivity in cuxtise2. *Nat. Physics*, 2:554, 2006.

[149] A. A. Soluyanov, D. Gresch, Z. Wang, Q. Wu, M. Troyer, X. Dai, and B. A. Bernevig. *Nature*, 527:495, 2015.

[150] S.-M. Huang, S.-Y. Xu, I. Belopolski, C.-C. Lee, G. Chang, B.K. Wang, N. Alidoust, G. Bian, M. Neupane, C. Zhang, S. Jia, A. Bansil, H. Lin, and M. Z. Hasan. A weyl fermion semimetal with surface fermi arcs in the transition metal monopnictide taas class. *Nat. Communication*, 6:7373, 2015.

[151] Hongming Weng, Chen Fang, Zhong Fang, B. Andrei Bernevig, and Xi Dai. Weyl semimetal phase in noncentrosymmetric transition-metal monophosphides. *Phys. Rev. X*, 5:011029, 2015.

[152] Xiaochun Huang, Lingxiao Zhao, Yujia Long, Peipei Wang, Dong Chen, Zhanhai Yang, Hui Liang, Mianqi Xue, Hongming Weng, Zhong Fang, Xi Dai, and Genfu Chen. Observation of the chiral-anomaly-induced negative magnetoresistance in 3d weyl semimetal taas. *Phys. Rev. X*, 5:031023, 2015.

[153] C.-L. Zhang, S.-Y. Xu, I. Belopolski, Z. Yuan, Z. Lin, B. Tong, G. Bian, N. Alidoust, C.-C. Lee, S.-M. Huang, T.-R. Chang, G.Chang, C.-H. Hsu, H.-T. Jeng, M. Neupane, D. S. Sanchez, H. Zheng, J. Wang, H. Lin, C. Zhang, H.-Z. Lu, S.-Q. Shen, T.s Neupert, M. Z. Hasan, and S. Jia. *Nat. Communication*, 7:10735, 2016.

[154] S.-Y. Xu, I. Belopolski, N. Alidoust, M. Neupane, G. Bian, C. Zhang, R. Sankar, G. Chang, Z. Yuan, C.-C. Lee, S.-M. Huang, H. Zheng, J. Ma, D. S. Sanchez, B. Wang,

A. Bansil, F. Chou, P. P. Shibayev, H. Lin, S. Jia, and M. Z. Hasan. Discovery of a weyl fermion semimetal and topological fermi arcs. *Science*, 349:613, 2015.

[155] L. X. Yang andZ. K. Liu, Y. Sun, H. Peng, H. F. Yang, T. Zhang, B. Zhou, Y. Zhang, Y. F. Guo, M. Rahn, D. Prabhakaran, Z. Hussain, S.-K. Mo, C. Felser, B. Yan, and Y. L. Chen. Weyl semimetal phase in the non-centrosymmetric compound taas. *Nat. Physics*, 11:728, 2015.

[156] B. Q. Lv, N. Xu, H. M. Weng, J. Z. Ma, P. Richard, X. C. Huang, L. X. Zhao, G. F. Chen, C. E. Matt, F. Bisti, V. N. Strocov, J. Mesot, Z. Fang, X. Dai, T. Qian, M. Shi, and H. Ding. Observation of weyl nodes in taas. *Nat. Physics*, 11:724, 2015.

[157] B. Q. Lv, H. M. Weng, B. B. Fu, X. P. Wang, H. Miao, J. Ma, P. Richard, X. C. Huang, L. X. Zhao, G. F. Chen, Z. Fang, X. Dai, T. Qian, and H. Ding. Experimental discovery of weyl semimetal taas. *Phys. Rev. X*, 5:031013, 2015.

[158] Observation of weyl nodes and fermi arcs in tantalum phosphide. *Nat. Communication*, 7:11006, 2016.

[159] Y. Sun, S.-C. Wu, M. N. Ali, C. Felser, and B. Yan. Prediction of weyl semimetal in orthorhombic mote2. *Phys. Rev. B*, 92:161107, 2015.

[160] T. R. Chang, S.-Y. Xu, G. Chang, C.-C. Lee, S.-M. Huang, B. K. Wang, G. Bian, H. Zheng, D. S. Sanchez, I. Belopolski andN. Alidoust, M. Neupane, A. Bansil, H.-T. Jeng, H. Lin, and M. Z. Hasan. Prediction of an arc-tunable weyl fermion metallic state in moxw1?xte2. *Nat. Communication*, 7:10639, 2016.

[161] G. Autès, D. Gresch, M. Troyer, A. A. Soluyanov, and O. V. Yazyev. Robust type-ii weyl semimetal phase in transition metal diphosphides xp2 (x =mo, w). *Phys. Rev. Lett.*, 117:066402, 2016.

[162] H P Hughes and R H Friend. Electrical resistivity anomaly in ?-mote2 (metallic behaviour). *J. Phys. C: Solid State Phys.*, 11:L103, 1978.

[163] C. Bigi, J. Fujii, I. Vobornik, P. K. Das, D. Benedetti, F. Salvador, G. Panaccione, and G. Rossi. Very efficient spin polarization analysis (vespa): New exchange scattering-

based setup for spin-resolved arpes at ape-nffa beamline at elettra. *arXiv:1610.06922*, 2016.

[164] P. Giannozzi, S. Baroni, N. Bonini, M. Calandra, R. Car, C. Cavazzoni, D. Ceresoli, G. L Chiarotti, M. Cococcioni, I. Dabo, A. Dal Corso, S. de Gironcoli, S. Fabris, G. Fratesi, R. Gebauer, U. Gerstmann, C. Gougoussis, A. Kokalj, M. Lazzeri, L. Martin-Samos, N. Marzari, F. Mauri, R. Mazzarello, S. Paolini, A. Pasquarello, L. Paulatto, C. Sbraccia, S. Scandolo, G. Sclauzero, A. P. Seitsonen, A. Smogunov, P. Umari, and R. M. Wentzcovitch. Quantum espresso: a modular and open-source software project for quantum simulations of materials. *J. Phys.: Condens. Matter*, 21:395502, 2009.

[165] A. Umerski. Closed-form solutions to surface green's functions. *Phys. Rev. B*, 55:5266–5275, Feb 1997.

[166] Arash A. Mostofi, Jonathan R. Yates, Giovanni Pizzi, Young-Su Lee, Ivo Souza, David Vanderbilt, and Nicola Marzari. An updated version of wannier90: A tool for obtaining maximally-localised wannier functions. *Computer Physics Communications*, 185(8):2309 – 2310, 2014.

[167] A. Dal Corso and A. Mosca Conte. *Phys. Rev. B*, 71:115106, 2005.

[168] B. E. Brown. *Acta Crystallographica*, 20(3800):268, 1966.

[169] A. Crepaldi, F. Cilento, M. Zacchigna, M. Zonno, J. C. Johannsen, C. Tournier-Colletta, L. Moreschini, I. Vobornik, F. Bondino, E. Magnano, H. Berger, A. Magrez, Ph. Bugnon, G. Autès, O. V. Yazyev, M. Grioni, and F. Parmigiani. Momentum and photon energy dependence of the circular dichroic photoemission in the bulk rashba semiconductors $\mathrm{BiTe}x$ ($x =$ I, br, cl). *Phys. Rev. B*, 89:125408, 2014.

[170] G. Manzoni, L. Gragnaniello, G. Autès, T. Kuhn, A. Sterzi, F. Cilento, M. Zacchigna, V. Enenkel, I. Vobornik, L. Barba, F. Bisti, Ph. Bugnon, A. Magrez, V. N.Strocov, H. Berger, O. V. Yazyev, M. Fonin, F. Parmigiani, and A. Crepaldi. Evidence for a strong topological insulator phase in zrte5. *Phys. Rev. Lett.*, 117(23), Nov 2016.

[171] *For additional experimental results and ab initio calculations of the surface Fermi arcs see supplementary information at XXXX*. 2016.

[172] Alexey A. Soluyanov and David Vanderbilt. Computing topological invariants without inversion symmetry. *Phys. Rev. B*, 83:235401, Jun 2011.

[173] D. Gresch, Gabriel Autès, O. V. Yazyev, M. Troyer, D. Vanderbilt, B. A. Bernevig, and A. A. Soluyanov. Z2pack: Numerical implementation of hybrid wannier centers for identifying topological materials. *arXiv:1610.08983*, 2016.